Fall 1978

A STUDY OF THE (NEUTRON; NEUTRON', GAMMA) REACTION IN IRON AND ANTIMONY

JAMES MILLER HARRISON

265

HARRISON, JAMES MILLER
A STUDY OF THE (NEUTRON; NEUTRON', GAMMA) REACTION IN IRON AND ANTIMONY.

UNIVERSITY OF NEW HAMPSHIRE, PH.D., 1978

A STUDY OF THE (N,N'GAMMA)

REACTION IN IRON AND ANTIMONY

BY

JAMES M. HARRISON
B.S., Allegheny College, 1973
M.S., University of New Hampshire, 1975

A DISSERTATION

Submitted to the University of New Hampshire
In Partial Fulfillment of
The Requirements for the Degree of

Doctor of Philosophy
in
Physics

September, 1978

This thesis has been examined and approved.

Edward L. Chupp

Thesis director, Edward L. Chupp, Prof. of Physics

John F. Dawson

John Dawson, Associate Professor of Physics

Barry Harrington

Barry Harrington, Assistant Professor of Physics

John A. Lockwood

John A. Lockwood, Professor of Physics

Robert E. Simpson

Robert E. Simpson, Associate Professor of Physics

8/11/78

Date

ACKNOWLEDGEMENTS

The author would like to express his thanks to Dr. Edward L. Chupp for his support and assistance in this research. Thanks also go to Thomas A. Patnode and Pamela J. Marden for their assistance in the experimental and data acquisition aspects of this project. For their assistance in the design and fabrication of experimental apparatus, Albert W. Knight and Arthur L. Anderson of the Physics Department shop deserve a note of thanks.

For the use of the computer programs MANDYF and SCAT, I would like to thank Dr. James Egan and Dr. Gus P. Couchell of the University of Lowell, Lowell, Massachusetts. For the use of the analysis program EVA I would like to express my appreciation to Dr. John M. Davidson and Dr. Peter Green of the Nuclear Research Centre, University of Alberta, Edmonton, Alberta, Canada.

For her support during this research and editorial assistance in the preparation of this paper I thank my wife, Janice D. Harrison.

Finally, I wish to acknowledge the support of NASA Grant NGL 30-002-018.

TABLE OF CONTENTS

LIST OF FIGURES

LIST OF TABLES

ABSTRACT

A STUDY OF THE (N,N'GAMMA) REACTION IN IRON AND ANTIMONY

by

JAMES MILLER HARRISON

An experiment has been performed to study gamma angular distributions and emission cross sections from the (n,n'gamma) reaction. A 5.5 MHz pulsed deuteron beam from a 400 keV Van de Graaff accelerator produced 3 MeV neutrons through the $d(d,n)^3He$ reaction. Utilizing a close source-scatterer geometry to achieve maximum neutron flux through natural iron and antimony samples, gamma radiation was detected with a 40 cm^3 Ge(Li) detector. Time-of-flight gating with a flight path length of 30 cm was employed to reduce background radiation.

Theoretical angular distributions were calculated using the statistical compound nucleus model. Corrections for distortion arising from the close geometry were applied to the theoretical distributions and compared to the raw experimental yields in an effort to assign spins and mixing ratios. Evidence for 9/2 spin assignments to the 0.947 MeV and 1.036 MeV levels of ^{121}Sb are reported as well as differential and total gamma emission cross sections for 3 MeV neutrons incident on iron and antimony.

I. INTRODUCTION

1-1 The Purpose of the Investigation

This paper is a discussion of an experiment which attempts to measure certain basic physical properties of nuclear structure as well as the probability of gamma emission from a nucleus following an inelastic neutron scattering reaction. There are two principal motivations behind the determination of these properties. The first is the desire to test a theory. A central problem of nuclear physics is to discover a potential which, when Schrödinger's equation is solved, will describe the physical properties, ie., energies, spins, parities, and decay modes, of levels in a given nucleus as well as reaction cross sections in interactions between particles and nuclei. Thus, in order to test the prediction of a given potential, we require measurements of these basic physical properties.

Of a more practical nature, the direct determination of such parameters as gamma emission cross sections as well as reliable theoretical predictions are useful in technological applications of physics. Neutron physics has proven quite useful in such applications. Some of these

include geophysical applications such as bore-hole logging, medical and health physics applications such as neutron radiography and neutron-gamma dosimetry, and energy production applications including materials studies for fission and fusion reactors. Also, this information is of increasing importance to other areas of experimental physics, such as gamma-ray astrophysics where neutron induced gamma background estimates are needed. All of these applications require reliable gamma emission cross sections for either identification of elements present in a substance or for estimating the gamma ray yield produced by neutrons incident on a substance. Therefore it is desirable to develop techniques to measure these properties.

1-2 Introduction to (n,n'gamma) Reaction Analysis

The inelastic neutron scattering, (n,n'gamma), reaction is well suited to the purposes described above. Specifically, the emission of gamma radiation following the inelastic scattering event is of interest. Angular distributions of gamma radiation provide information about the spin of nuclear levels and the mixing ratios of gamma transitions from the nuclear levels. Such information is extracted from angular distribution data as follows. A model is chosen for the reaction mechanism and theoretical calculations of the gamma angular distribution carried out with hypothetical values of level spin and decay mixing ratio for an excited state of a given nucleus. Here the

Wolfenstein-Hauser-Feshbach statistical compound nucleus theory is chosen to model the reaction mechanism (Wolfenstein, 1951; Hauser and Feshbach, 1952; Feshbach et al., 1954). Theoretical angular distributions are evaluated in the framework of this theory utilizing the computer codes SCAT and MANDYF (Smith, 1969; Sheldon and Donati, 1971) obtained from the (n,n'gamma) research group at the University of Lowell, Lowell, Massachusetts. Then the theoretical angular distributions are distorted to suit the geometry of the experiment. Finally, the distorted theoretical angular distributions are compared to experimental gamma yields at various angles and through this comparison likely values of spin and mixing ratio are chosen.

1-3 Introduction to the Experimental Technique

The (n,n'gamma) reaction has been used for more than 20 years to excite nuclei for level structure studies as well as cross section measurements (Van Loef and Lind, 1956; Hosoe and Suzuki, 1959; Day and Walt, 1960; Gilboy and Towle, 1964). Early reasearch was carried out with NaI(Tl) detectors and, while this was successful on strong, isolated gamma lines, such as the 0.847 MeV transition in ^{56}Fe, in many nuclei the gamma transitions were unresolved in NaI and meaningful angular distribution data could not be obtained. Thus in 1965, Ristinen et al., (1965) and Daniels et al., (1965) began research with Ge(Li) detectors. Even with the

relatively small crystals available at the time, ~ 3 cm^3 compared to 40 cm^3 used in this experiment, the advantage of the high resolution attainable with Ge(Li) detectors, ~ 20 times that with NaI, was apparent.

One of the problems encountered in (n,n'gamma) research has always been the difficulty of obtaining high-flux, monoenergetic neutron beams. The lower excited states of nuclei in the $A \geq 40$ region are generally in the area of ~ 1 MeV and usually an excitation energy of ~ 3 MeV includes many levels. Monoenergetic neutrons for laboratory use in the 1 - 3 MeV region are frequently produced using a charged particle reaction. The flux of neutrons produced in this way is limited by several factors. First the flux is radiated outward into 4π solid angle and second the flux is limited by the charged particle beam current available. Also target lifetime plays an important part when high current beams are available. In order to minimize this low flux limitation, the close source-scatterer geometry technique developed by the (n,n'gamma) research group at the Nuclear Research Center, Alberta, Canada was adopted (Elbakr et al., 1971; Davidson et al., 1976). In this approach, the sample is placed as close to the neutron source as target construction allows. Then a computer code, EVA, is used to correct for distortion due to this close geometry (Davidson, 1976). In addition, time-of-flight gating of the Ge(Li) energy spectrum is used to reduce background radiation produced by neutrons in the experimental area.

The Canadian group has met with considerable success in using this technique, particularly in the study of the (n,n'gamma) reaction in enriched isotopes where only small samples, ~ 5 g, are available (Elbakr et al., 1974; Newton et al., 1977; Davidson et al., 1977; Hooper et al., 1977).

The procedure followed in this research is as follows. First the technique, equipment, and analysis program are tested by attempting to duplicate the well known result that the 0.847 MeV level in ^{56}Fe is a +2 spin state. Then the same technique is applied to the odd A antimony isotopes, ^{121}Sb and ^{123}Sb, in an effort to learn something new about the properties of levels of these isotopes. Also gamma emission cross sections are reported for these elements.

There are several reasons for the choice of antimony as a sample material. First it has two stable isotopes present in about equal proportion. This allows measurements on both isotopes without necessitating the use of rare and expensive enriched isotopes. Secondly there are several levels of ^{121}Sb and ^{123}Sb which have not had definite spins assigned to them. Of particular interest are the 0.947 MeV and 1.036 MeV ^{121}Sb levels. The theoretical calculations of Vanden Berghe suggest the existence of several +9/2 levels in this energy region. Most previous experiments have not been able to definitely assign these +9/2 spins, leaving +7/2 and +11/2 as possible assignments (Booth et al., 1973; Barnes et al., 1966). Only Meyer in his recent paper on

beta decay of ^{121}Te has assigned definite +9/2 spin-parities to these levels (Meyer et al., 1975). Thus it is of value to attempt a measurement of these spins. Also little previous research on the (n,n'gamma) reaction in Sb has been done. Barnard et al., (1971) utilized the (n,n'gamma) reaction to study the excited levels of Sb, however, did not attempt angular distribution analysis and assigned spins on the basis of the decay schemes only. In addition to this, no reliable data on gamma emission cross sections for the Sb(n,n'gamma) reaction is available in the literature.

II. THEORETICAL BACKGROUND

2-1 Introduction

This chapter is concerned primarily with the calculation of differential cross sections and angular distributions, which are differential cross sections normalized to 1.0 at 90°, for gamma emission from the (n,n'gamma) reaction. This will be discussed for the more general case of an (a,a'gamma) reaction, where "a" is a particle of spin s, with specific references to the (n,n'gamma) reaction under the experimental conditions defined in Chapter III. A schematic of the reaction is presented in Figure 2-1. Basically a particle scatters off of a target nucleus leaving the residual nucleus in an excited state. The recoiling excited nucleus then decays after a short period of time characteristic of its particular state, typically $< 10^{-11}$ sec, and emits a gamma ray. The theoretical angular distribution of these gamma rays is dependent upon the reaction mechanism by which the residual nucleus was formed as well as the spins and energies of the particle and gamma transitions involved. As will become evident, we also must be able to calculate gamma

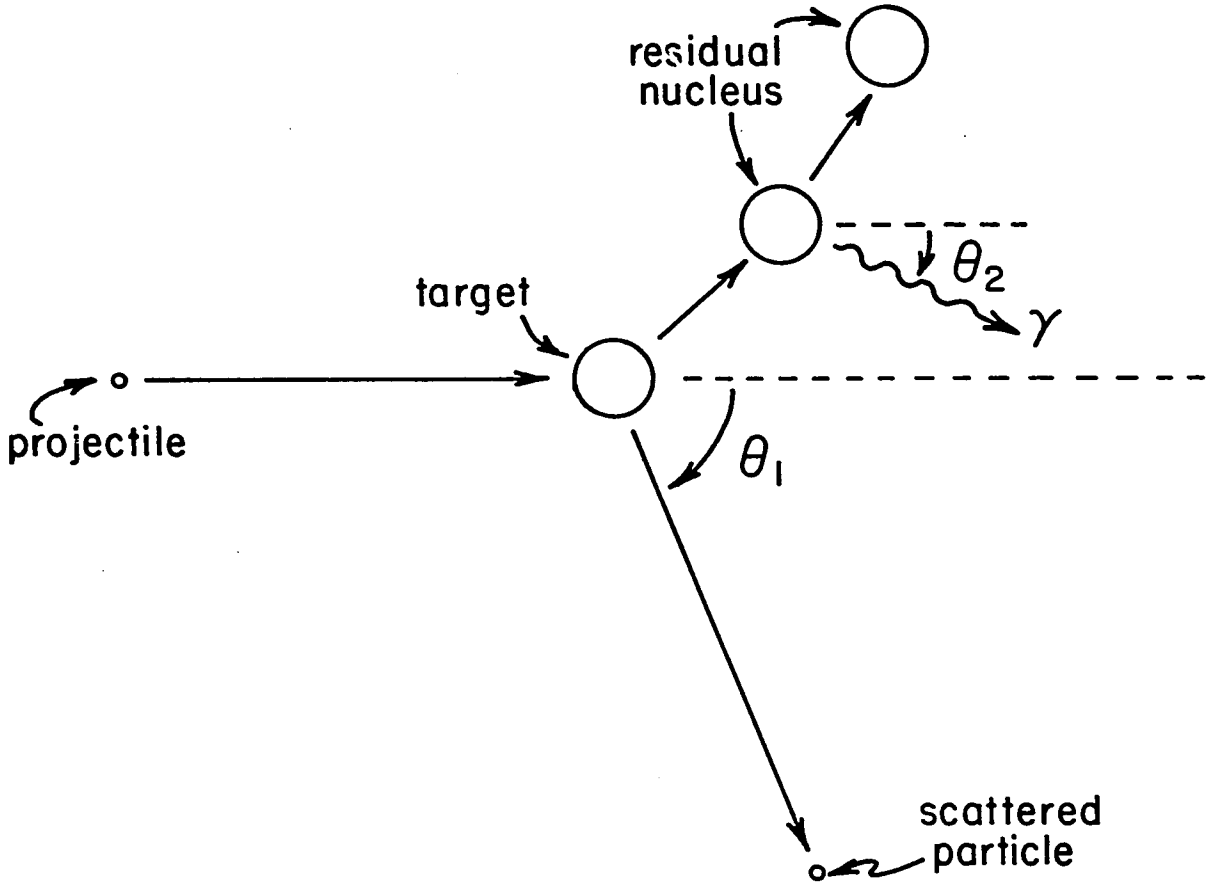
residual
nucleus
target
θ_2
γ
projectile
θ_1
scattered
particle

FIGURE 2-1

angular distributions from the second gamma in a cascade from the (n,n'gamma-gamma) reaction where the first gamma transition is unobserved. This is because cascades from higher excited levels in the residual nucleus can populate the level of interest and add a contribution to the observed gamma angular distribution.

At this point one may ask why the gamma distribution from the residual nucleus decay should be anything other than isotropic. Intuitively we expect a collection of randomly oriented excited nuclei to de-excite and emit gamma radiation isotropically. To show this, consider an excited nucleus in a $J_i = 1$, $m_i = -1, 0, +1$ state decaying by gamma emission to a $J_f = 0$, $m_f = 0$ state. This gamma decay is a dipole transition with L = 1 and M = -1, 0, +1. Thus three modes of decay are possible, one for each value of the magnetic quantum number M, representing an electromagnetic transition from each of the three magnetic substates of the $J_i = 1$ level. The general form for the angular distribution of gamma radiation from nuclear decay, $W_{LM}(\theta)$, can be calculated from electromagnetic theory (Blatt and Weisskopf p 594, 1952). Here we give the three partial distributions for L = 1 and M = -1, 0, +1

$$W_{1+1}(\theta) = 3/16\pi \quad (1 + \cos^2\theta)$$

$$W_{10}(\theta) = 3/8\pi \quad \sin^2\theta$$

$$W_{1-1}(\theta) = 3/16\pi \quad (1 + \cos^2\theta)$$

When summed over M we obtain the angular distribution

$$W(\theta) = 3/4\pi$$

which is an isotropic distribution as expected.

Now consider the angular distribution W(0) under the assumption that we can preferentially excite certain magnetic substates. If, for instance, the $J_i = 1$ state is excited by electromagnetic radiation incoming along a direction selected to be the $\hat{z}$ axis, the M = 0 substate will not be populated since sin $0^0 = 0$. Then, assuming that the alignment is maintained, the angular distribution of de-excitation radiation will be

$$W(\theta) = 3/8\pi \quad (1 + \cos^2\theta)$$

which is anisotropic. This non-uniform magnetic substate population is the basis for anisotropic distributions obtained in gamma-gamma correlation experiments as well as those obtained from inelastic scattering of neutrons and protons.

Regarding the case of inelastic neutron scattering specifically, in Section 2-2 we show that the incoming neutron direction defines an alignment axis by which the neutron cannot transfer any $\hat{z}$-component of angular momentum to the target nucleus. This produces an alignment of the excited nuclei with spin axes in the x-y plane. In terms of magnetic substates, this means that substates of different $|m|$ have different populations. It should be stressed that this is not an orientation or polarization of excited nuclei in which substates of $\pm$ m also have different populations.

Gamma angular distributions from de-excitation of non-uniformly populated magnetic substates are generally anisotropic. The distributions are dependent upon level spins, multipolarities and mixing ratios, but not parities (Sheldon and Van Patter p 185, 1966). Although parity determines the multipole character, ie., electric or magnetic, of the radiation, the distributions produced by these multipoles from an unpolarized source are identical (Blatt and Weisskopf p 596, 1952). The difference between these multipole radiations is in their respective polarizations which are not detected in this experiment. Thus we cannot learn anything about parity from these angular distributions.

An essential point to obtaining anisotropic angular distribution is the maintaining of the nuclear alignment brought about by preferentially exciting specific substates of the nucleus. If the nuclear alignment is lost before de-excitation, the angular distribution will become isotropic. This sets a requirement that the lifetime of the excited nuclear level be short enough so that interactions of the recoiling nucleus with extranuclear fields is minimized. In the case of short lived states, ~ 10^{-12} sec, this requirement is always fulfilled (Frauenfelder and Steffen p 1002, 1966). In extreme cases perturbations are possible for lifetimes as short as ~ 10^{-11} sec. Considering the ^{56}Fe(n,n'gamma) reaction's kinematics we find that the recoil energy of the ^{56}Fe nucleus can be as high 175 keV for

back scattering of the 3 MeV incident neutrons (see Appendix A). This corresponds to an initial recoil velocity of 7.8×10^7 cm/sec which would allow a recoil distance in free space of 5×10^{-4} cm before the 0.847 MeV level decays ($t_{1/2} = 7 \times 10^{-12}$ sec). Of course the recoiling nucleus is not in a free space environment in this experiment and so can interact with surrounding atoms in the crystal structure. Interactions with electromagnetic fields in the vicinity of the recoiling nucleus cause the spin axis of the nucleus to precess. If the level lifetime is long enough for sufficient precession to take place the result will be an attenuation or smearing out of the anisotropy expected in the angular distribution. Fortunately, since the lifetime of the 0.847 MeV level is relatively short, we expect minimal attenuation of the angular distribution from these effects. Confirming this, as will become evident in Chapter IV, no discernable attenuation was observed in the experimental data.

In order to predict the outcome of a nuclear reaction, we need a model for the reaction mechanism. There are two principle reaction mechanisms that have been applied with considerable success to single nucleon reactions. The first is the direct interaction (DI) mechanism in which the target nucleus is pictured as a passive core with a nucleon or group of nucleons around it. It is the outer nucleons that interact with an incoming nucleon while the core contributes only elastic scattering. Such a reaction

proceeds very fast, typically 10^{-22} sec, which is approximately the nuclear traversal time for the incoming nucleon. The second reaction mechanism involves formation of a compound nucleus. An incoming nucleon enters the target nucleus, loses its individual identity as the "incoming" nucleon, and shares its energy with the ensemble of nucleons in the target creating a highly excited state of an intermediate nucleus referred to as a compound nucleus (CN). This nucleus lives until an individual nucleon or collection of nucleons, ie., an alpha particle, acquires enough energy by statistical fluctuations to escape the compound state, typically 10^{-16} sec, and cause its decay into an excited residual nucleus and the escaping nucleon (Marmier and Sheldon p 1091, 1970).

These reaction mechanisms represent two extreme views of how the reaction proceeds and it is not always clear which mechanism should be applied. In general, compound nucleus formation appears to predominate at energies below 6 MeV while direct interactions take precedence at energies above 12 MeV (Marmier and Sheldon p 1127, 1970). The energy region in between those limits can involve both mechanisms and the correct procedure for combining them is as yet unclear. Extensive (n,n'gamma) work has been carried out in the ~ 3 MeV region by other experimenters over a wide range of medium to heavy nuclei (Nellis and Morgan, 1974; Lachkar et al., 1974; Tessler and Glickstein, 1972; Cranberg et al., 1967; and many

others appearing in the bibliography). It has been found that in most cases the CN mechanism is very successful and provides better fits to experimental data than the DI mechanism (Kellie et al., 1973; Coope et al., 1977). This was also the conclusion of Sheldon in a paper which examined both mechanisms and compared them to experimental data (Sheldon p 796, 1963). It is this evidence that lead to the adoption of the CN approach in the analysis of the data obtained in this experiment at an incident neutron energy of ~ 3 MeV,

The next section in this chapter will discuss the CN reaction in greater detail and the calculation of theoretical angular distributions by application of the Wolfenstein-Hauser-Feshbach (WHF) statistical compound nucleus theory (Wolfenstein, 1951; Hauser and Feshbach, 1952; Feshbach et al., 1954). Then the numerical evaluation is outlined in Section 2-3 along with the results of those calculations for ^{56}Fe.

2-2 Statistical Compound Nuclear Theory

Before presenting the results of the WHF theory we must first take a look at the compound nucleus (CN) reaction in more detail and specify what it is that we wish the theory to predict. But first a note on the kinematics of the (n,n'gamma) reaction. Refer once more to Figure 2-1. In the lab system the nucleon is scattered by an angle θ_1 with respect to the incident direction while the gamma is

emitted at an angle θ_2 with respect to the incident direction. The differential cross sections of scattered nucleons and gammas are $d\sigma/d\Omega_1$ and $d\sigma/d\Omega_2$ respectively while the corresponding angular distributions, which are just the differential cross sections normalized to 1 at 90°, are $W(\theta_1)$ and $W(\theta_2)$. Differential cross sections are given in units of mb/sr and angular distributions are unitless. Because the masses of the target nuclei used here are so large, the lab angle $\theta_2 \sim \theta_2'$, where θ_2' is the center of mass (CM) angle. This also holds to a lesser degree for the nucleon angle θ_1. Therefore, θ_2 will be used in this presentation without reference to the explicit coordinate system used (see Appendix A).

An essential property of the CN theory is that the CN "forgets" how it was formed, that is, the exit channel that the CN decays through is independent of the entrance channel through which it was formed, except for conserved quantities discussed later. This "amnesia" assumption allows us to factor the cross section of a reaction proceeding via CN formation into separate formation and decay terms. Figure 2-2 shows the formation and decay of an excited CN formed through various entrance channels. For an inelastic scattering experiment the entrance channel is A + a and the exit channel of interest is A^* + a'. However, there are additional exit channels open for the CN to decay through. These include elastic scattering, inelastic scattering to different levels, and decays involving

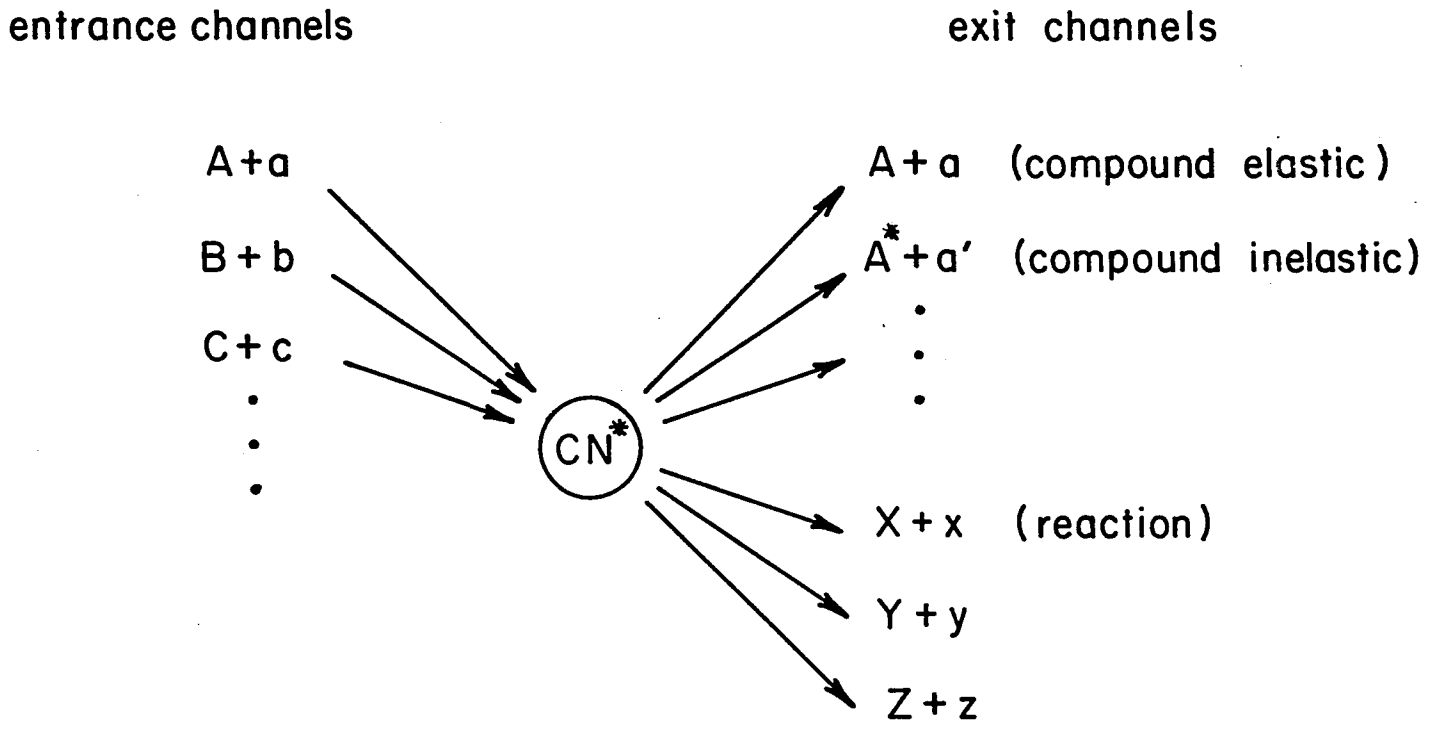
entrance channels
exit channels
A+a
B+b
C+c
CN*
A+a (compound elastic)
A*+a' (compound inelastic)
X+x (reaction)
Y+y
Z+z

FIGURE 2-2

different particles. The effect of these additional exit channels will have to be accounted for by the theory.

The excitation energy of the CN is given by

$$E^* = E_{CM} + B = m_A E_{lab}^{(a)} / (m_a + m_A) + B$$

where E_{cm} is the total CM energy available for the reaction, B is the binding energy difference between A and the CN, m_A and m_a are the masses of the target and projectile respectively, and $E_{lab}^{(a)}$ is the lab energy of the projectile. In the present work the excitation energy of the CN is generally high. For an ^{56}Fe target and 3 MeV incident neutron the CN is an excited ^{57}Fe nucleus with $E^* = 7.67$ MeV. If the CN is excited to a region where the energy levels are closely spaced and the energy spread of the projectile beam is wide enough, many CN levels will be excited. This fact will later become the basis for applying a statistical theory to the CN states. Again using an ^{57}Fe CN as an example we calulate the approximate number of levels excited. The average level spacing D, is given by (Sheldon p 845, 1963)

$$D = 0.0185\ A^2 (E^*+T)^2$$
$$\times \exp[-2(AE^*/11)^{1/2} - 0.094\ (11E^*)^{2/3}]$$

where T is the nuclear temperature in MeV

$$T = (4/A)\{1 + (1 + AE^*/2)^{1/2}\}$$

For ^{57}Fe excited to ~ 8 MeV, D = 0.36 keV. Thus if the

neutron energy spread is ~ 100 keV there are over 270 levels excited in ^{57}Fe.

Perhaps the most important information that we have on the CN reaction derives from conservation laws. In addition to energy and linear momentum conservation, it is clear that total angular momentum, the $\hat{z}$-component of total angular momentum, and parity of nuclear states are all conserved quantities. Conservation of total angular momentum and parity serve to limit, through selection rules, transitions between certain CN states and initial and final states. It is, however, the conservation of the $\hat{z}$-component of total angular momentum that causes the CN to "remember" the direction of the incident particles (Wolfenstein p 691, 1951). This preservation of alignment is responsible for anisotropic angular distributions. Figure 2-3 presents the (a,a'gamma) and (a,a'gamma-gamma) reactions in schematic form showing all angular momenta involved. A particle of total angular momentum $\vec{j}_1 = \vec{l}_1 + \vec{s}_1$ and a target nucleus of spin-parity $\vec{J}_0\pi_0$ form a CN of spin-parity $\vec{J}_1\pi_1$. Then the CN decays by emitting a particle of total angular momentum $\vec{j}_2 = \vec{l}_2 + \vec{s}_2$ leaving a residual nucleus in a state $\vec{J}_2\pi_2$ which decays itself by gamma emission of multipolarities L_2, L_2' to state $\vec{J}_3\pi_3$. In the case of the (n,n'gamma-gamma) reaction another transition with multipolarities L_3, L_3' can then occur to state $\vec{J}_4\pi_4$. Conservation of total angular momentum requires that

$$\vec{J}_0 + \vec{j}_1 = \vec{J}_1$$

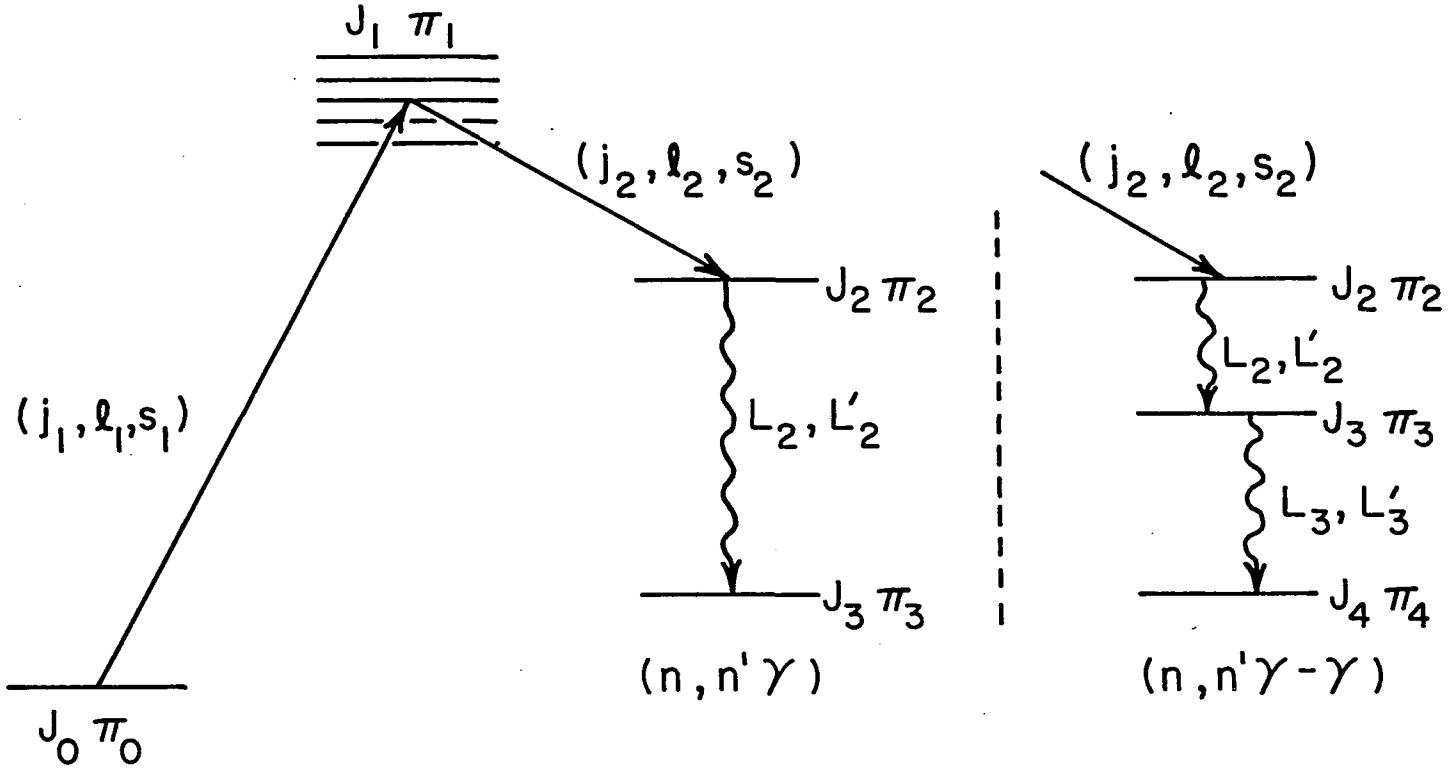
$J_1\ \pi_1$
(j_2, ℓ_2, s_2)
$J_2\ \pi_2$
L_2, L'_2
$J_3\ \pi_3$
$(n, n'\gamma)$
(j_1, ℓ_1, s_1)
$J_0\ \pi_0$
(j_2, ℓ_2, s_2)
$J_2\ \pi_2$
L_2, L'_2
$J_3\ \pi_3$
L_3, L'_3
$J_4\ \pi_4$
$(n, n'\gamma - \gamma)$

FIGURE 2-3

and

$$\vec{J}_1 = \vec{J}_2 + \vec{j}_2$$

In order to provide a picture of the alignment obtained relative to the incoming particle axis, we give a simplified, classical description of the (n,n'gamma) reaction. Consider a spinless particle of orbital angular momentum $\vec{l}_1$ striking a target nucleus of spin $\vec{J}_o = 0$. If we choose the $\hat{z}$ axis along the incident particle direction, then $\vec{p}$ is parallel to $\hat{z}$ and it is obvious that $l_{1z} = 0$ since $\vec{l} = \vec{r} \times \vec{p}$. This means that the $\vec{l}$ vector is confined to the x-y plane perpendicular to $\hat{z}$ at all times and so no additional $\hat{z}$-component of angular momentum can be transferred to the compound system. Thus the CN has total angular momentum $\vec{J}_1 = \vec{l}_1$ and $M_1 = 0$. At this point the CN has lost all memory of how it was formed except the values of J_1, π_1 and M_1. Now the CN can decay by emitting a neutron. The orbital angular momentum carried off by the outgoing neutron, l_2, can classically take on values from $l_2 = 0$ on up, however, the l_2 taken on is dependent upon the outgoing neutron energy. When the incoming neutron energy E_n is near the reaction threshold, the outgoing neutron energy $E_{n'}$ is low, and low values of l_2 are favored. In the $l_2 = 0$ case the residual nucleus is left spinning with the same orientation as the CN was given in the initial collision. That is, the excited residual nuclei will also have $\vec{J}_2$ confined to the x-y plane resulting in $M_2 = 0$ and are thus aligned. When these nuclei decay the corresponding

gamma distributions may be anisotropic, depending on the spin of the excited nuclear state, the ground state spin, and the multipolarity and mixing ratio of the gamma radiation.

Of course this picture is over simplified. The presence of partial waves higher than $l_2 = 0$ will tend to make the resulting distribution more isotropic because the $l_2 \neq 0$ neutrons can leave the residual nucleus in different, less perfectly aligned states with $M_2 \neq 0$. The degree of disalignment caused by higher l_2 is offset, however, by the decreasing numbers of higher l_2 neutrons with increasing l_2.

We can obtain an estimate of the most probable l values available for incident as well as scattered neutrons at different energies by assuming that a reaction only occurs when a neutron is within range of the nuclear force, ie., within radius $b \sim r_o A^{1/3}$. Then the energy as a function of l is given by

$$E \sim l(l + 1)\, \hbar^2/2m_n b^2$$

Using r = 1.4 fm we find for ^{56}Fe

l	E (MeV)
1	1.4
2	4.3
3	8.6

These figures imply that a 3 MeV neutron and ^{56}Fe nucleus cannot interact with an l greater than about 2, however, we

must consider that the nuclear density distribution is not a step function with a sharp cut off. The use of a more smoothly cut off nuclear distribution allows some interaction at a greater radius and thus higher partial waves can participate for a given E_n. In Section 2-3 we show how various partial waves contribute to the reaction and values of l_{1max} and l_{2max} are chosen.

The addition of particle spin to the above description also tends to destroy the anisotropy of the distribution. As in the case of $l_2 \neq 0$ partial waves, the inclusion of nucleon as well as target nucleus spin allows for more orientations of $\vec{J}_2$ and consequently a more isotropic distribution. Thus the most anisotropic distributions are obtained from conditions of $\vec{J}_o = 0$ and E_n near threshold.

Now we consider the application of a specific model to the CN system. As pointed out previously, a great number of broad, overlapping states are excited in the CN at this energy. For this reason attempts to treat the excited CN levels individually fail. Thus we turn to the WHF statistical model to analyze this quasi-continuum of levels. A complete derivation of differential cross sections using this statistical model is beyond the scope of this paper, but, the essential simplification achieved by employing the WHF approach is the elimination of interference terms between incoming partial waves with each other and of outgoing partial waves with each other. Cancellation of

these terms comes about as a consequence of summing over the large number of random phases present in the wavefunctions of the many excited CN states (Hauser and Feshbach p 367, 1952). This greatly reduces the complexity of the sums involved over incoming and outgoing partial waves.

In general, the differential cross sections for either the scattered particles or gamma rays can be expressed as

$$d\sigma/d\Omega = \sum a_\nu \; P_\nu(\cos\theta)$$

where ν is even and its range is determined by vector momentum coupling conditions. The fact that ν takes on only even values is expected from parity conservation which requires symmetry about $\theta = 90^0$. This symmetry is characteristic of the statistical model since averaging has destroyed sense of direction, ie., forward and backward with respect to 90^0 (Marmier and Sheldon p 1187, 1970). Following Sheldon's formalism the a_ν can be factored into energy dependent and momentum dependent terms (Sheldon and Van Patter p 144, 1966)

$$a_\nu = \sum_i \alpha_{i\nu} \tau_i$$

The energy dependent terms are contained in

$$\tau = T_{j_1 l_1}(E_1) \; T_{j_2 l_2}(E_2) \; / \sum T_{jl}(E)$$

where the T_{jl} are energy dependent transmission factors (see Appendix B). The factor $T_{j_1 l_1}(E_1)$ represents the formation of

the CN through channel 1 with orbital angular momentum l_1. The remaining factor in τ,

$$T_{j_2 l_2}(E_2) \; / \sum T_{jl}(E)$$

is the probability that the CN will decay via channel 2 with orbital angular momentum l_2. The sum in the denominator of τ is over all possible exit channels including elastic scattering.

The momentum dependent terms are called "linking parameters" that describe each transition in the reaction. Each step, be it a particle or gamma transition, in the reaction is described by a linking parameter. For instance, the (n,n'gamma) reaction has three transitions involved in it. First is the particle transition that creates the CN from an incoming neutron and target nucleus. Then there is another particle transition when the CN decays emitting a neutron. Finally, there is the gamma transition as the residual nucleus decays emitting a gamma ray. For a particle transition we use the $\eta_\nu(jj'J_i J_f)$ which describe a transition in the target nucleus caused by a particle of initial total angular momentum j and final total angular momentum j' from spin J_i to J_f of the nucleus. For an observed gamma transition from J_i to J_f by emission of a photon of multipolities L and L', we use $A_\nu(L\ L'J_i\ J_f)$. Finally, to describe an unobserved gamma transition as in the (n,n'gamma-gamma) reaction, we use the $U_\nu(L\ L'J_i\ J_f)$ where the notation is the same as for the A_ν. The U_ν are actually

independent of the nature of the unobserved radiation so $U_\nu(jj'J_i J_f)$ is used to describe an unobserved transition due to a particle. These three quantities can all be expressed in terms of Racah coefficients involving the spins, multipolarities, and the mixing ratio

$$\delta = \langle J_f \| L' \| J_i \rangle / \langle J_f \| L \| J_i \rangle$$

For the (n,n'gamma) reaction we are interested in the sequence

$$J_0\pi_0 (j_1 = l_1 \pm 1/2) \rightarrow J_1\pi_1 \rightarrow (j_2 = l_2 \pm 1/2)\ J_2\pi_2 \rightarrow (L_2, L_2')\ J_3\pi_3$$

as shown in Figure 2-3. The differential cross section for the gammas will involve linking parameters

$$\lambda_\nu(j_1\, j_1\, J_0\, J_1)\ U_\nu(j_2\, j_2\, J_2\, J_1)\ A_\nu(L_2\, L_2'\, J_3\, J_2)$$

here the U_ν is included because the scattered nucleon is not observed and no information on its scattering angle is available.

For the (n,n'gamma-gamma) reaction, important in making cascade corrections, we have the sequence

$$J_0\pi_0 (j_1 = l_1 \pm 1/2) \rightarrow J_1\pi_1 \rightarrow (j_2 = l_2 \pm 1/2)\ J_2\pi_2 \rightarrow (L_2 L_2')\ J_3\pi_3 \rightarrow (L_3 L_3')\ J_4\pi_4$$

which has the following angular momentum factors

$$\lambda_\nu(j_1\, j_1\, J_0\, J_1)\ U_\nu(j_2\, j_2\, J_2\, J_1)\ U_\nu(L_2 L_2' J_3\, J_2)\ A_\nu(L_3 L_3' J_4\, J_3)$$

Multiplying these factors together and summing over j_1, j_2 and ν, we obtain differential cross section for the

above cases. The gamma differential cross section is

$$d\sigma/d\Omega = \frac{\lambda^2}{4}\sum g\, \eta_\nu(j_1\, j_1\, J_0\, J_1)\; U_\nu(j_2\, j_2\, J_2\, J_1)$$
$$\times\; A_\nu(L_2\, L_2'\, J_3\, J_2)\; \tau\; P_\nu(\cos\theta_2)$$

where g is a statistical spin factor, λ is the rationalized wavelength of the incident particle in the CM system and θ_2 is the scattering angle referred to the incident direction. The Racah coefficients contained in η_ν, U_ν and A_ν restrict ν such that $0 \le \nu \le 2j_1,\ 2J_1,\ 2J_2,\ 2L_2'$.

For the observed gamma differential cross section in the (n,n'gamma-gamma) reaction we have

$$d\sigma/d\Omega = \frac{\lambda^2}{4}\sum g\, \eta_\nu(j_1\, j_1\, J_0\, J_1)\; U_\nu(j_2\, j_2\, J_2\, J_1)\; U_\nu(L_2\, L_2'\, J_3\, J_2)$$
$$\times\; A_\nu(L_3\, L_3'\, J_4\, J_3)\; \tau\; P_\nu(\cos\theta_2)$$

where $0 \le \nu \le 2j_1,\ 2J_1,\ 2J_2,\ 2J_3,\ 2L_3'$.

At this point we have expressions for the differential cross sections required in terms of the angular momenta involved and the transmission coefficients T_{jl}. The next task is to calculate these differential cross sections, which is the topic of Section 2-3.

2-3 Numerical Evaluation of Differential Cross Sections

This section will concern itself with an outline of the method used to calculate differential cross sections. Angular distributions are then obtained from the differential cross sections by simply normalizing the differential cross section to 1.0 at 90°. The results of

these calculations will be illustrated using the $^{56}Fe(n,n'gamma)^{56}Fe$ reaction by varying the nuclear potential parameters used, the incident neutron energy, the maximum number of incoming and outgoing partial waves included, and the number of extra exit channels accounted for. The effect of these parameter variations will be presented in graphic form. Then cascade corrections to the angular distributions will be discussed and final theoretical angular distributions given for ^{56}Fe.

Two computer programs were used in the numerical differential cross section evaluations. The first, SCAT, is a Fortran program which calculates the transmission coefficients T_{jl} from an optical model potential consisting of a complex Woods-Saxon nuclear potential with spin-orbit coupling included (Smith, 1969). For a particular set of optical model potential parameters, calculation of the T_{jl} is implemented by stepping out a solution to Schrödinger's equation from the origin to a point outside the nuclear potential and matching that solution to a linear combination of regular and irregular asymptotic Coulomb wave functions. For neutron scattering the asymptotic Coulomb functions reduce to regular and irregular spherical Bessel functions (Marmier and Sheldon p 1224, 1970). The T_{jl} are then derived from the boundary matching coefficients (see Appendix C). The T_{jl} are used as input data to the Fortran program MANDYF which calculates the differential cross section by the WHF theory as outlined in Section 2-2

(Sheldon and Donati, 1971). MANDYF has provision for calculating total cross sections, differential cross sections, and angular distributions as well as various intermediate parameters for reactions of the type (a,b), (a,b gamma), and (a,b gamma-gamma). Orbital angular momenta up to $l_{max} = 8$ are allowed with up to 40 extra exit channels included.

Utilizing the T_{jl} calculated by SCAT, and other input parameters such as energies, multipolarities, mixing ratios, spins and parities, MANDYF calculates the Racah coefficients in the K_ν, A_ν and U_ν, calculates the sums involved in τ, and performs the sums in the differential cross section that are allowed by angular momentum and parity selection rules (see Appendix D). As mentioned previously, in an experiment where polarization of radiation is undetected, parity does not influence the angular distribution directly. Only by limiting, through the parity selection rule, the l_1 and l_2 which can participate in the reaction does parity have any effect on the angular distribution. This effect was checked by calculating angular distributions for different parities and, as reported by Sheldon, was found to be minimal (Sheldon and Van Patter p 166, 1966). Thus we cannot make parity assignments from the results of this experiment. In all remaining calculations the probable parities given in Nuclear Data Sheets energy level diagrams were chosen.

Output from MANDYF begins with a complete listing of

the input parameters followed by some intermediate results such as the a_γ referred to in Section 2-2 and the B_γ to be discussed in connection with the data analysis program in Chapter IV. Finally MANDYF outputs the differential cross section and normalized angular distributions and sums the differential cross section to arrive at the total cross section.

In order to demonstrate the use of SCAT and MANDYF we shall evaluate the differential cross sections for inelastic scattering of neutrons on ^{56}Fe. The low lying levels of ^{56}Fe are shown in Figure 2-4. The principal level of interest here is the 0.847 MeV, +2 level. In order to calculate the gamma angular distribution from this level we must first select a set of optical model parameters as input to SCAT. Several sets of these parameters, determined from elastic scattering, were selected from a compilation by Perey, and $T_{j\ell}$ were calculated from them (Perey and Perey, 1976). Figure 2-5 shows the results of this test. Clearly, there is little difference in the angular distributions predicted by these optical parameters except for that predicted by the Becchetti parameters. This variation is probably due to the fact that the Becchetti parameters derive from fits to elastic scattering at E_n = 15 - 24 MeV whereas the remaining optical parameters result from elastic scattering in the 3 MeV region. The Wilmore and Hodgson parameters were chosen for this analysis simply because of their successful, wide-spread use and acceptance by other

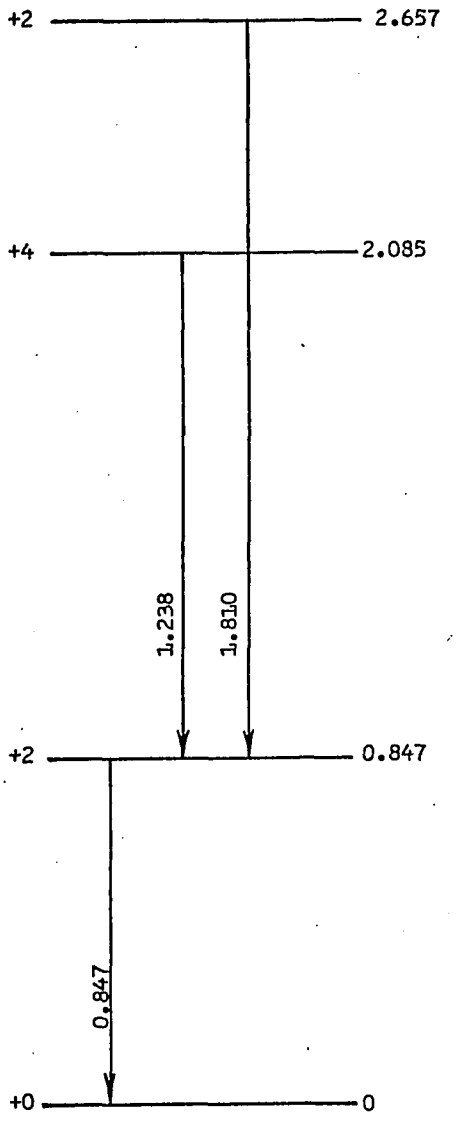

$^{56}_{26}Fe$

FIGURE 2-4

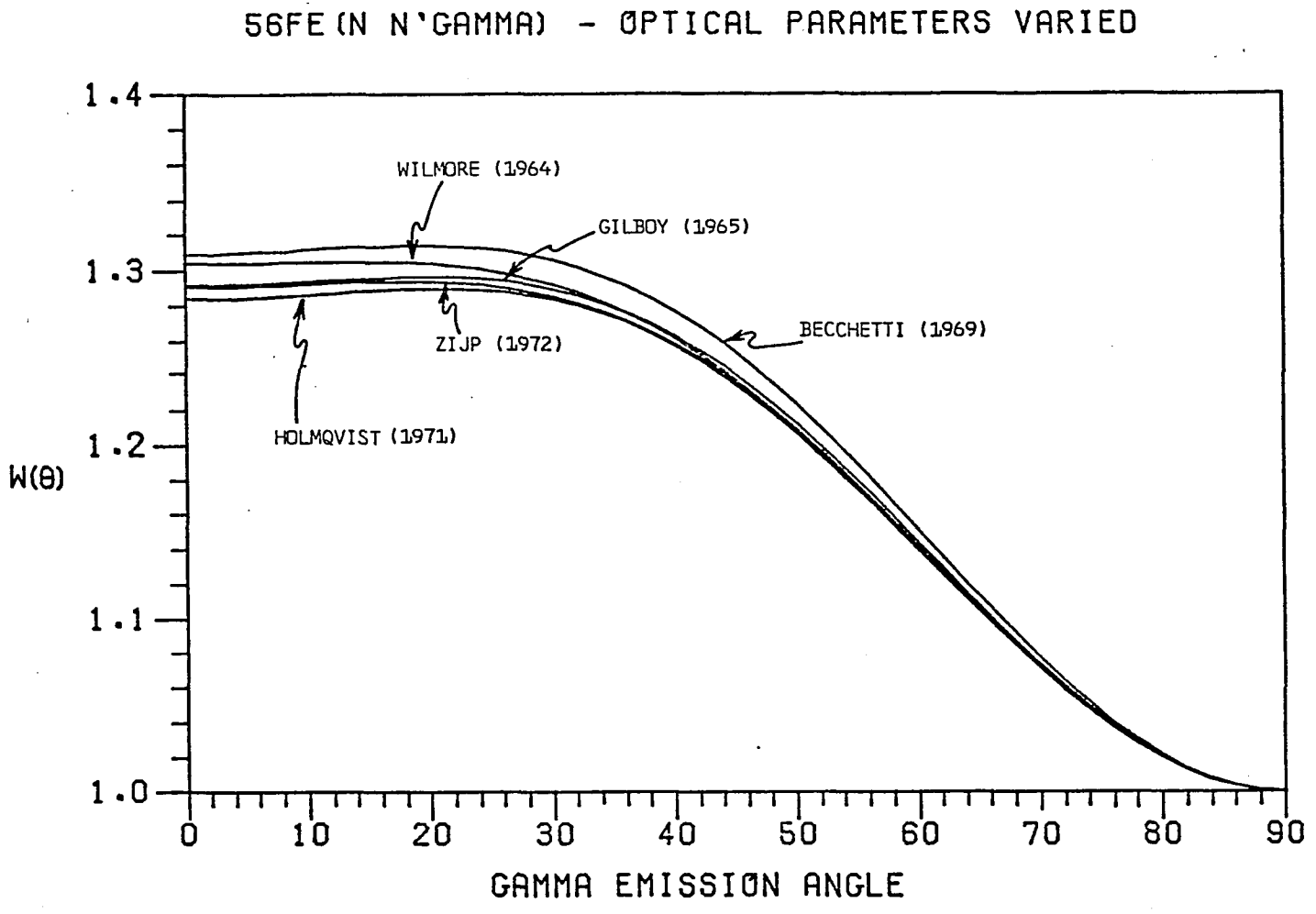
56FE(N N'GAMMA) - OPTICAL PARAMETERS VARIED
1.4
1.3
1.2
1.1
1.0
W(θ)
WILMORE (1964)
GILBOY (1965)
BECCHETTI (1969)
ZIJP (1972)
HOLMQVIST (1971)
0
10
20
30
40
50
60
70
80
90
GAMMA EMISSION ANGLE

FIGURE 2-5

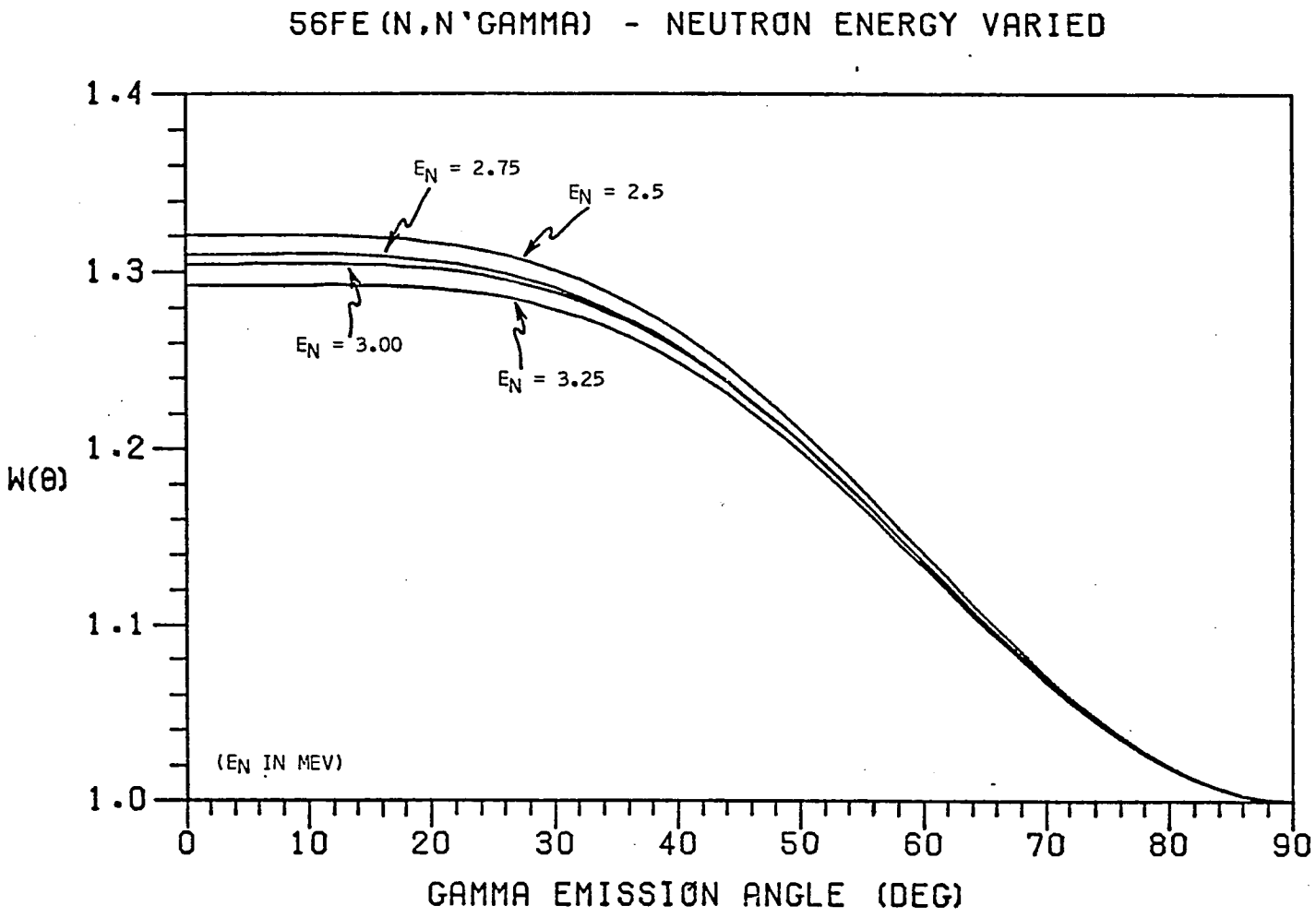
56FE(N,N'GAMMA) - NEUTRON ENERGY VARIED
1.4
1.3
1.2
1.1
1.0
W(θ)
E_N = 2.75
E_N = 2.5
E_N = 3.00
E_N = 3.25
(E_N IN MEV)
0
10
20
30
40
50
60
70
80
90
GAMMA EMISSION ANGLE (DEG)

FIGURE 2-6

experimenters.

Another variable of importance here is the incident neutron energy E_n. The values of the T_{jl} are dependent upon neutron energy. Figure 2-6 indicates that the variation of E_n from 2.5 - 3.25 MeV produces only a small change in the angular distribution. Even so, this variation was included in the analysis, as will be fully explained in Chapter IV. For the remaining examples in this chapter the incident energy will be set at 3.0 MeV.

The calculation of the angular distribution involves sums over possible values of l_1 and l_2 with a maximums of l_{1max} and l_{2max} respectively. It is important to insure that the l_{max} are high enough to include all contributing terms. Figure 2-7 shows that the angular distribution becomes slightly more anisotropic with increasing l_{1max} but that $l_{1max} = 4$ and $l_{1max} = 5$ produce indistinguishable results. Figure 2-8 confirms the smoothing out of the angular distribution as l_{2max} is increased. As the exiting neutron is allowed to carry away more orbital angular momentum, the residual nucleus is left in more possible orientations of $\vec{J}_2$. Then the sum over these possible values of $\vec{J}_2$ causes the angular distribution to tend toward the isotropy expected if there were no alignment. Both l_{1max} and l_{2max} are set to 5 in the remaining calculations.

As mentioned previously, additional exit channels for the reaction must also be included in the calculation of the differential cross section. The inclusion of extra exit

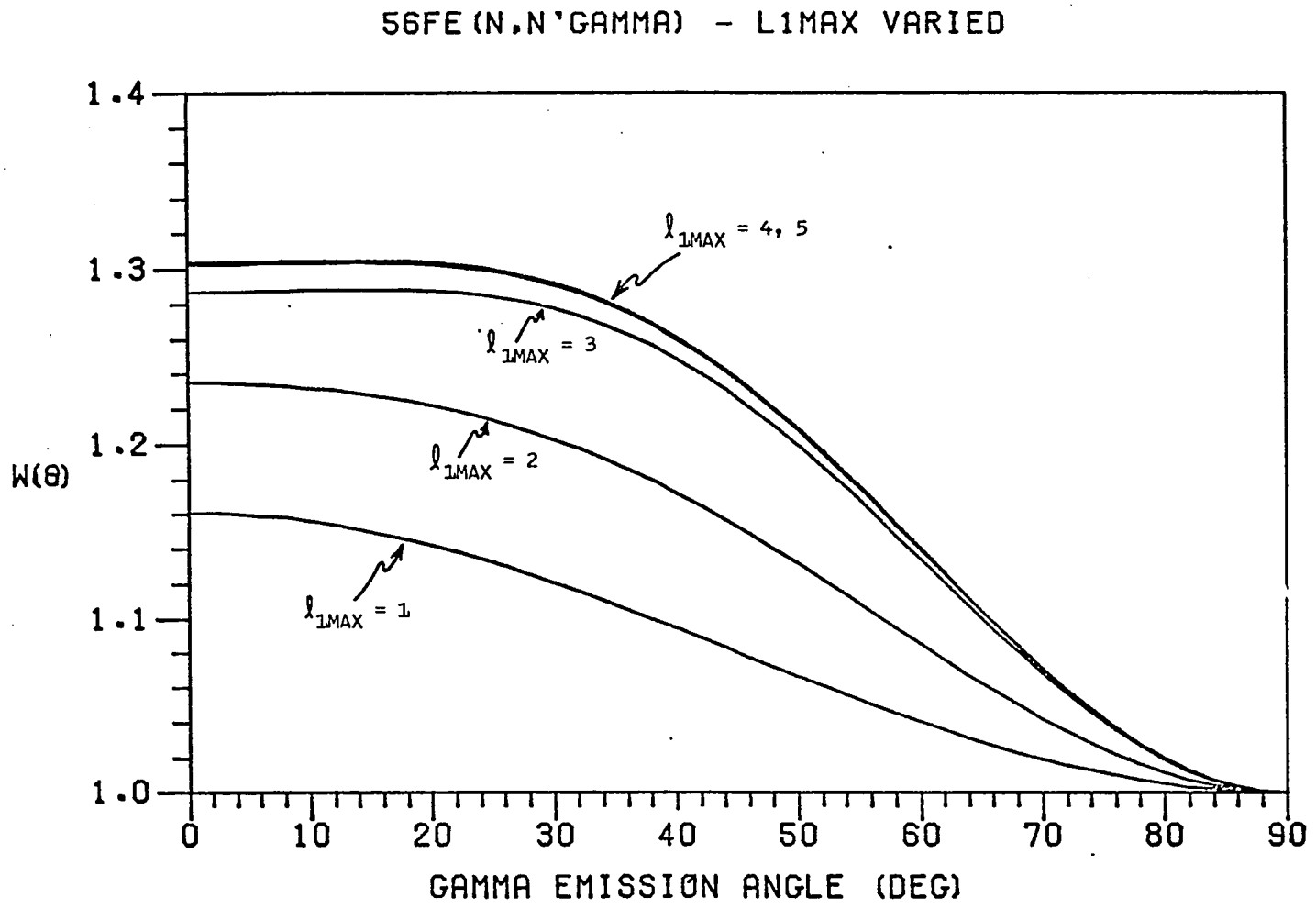
56FE(N,N'GAMMA) - L1MAX VARIED
1.4
1.3
1.2
1.1
1.0
W(θ)
ℓ_{1MAX} = 4, 5
ℓ_{1MAX} = 3
ℓ_{1MAX} = 2
ℓ_{1MAX} = 1
0
10
20
30
40
50
60
70
80
90
GAMMA EMISSION ANGLE (DEG)

FIGURE 2-7

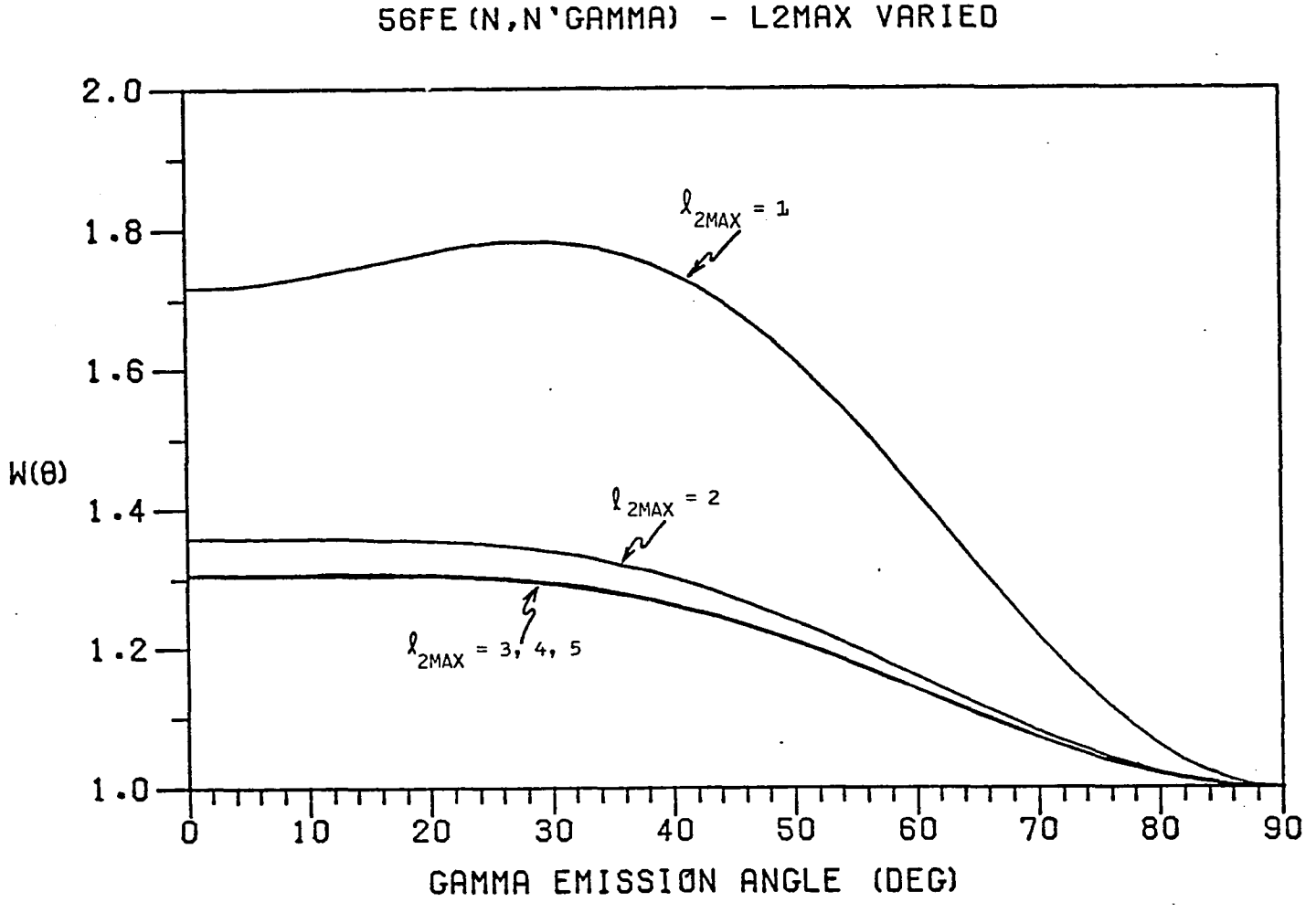
56FE(N,N'GAMMA) - L2MAX VARIED
2.0
1.8
1.6
1.4
1.2
1.0
W(θ)
ℓ2MAX = 1
ℓ2MAX = 2
ℓ2MAX = 3, 4, 5
0
10
20
30
40
50
60
70
80
90
GAMMA EMISSION ANGLE (DEG)

FIGURE 2-8

channels, other than the elastic exit channel which is always included, influences the differential cross section through τ because the probability of the reaction proceeding through a particular exit channel is proportional to

$$T_{j_2 l_2}(E_2) / \sum T_{jl}(E)$$

As more exit channels are included, the denominator becomes larger and the probability for exit through channel 2 becomes smaller. Thus extra exit channels tend to decrease the differential cross section appreciably without having as pronounced an effect on the angular distribution. The effect of including one and then two additional exit channels in the ^{56}Fe differential cross section is illustrated in Figure 2-9 while the effect on the angular distribution is shown in Figure 2-10. The extra exit channels included are first the inelastic scattering channel to the 2.085 MeV, +4 and second to the 2.657 MeV, +2 levels of ^{56}Fe.

Finally, we consider the effect of cascading from higher levels. The 3 MeV neutrons used in this experiment easily excite the 2.085 MeV and 2.657 MeV levels in ^{56}Fe both of which decay to ground via the 0.847 MeV level. To correct for this population of the 0.847 MeV level, we calculate the differential cross section for the (n,n'gamma-gamma) reaction from each cascade level. The first gamma transition is unobserved and corresponds to decay from the 2.085 MeV or 2.657 MeV levels to the

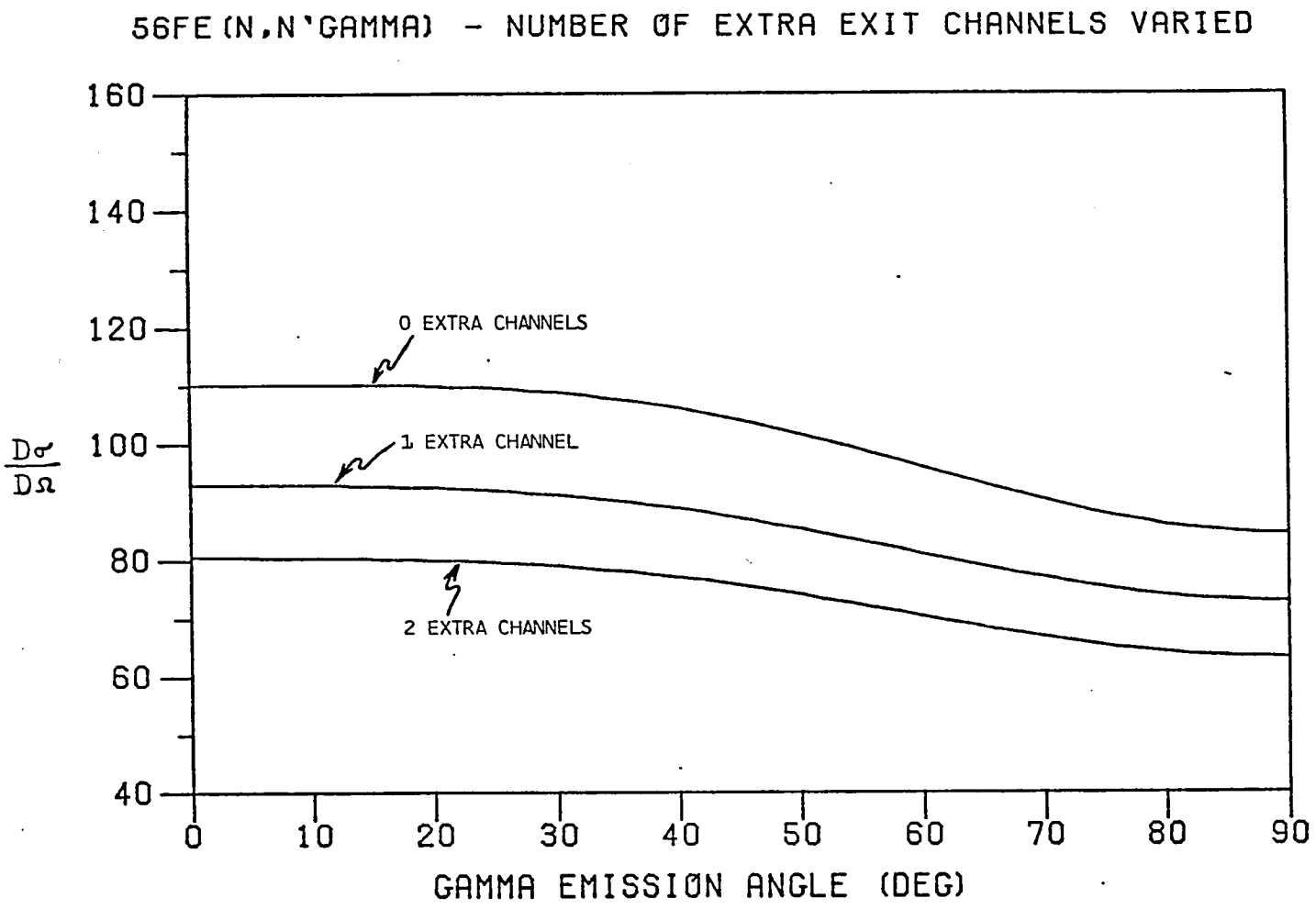
56FE(N,N'GAMMA) - NUMBER OF EXTRA EXIT CHANNELS VARIED
160
140
120
100
80
60
40
Dσ/DΩ
0 EXTRA CHANNELS
1 EXTRA CHANNEL
2 EXTRA CHANNELS
0
10
20
30
40
50
60
70
80
90
GAMMA EMISSION ANGLE (DEG)

FIGURE 2-9

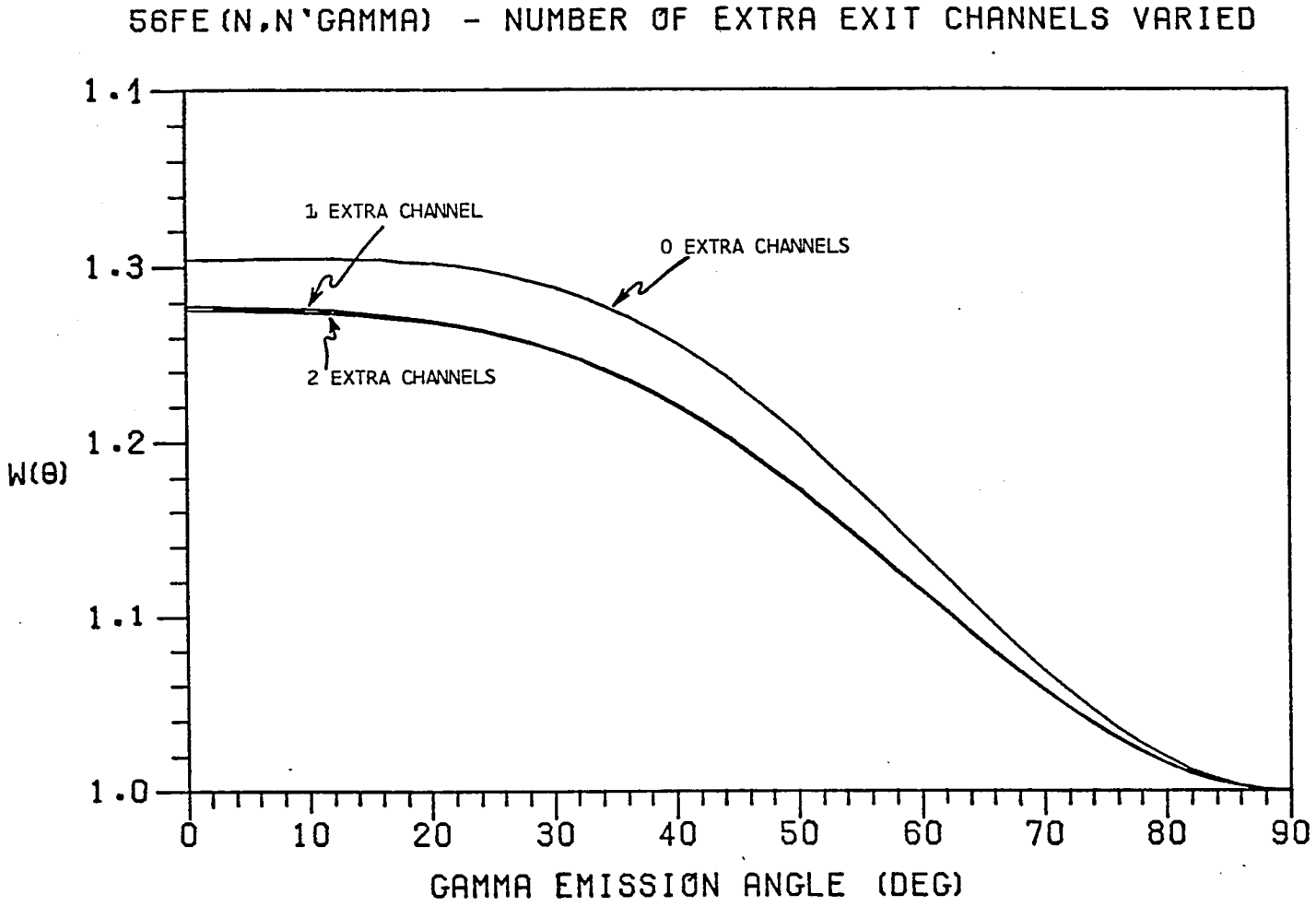
56FE(N,N'GAMMA) - NUMBER OF EXTRA EXIT CHANNELS VARIED
1.1
1.3
1.2
1.1
1.0
W(θ)
1 EXTRA CHANNEL
0 EXTRA CHANNELS
2 EXTRA CHANNELS
0
10
20
30
40
50
60
70
80
90
GAMMA EMISSION ANGLE (DEG)

FIGURE 2-10

0.847 MeV level. The second transition corresponds to decay from the 0.847 MeV level to ground, which is the observed transition. These contributions are calculated separately and summed with each level's contribution weighted by its excitation cross section and branching ratio to produce the angular distribution that should be observed experimentally (Sen Gupta and Van Patter, 1964; Mohindra and Van Patter, 1965; Sheldon and Van Patter p 162, 1966). Figure 2-11 shows the contributions to the angular distribution of the 0.847 MeV level obtained for the three transitions separately where the spin of the 0.847 MeV level has been set to +2. As indicated by Figure 2-11, both cascade sequences are anisotropic in the same way as the main sequence, 0.847 MeV (+2) → G.S. (+0). This causes the observed distribution of 0.847 MeV gammas to be more anisotropic than if cascading were neglected.

The major drawback to this cascade correction approach is that it requires prior knowledge of the spins, parities, and excitation cross sections of upper levels, as well as the branching ratios in the decay schemes. This points out the desirability of a neutron source of variable energy that could be used to excite levels only up to the level being studied. The importance of cascade corrections for ^{56}Fe will become evident when the experimental data is presented in Chapter IV. To conclude the ^{56}Fe differential cross section evaluation, we summarize the results in Figures 2-12 and 2-13. Figure 2-12 shows the effect of

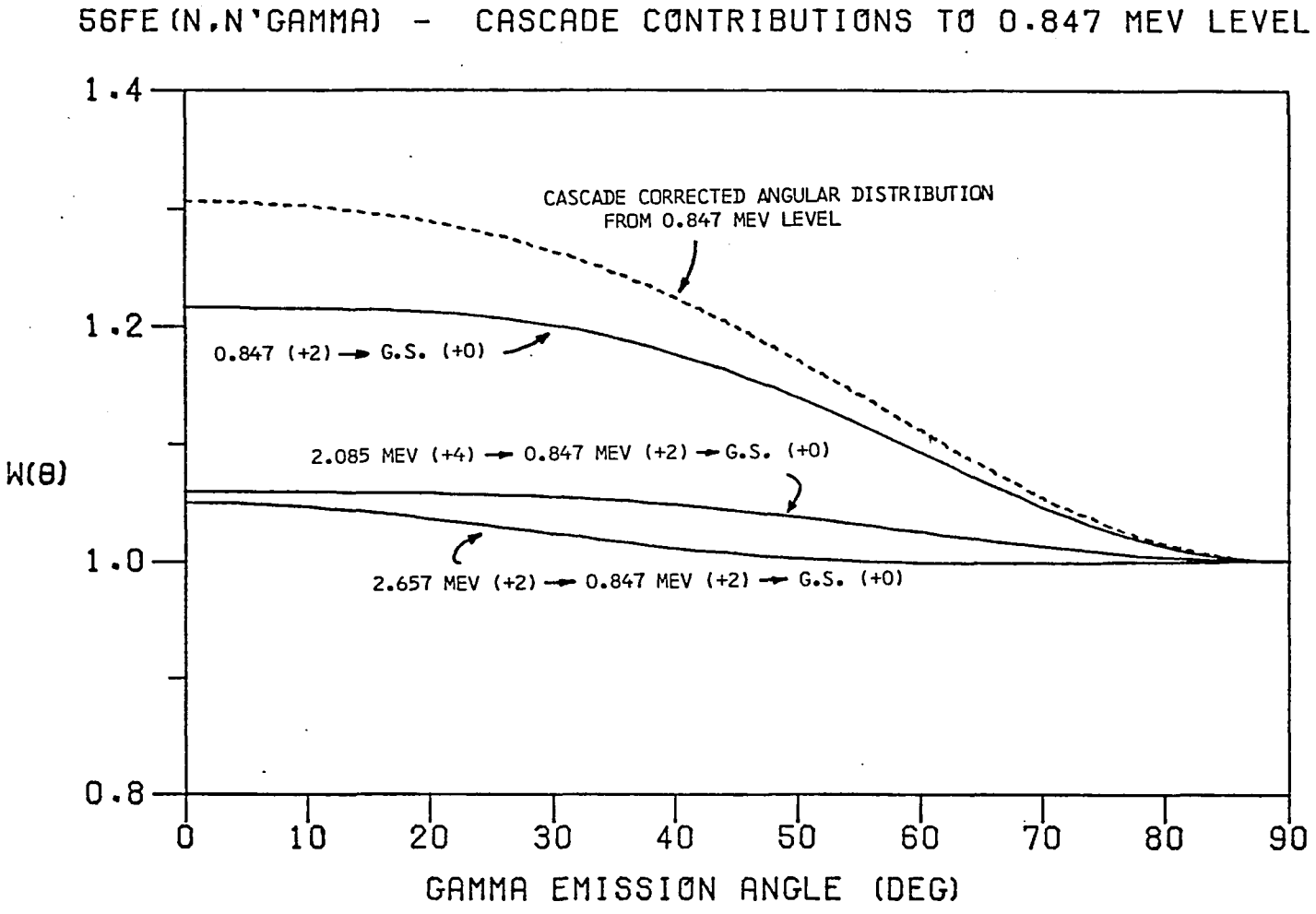
56FE(N,N'GAMMA) - CASCADE CONTRIBUTIONS TO 0.847 MEV LEVEL
1.4
1.2
1.0
0.8
W(θ)
CASCADE CORRECTED ANGULAR DISTRIBUTION
FROM 0.847 MEV LEVEL
0.847 (+2) → G.S. (+0)
2.085 MEV (+4) → 0.847 MEV (+2) → G.S. (+0)
2.657 MEV (+2) → 0.847 MEV (+2) → G.S. (+0)
0
10
20
30
40
50
60
70
80
90
GAMMA EMISSION ANGLE (DEG)

FIGURE 2-11

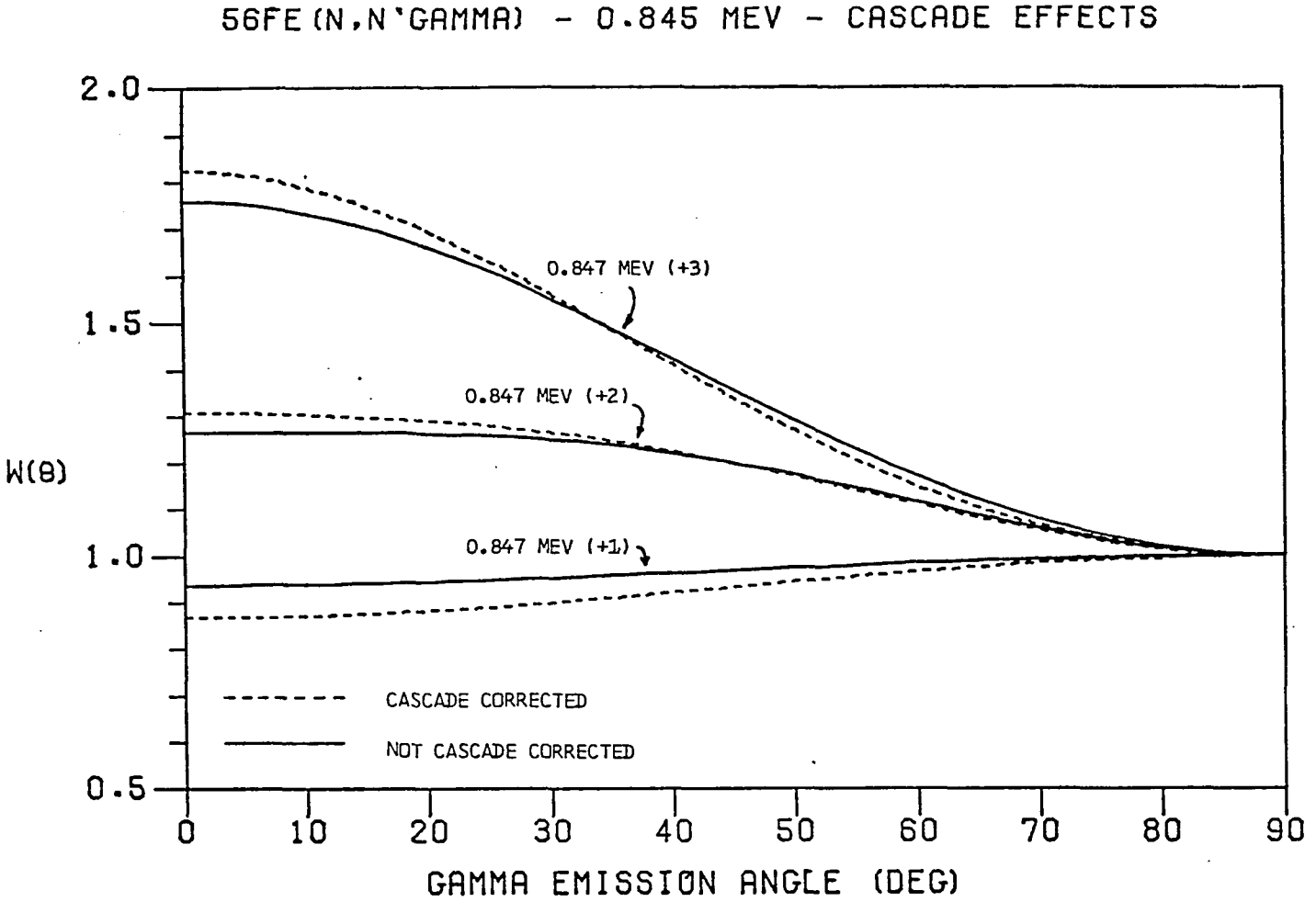
56FE(N,N'GAMMA) - 0.845 MEV - CASCADE EFFECTS
2.0
1.5
1.0
0.5
W(θ)
0.847 MEV (+3)
0.847 MEV (+2)
0.847 MEV (+1)
CASCADE CORRECTED
NOT CASCADE CORRECTED
0
10
20
30
40
50
60
70
80
90
GAMMA EMISSION ANGLE (DEG)

FIGURE 2-12

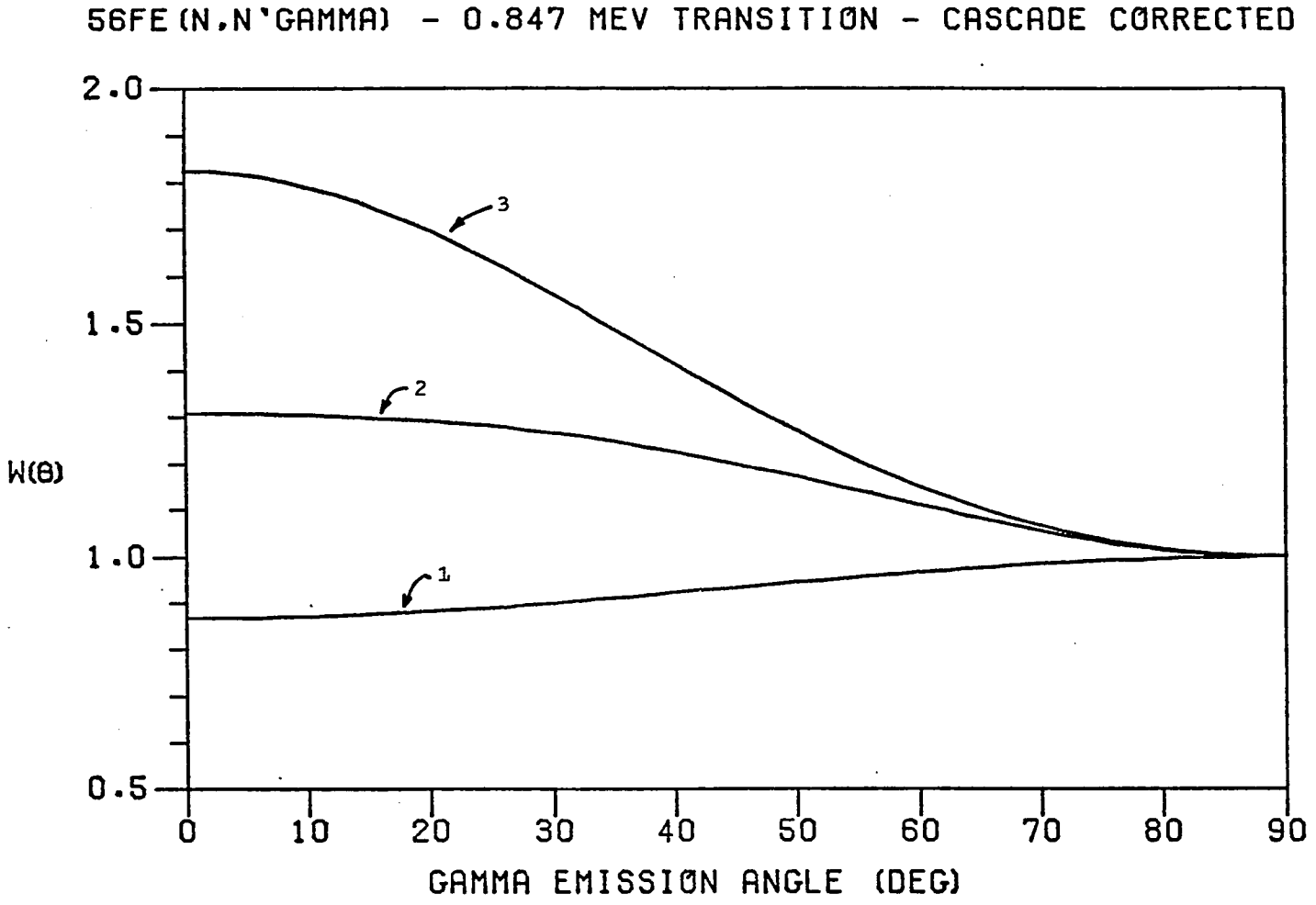
56FE(N,N'GAMMA) - 0.847 MEV TRANSITION - CASCADE CORRECTED
2.0
1.5
1.0
0.5
W(θ)
3
2
1
0
10
20
30
40
50
60
70
80
90
GAMMA EMISSION ANGLE (DEG)

FIGURE 2-13

cascade corrections on the angular distribution for three hypothesized spins of the 0.847 MeV level. The spin of the 0.847 MeV level is varied from +1 to +3 while the cascade level spins are held at the previously given values of +4 and +2. The solid lines in Figure 2-12 represent the angular distribution without cascade effects included while the dashed lines include the cascade correction. Finally, Figure 2-13 gives the cascade corrected theoretical angular distributions for hypothesized 0.847 MeV level spins +1, +2, +3. These distributions include the two extra exit channels discussed above and cascades from those two higher levels. It is these angular distributions that will be compared with experimental data in Chapter IV to confirm that the spin of the 0.847 MeV is indeed +2.

III. EXPERIMENTAL

3-1 Introduction

This chapter discusses the experimental setup and procedures used in this research. Section 3-2 describes the accelerator facility and the production of a deuteron beam for use in the neutron production reaction. Section 3-3 then describes the pulsing system, and Section 3-4 the actual target assembly and experimental area. Section 3-5 gives a detailed account of the electronics and timing considerations relevant to this research. Both energy and efficiency calibration are discussed in Section 3-6 and the actual data acquisition procedure is described in Section 3-7.

3-2 The Accelerator Facility

The University of New Hampshire operates a 400 keV positive ion Van de Graaff accelerator manufactured by High Voltage Engineering of Burlington, Massachusetts. In order to provide adequate shielding from X-rays and neutrons produced by the accelerator it is located underground while the control room is aboveground and offset from it.

A diagram of the accelerator room as it was set up for this experiment is shown in Figure 3-1.

Two high yield neutron producing reactions are available on the UNH accelerator. The $t(d,n)^4He$ reaction (Q = +17.5785 MeV) produces ~ 14 MeV neutrons and the $d(d,n)^3He$ reaction (Q = +3.2688 MeV) produces ~ 3.0 MeV neutrons. For the present (n,n'gamma) experiment the lower energy neutrons were preferred because they would excite levels up to 3 MeV, the energy region of interest, and not excite higher levels that complicate the analysis by cascading down and populating the level being studied. In addition, 14 MeV neutrons could initiate competing reactions such as (n,p), (n,alpha), and (n,2n) that would also complicate the analysis and whose threshold energies are generally above 3 MeV. Neutrons with energies ranging from 3.05 MeV at 0° to 2.45 MeV at 90° can be produced using a thick TiD target (Seagrave, 1957).

A potential of 300 kV is produced at the high voltage terminal end of the accelerator by transferring charge from ground potential to the insulated high voltage terminal end. This is implemented by spraying electrons onto a fast moving rubberized belt and collecting them again at the high voltage terminal. This terminal is isolated from ground by the column, a series of ten alternating glass and metal rings interconnected by dropping resistors. The center of the column forms a vacuum tube down which particles can pass and, in doing so, travel through a

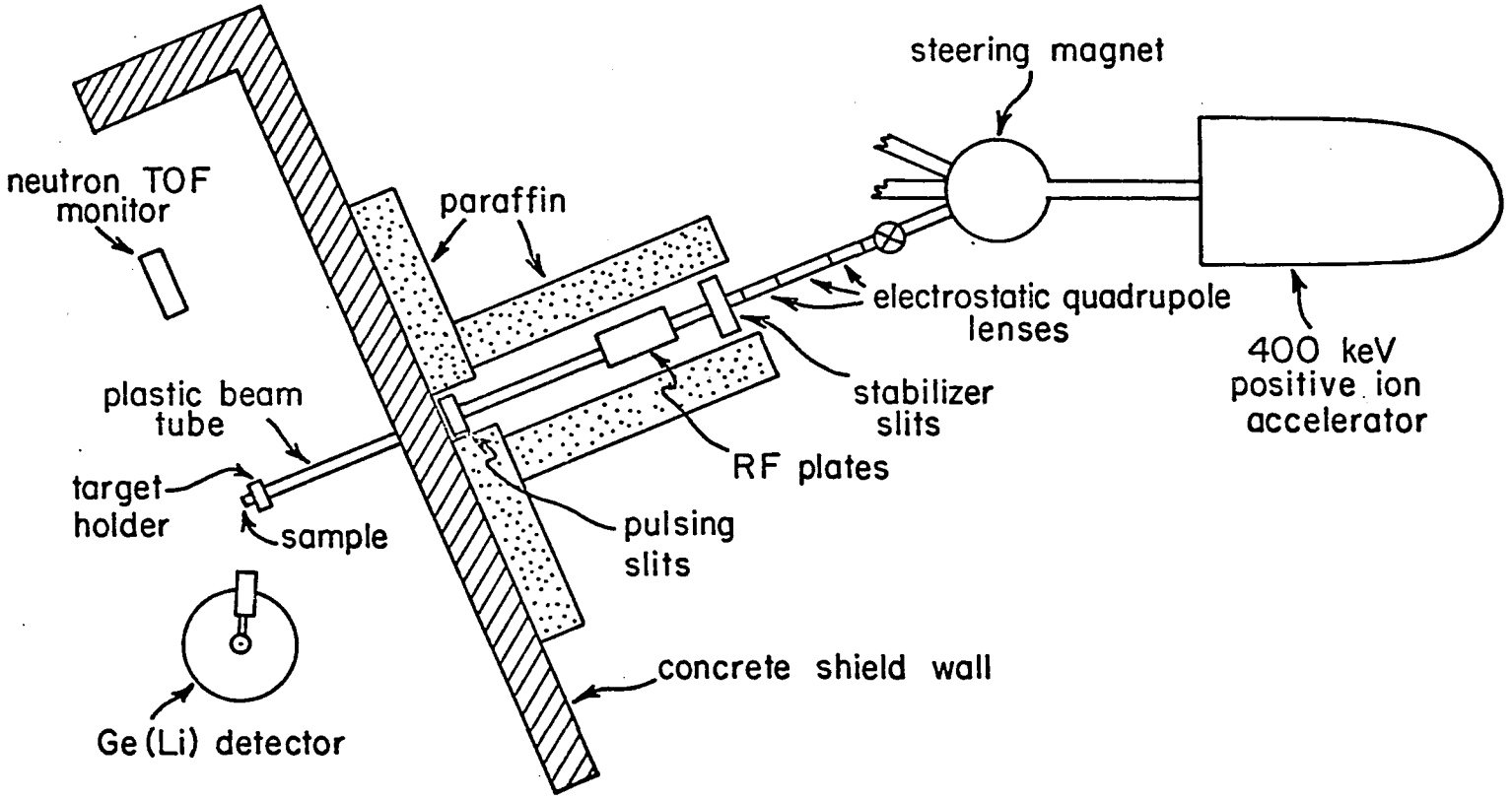
steering magnet
neutron TOF monitor
paraffin
electrostatic quadrupole lenses
400 keV positive ion accelerator
plastic beam tube
stabilizer slits
RF plates
target holder
sample
pulsing slits
concrete shield wall
Ge (Li) detector

FIGURE 3-1

potential drop of 300 kV. A deuteron beam is produced by ionizing deuterium gas with an RF source at the high voltage terminal end of the accelerator and injecting the resulting deuterons into the column where they accelerate through the potential . After leaving the column, the 300 keV deuteron beam enters the steering magnet where it can be analyzed and bent 15° down the left or right ports to seperate experiments, or left unanalyzed and allowed to enter the center port. In this experiment the left port was used exclusively.

In the left port, the beam first passes through an electrostatic quadrupole lens where it is focused by an electric field. Downstream from the quadrupole lens a portion of the beam is collected by a pair of stabilizer slits. Excessive signal in the high (low) energy slit circuit feeds back to the corona points located on the side of the accelerator tank and causes them to drain more (less) current from the high voltage terminal and thus decrease (increase) terminal voltage and return the beam to the center of the left port. The accelerator is also equipped with a capacitive pickup unit located at the rear of the accelerator tank which senses ripple in the terminal voltage and sends a cancellation signal to the corona points to reduce the ripple. The combination of these stabilizer systems results in an analyzed deuteron beam of 20 - 30 microamps current with typical ripple and drift of ± 1 keV.

3-3 The Beam Pulsing System

The beam pulsing apparatus described in this section is used to facilitate the time-of-flight (TOF) systems used in energy analysis and neutron monitoring. (The TOF systems are discussed in Section 3-5.)

An oscillating electric field is created between a pair of parallel brass plates by grounding the upper plate, and applying a high voltage 5.5 MHz signal to the lower plate with a radio frequency (RF) generator, a wideband RF amplifier and a tank circuit, as shown in Figure 3-2. The generator frequency and variable capacitor in the tank circuit can be adjusted for maximum signal as observed by a small antenna placed near the plates in the RF cavity. The RF voltage on the plates can be varied from 0 - 4000 volts. Approximately 60 cm from the brass plates an aluminum disk containing a 0.15 cm horizontal slit in its center blocks off the beam tube. The passing of the deuteron beam through the electric field causes the beam to be swept across the aluminum disk. Each time the beam passes across the slit in the disk, a deuteron pulse is created. The intensity of these pulses is optimized as follows. With the RF sweeping voltage turned off, one can observe, through a window in the beam tube, the beam striking a vicor glass disk that swings in front of the slit. While observing the beam, voltages on the plates of the quadrupole focusing lenses can be adjusted to define the beam to a very narrow horizontal line. Then, when the RF is turned on, the result downstream from the

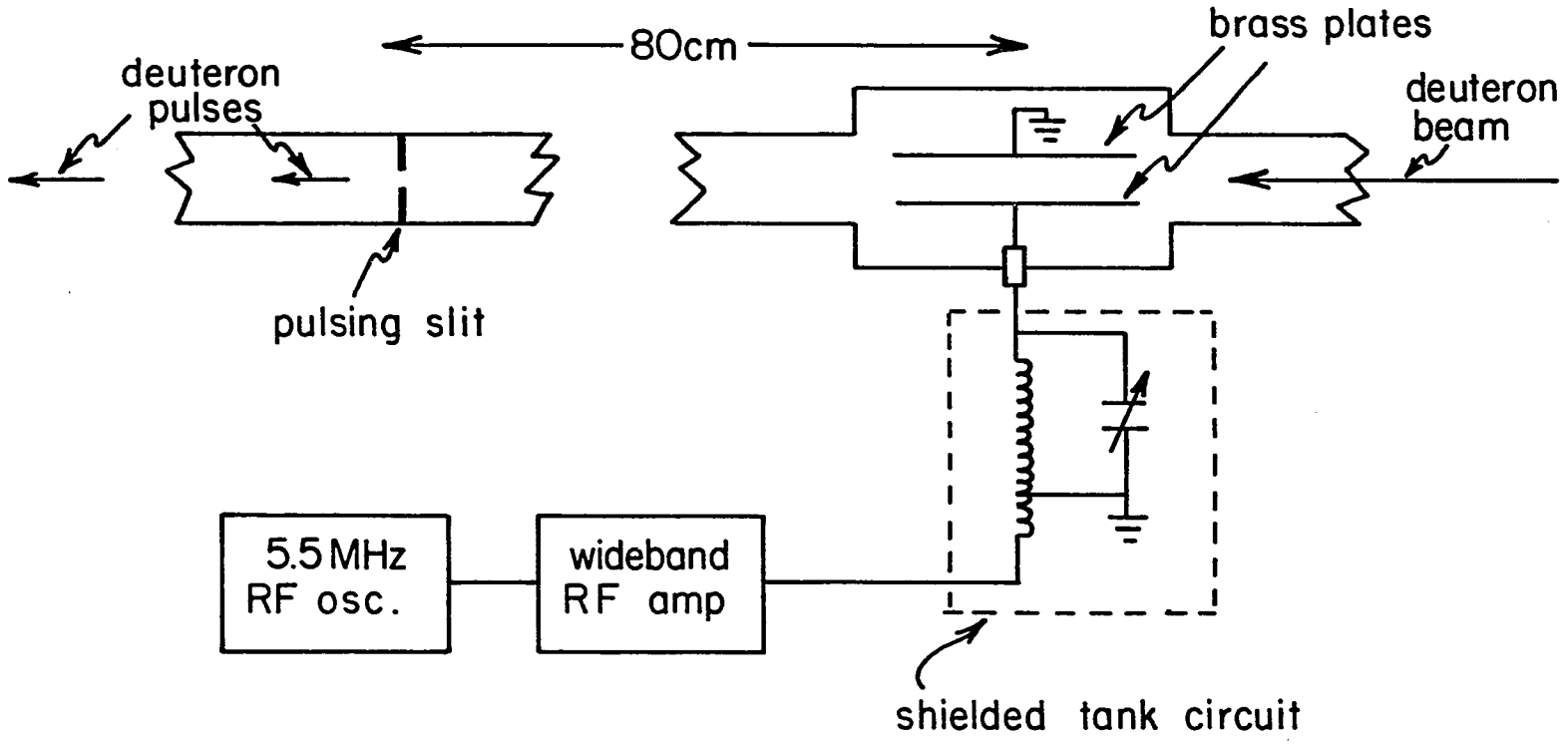
80cm
brass plates
deuteron pulses
deuteron beam
pulsing slit
5.5 MHz RF osc.
wideband RF amp
shielded tank circuit

FIGURE 3-2

slit is a pulsed deuteron beam with a pulse separation of approximately 100 ns and a duration of approximately 2 - 8 ns. The effective beam current at this point is only about 5% of that before pulsing, that is 1.0 - 1.5 microamps.

A problem in the pulsing system was indicated by spurious peaks in initial TOF spectra, implying the presence of neutron sources in the pulsing system area. To absorb neutrons produced in that area, the section of beam tube from the stabilizer slits to the pulsing slit was enclosed in paraffin blocks. In addition, a concrete block wall was built to isolate the target area, discussed in Section 3-4, from the pulsing system. The effect of this shielding was dramatic in that subsequent TOF spectra were free of unexpected peaks.

3-4 The Target Area

When studying the (n,n'gamma) reaction in small samples and observing weak lines it is desirable to reduce background as much as possible. Particularly when using ^{56}Fe as a sample nucleus it is important to eliminate ^{56}Fe in the target area. For this reason a special water cooled Delrin target holder was designed and fabricated. Delrin is a compound similar to nylon and is composed largely of carbon and hydrogen. Since 3 MeV neutrons were to be used in this work, and the first excited states of carbon and oxygen are at 4.43 MeV and 6.13 MeV respectively, very little contribution was expected from the target holder. In

designing the target holder an effort was made to keep the water cooling chamber behind the target as small as possible and thus have the neutron source close to the end face of the holder and the sample which would later be positioned there. The neutron producing target itself is a layer of deuterated titanium 1.86 mg/cm^2 thick on a copper backing so that, except for the target and a charge collection lead for current monitoring, there is very little material in the target region to produce background gamma lines. To further insure low background the target assembly is mounted on a 60 cm long transparent acrylic plastic tube. Supports for the beam tube-target assembly and the sample are also constructed from acrylic plastic. Later the transparent nature of the tube allowed carbon buildup on the target to be observed. Between data sets thin carbon buildup was removed using fine emery cloth and steel wool.

Samples to be studied were placed in cylindrical plastic vials and supported at the endface of the Delrin target holder. Variations in sample size will be taken into consideration in Chapter IV. Angles and distances were marked on the floor beneath the target and were referenced from the center of the target holder endface to the front face of the Ge(Li) detector which was placed 30 cm from the target. An alignment jig was used to insure proper placement after removal of the Ge(Li) for weekly liquid nitrogen refilling. A range of angles from 0° to 90° and flight path lengths from 20 cm to 100 cm were available.

As a monitor of neutron flux with which to normalize data runs, an NE213 liquid scintillator cell viewed by an RCA 8575 photomultiplier tube was placed at 90° to the beam and 80 cm from the target. This monitor was stationary during data runs.

5 Electronics

Both the Ge(Li) detector and neutron monitor are operated in a time-of-flight (TOF) gated mode. In the case of the Ge(Li) detector this means that energy analysis only takes place during a short interval of time, ~ 12 ns, at a time after neutrons are produced in the target such that only prompt gamma radiation is observed. Neutrons produced in the target or scattered elastically from the sample, being slower than photons, arrive at the Ge(Li) detector too late to fall into the analysis window. To show this consider the expression for neutron flight times:

$$t = 0.723\ d/(E)^{1/2}$$

Where t is the transit time in ns, d is distance traveled in cm and E is the neutron energy in MeV. Thus for a 3 MeV neutron we find a flight time of ~ 14 ns for a flight path of 34.5 cm (average distance from target to the center of the Ge(Li) crystal). In comparison a photon travels the same distance in ~ 1 ns for a difference of ~ 13 ns. This allows a 12 ns wide analysis window to be centered about the gamma TOF peak and exclude neutron effects in the Ge(Li)

detector. In addition, since energy analysis only takes place for 12 ns out of every 100 ns, we exclude 88% of uncorrelated background gamma radiation present in the room and created in the sample-target area. The neutron monitor is also operated in the TOF mode so that counts under the neutron peak appearing in the time of flight spectrum can be used to normalize data runs.

Figure 3-3 shows the full electronics setup used. The Ge(Li) detector preamp output is split. Part of this signal is amplified and shaped using a timing filter amplifier (TFA) and a fast timing pulse is derived from it using a constant fraction discriminator (CFD). This provided the start pulse to the Ge(Li) TOF time-to-amplitude converter (TAC). A small antenna placed near the RF plates in the plate cavity picks up the 5.5 MHz signal and a fast discriminator produces a timing pulse each time the signal goes negative below a reference voltage set by the discriminator control. This serves as the stop pulse for both time-to-amplitude converters. Using the Ge(Li) signal to start the TAC causes the time spectrum to be reversed with time increasing to the left but provides the lowest dead time for the TAC. Similarly a fast timing pulse is produced from the neutron monitor signal using another fast discriminator. This is used to start the monitor TAC. The system described so far comprises the fast electronics and is placed close to the Ge(Li) while the rest of the analysis takes place in the control room.

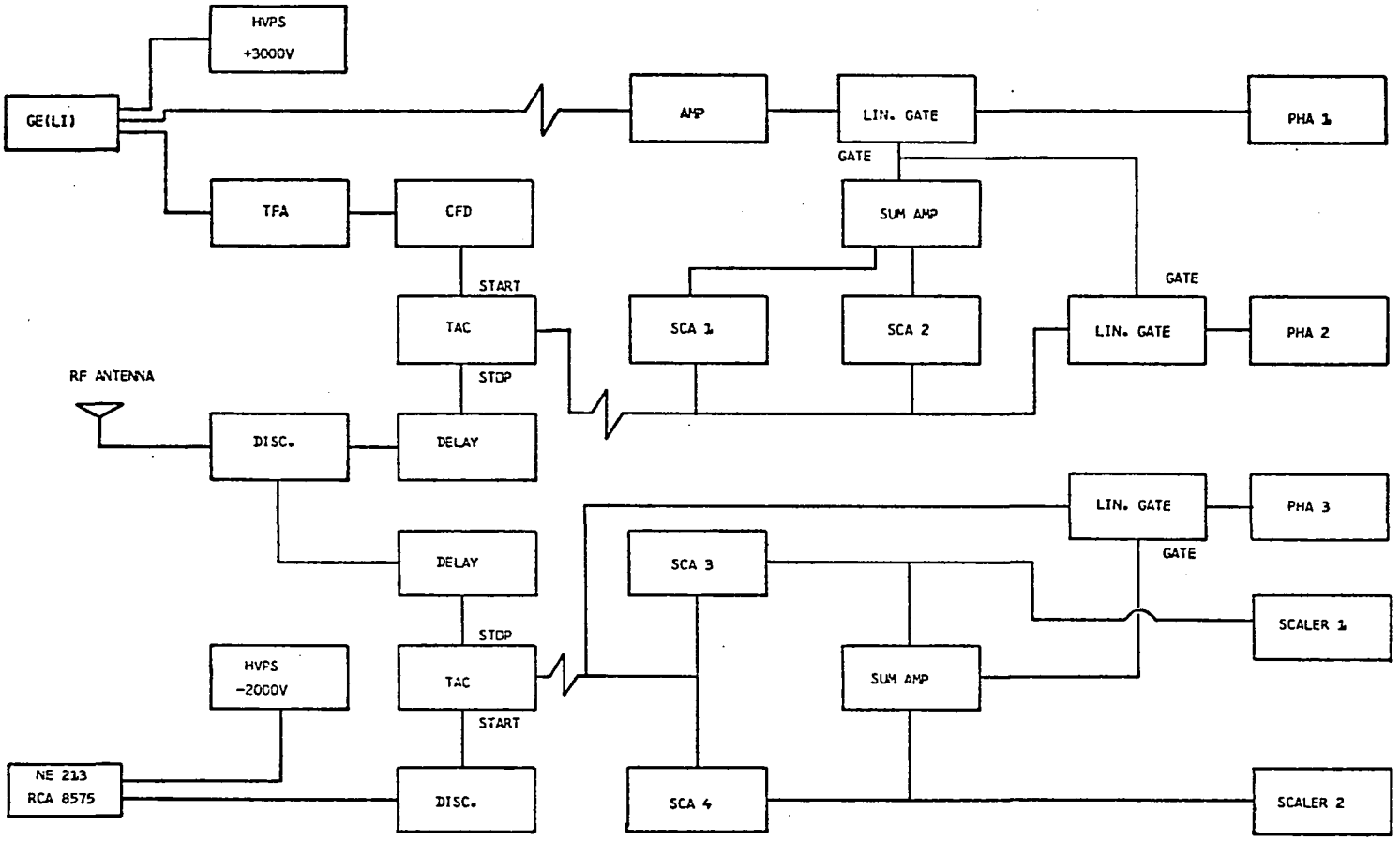
HVPS
+3000V
GE(LI)
AMP
LIN. GATE
PHA 1
GATE
TFA
CFD
SUM AMP
START
GATE
TAC
SCA 1
SCA 2
LIN. GATE
PHA 2
STOP
RF ANTENNA
DISC.
DELAY
LIN. GATE
PHA 3
DELAY
SCA 3
GATE
STOP
SCALER 1
HVPS
-2000V
TAC
SUM AMP
START
NE 213
RCA 8575
DISC.
SCA 4
SCALER 2

FIGURE 3-3

Upstairs the other half of the Ge(Li) preamp signal is amplified and gated on the gamma peaks in the TOF spectrum by two single channel analyzers (SCA 1 and SCA 2) and a summing amplifier. This gated signal is analyzed by a pulse height analyzer (PHA 1). The settings of the two analysis windows can be observed in the Ge(Li) TOF analyzer (PHA 2). Two single channel analyzers are used since a double set of neutron and gamma peaks is produced by the fast electronics. The reason for this is that a deuteron pulse occurrs each time the RF sweep voltage passes through zero, that is, twice each cycle, while a stop pulse is created only by the negative leading edge of the RF signal, that is, once each cycle. The relative timing of the various TOF system pulses is shown more clearly in Figure 3-4. First a plot of the RF sweeping voltage versus time shows the voltage passing through zero at intervals 90 ns apart corresponding to 5.5 MHz sweeping voltage. The second line in Figure 3-4 shows the deuteron pulse at the slits 80 cm downstream from the RF plates. Each pulse has occurred 150 ns after the RF went through zero since 300 keV deuterons require that long to travel 80 cm. Another 70 cm downstream the deuteron pulses arrive at the TiD target and produce neutrons and gammas in the target and sample. This requires another 130 ns travel time for the deuterons. The fourth line in Figure 3-4 shows gammas arriving at the Ge(Li) detector after 1 ns travel time (peaks in solid lines) and neutrons after 14 ns (peaks in dotted lines). In

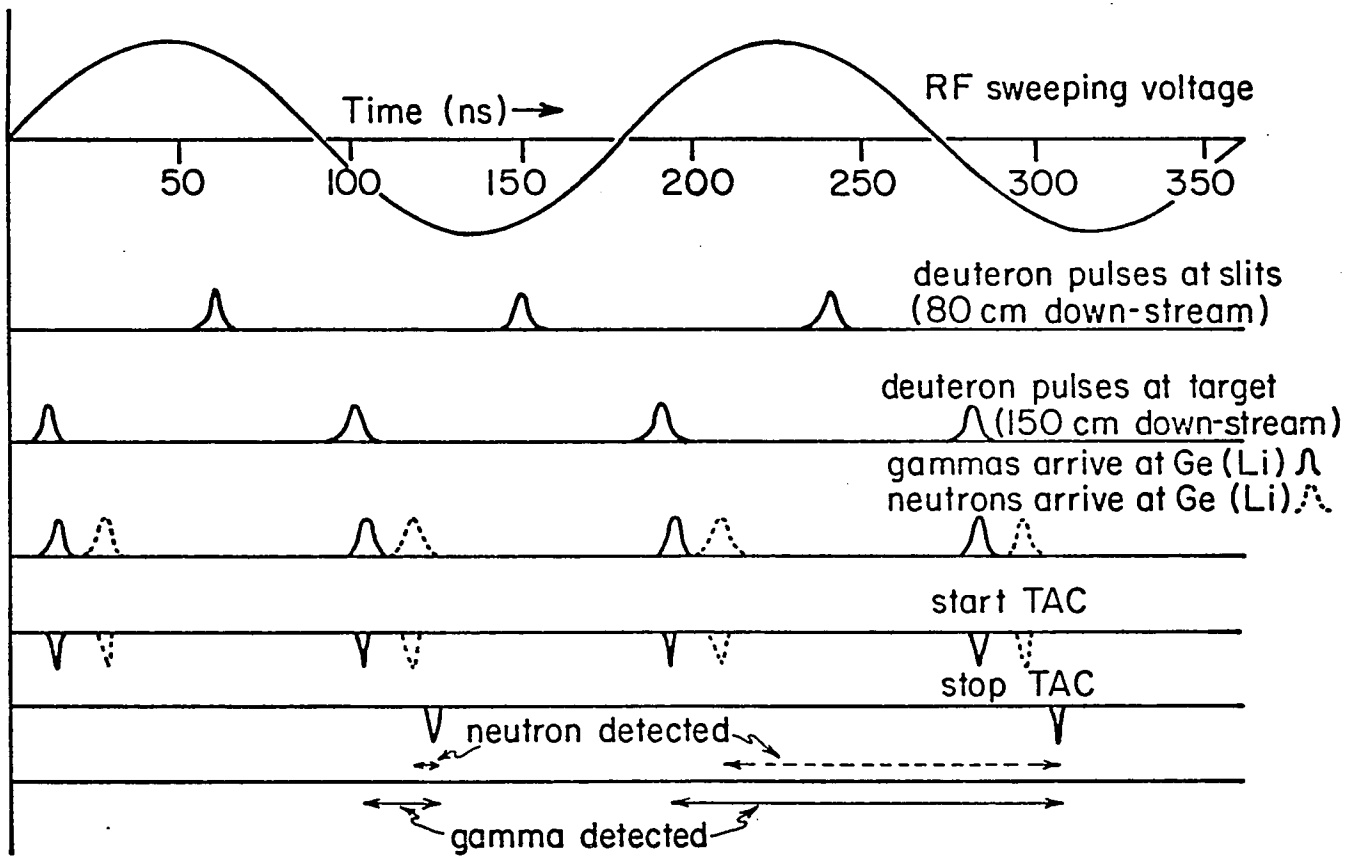
RF sweeping voltage
Time (ns)→
50
100
150
200
250
300
350
deuteron pulses at slits
(80 cm down-stream)
deuteron pulses at target
(150 cm down-stream)
gammas arrive at Ge (Li)
neutrons arrive at Ge (Li)
start TAC
stop TAC
neutron detected
gamma detected

FIGURE 3-4

the fifth and sixth lines are the respective start pulses and the stop pulse derived from a reference point on the negative part of the RF waveform. Finally, in the last line the origin of the two sets of peaks in the TOF spectrum becomes evident. In the first case the start pulses have occurred just before the stop pulse and result in short time intervals, ie., small pulse heights and a set of peaks at the left of the TOF spectrum. In the other example the start pulses occur just after a stop pulse, and so the time interval is long, resulting in a large pulse height and a set of peaks on the right of the TOF spectrum. It is clear then that the use of only one of these sets of peaks would mean a loss of half of the available data.

The neutron monitor TOF spectrum is treated similarly. SCA 3 is set to include the neutron peak and SCA 4 is set to include a flat portion of the neutron monitor time spectrum. The area under the flat portion is then subtracted from the neutron peak area to arrive at a normalization. Again the SCA settings are monitered on the neutron monitor analyzer (PHA 3). Scalers 1 and 2 integrate the areas of the time spectrum selected by SCA 3 and SCA 4.

Figure 3-5 shows a typical Ge(Li) TOF spectrum taken at 90° and with a 30 cm flight path. As explained previously there are two sets of neutron and gamma peaks. Because of the time reversal created by use of the Ge(Li) detector signal as a start pulse the smaller gamma peaks occur to the right of the larger neutron peaks. Each set of

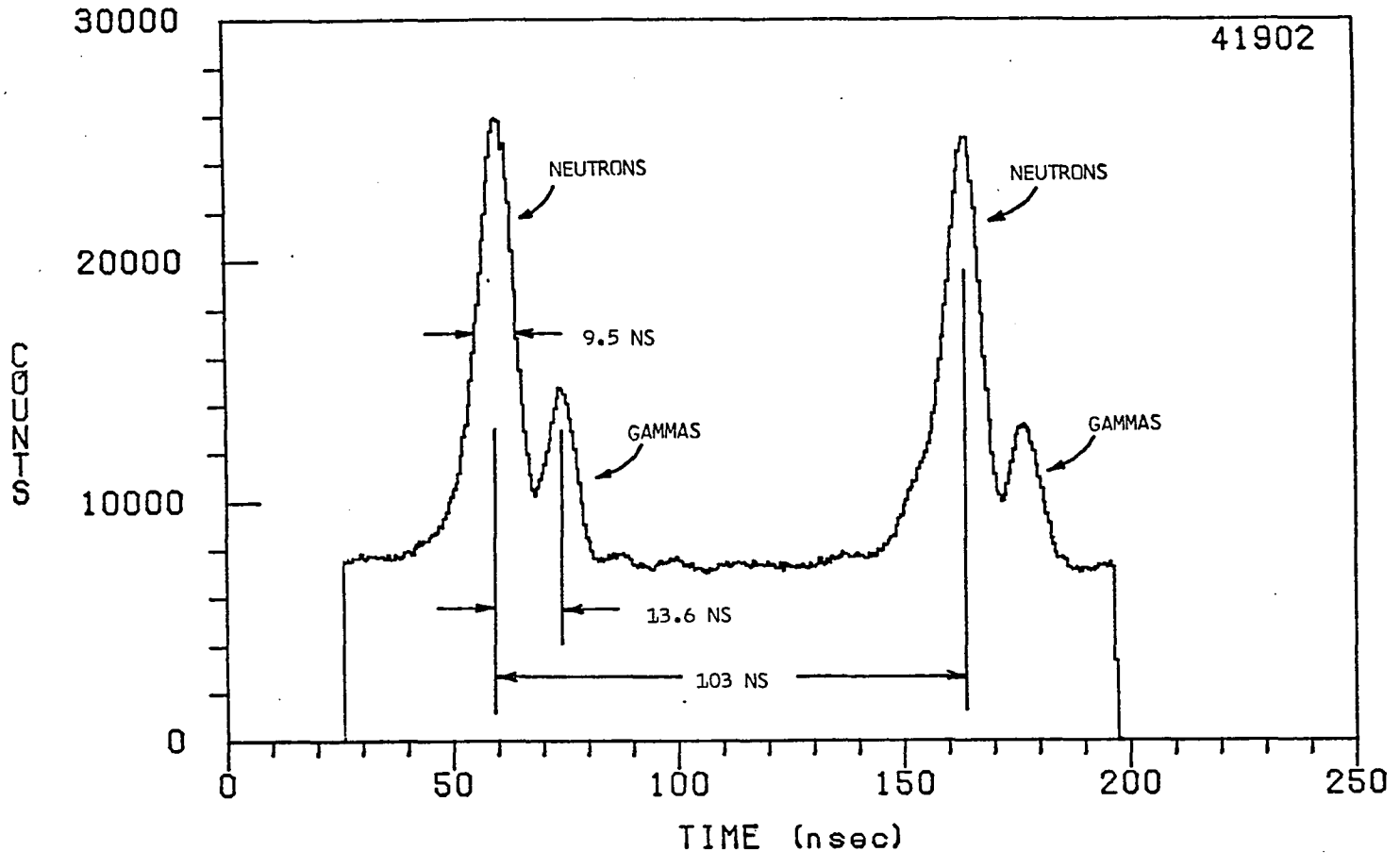
Ge(Li) TOF SPECTRUM AT 90 DEGREES - Sb SAMPLE
41902
NEUTRONS
NEUTRONS
9.5 NS
GAMMAS
GAMMAS
13.6 NS
103 NS
COUNTS
30000
20000
10000
0
0
50
100
150
200
250
TIME (nsec)

FIGURE 3-5

peaks is separated by ~ 13.6 ns as expected. The FWHM of the neutron peak is 9.5 ns. This spectrum indicates that it should be possible to eliminate much of the effect of prompt neutrons and observe prompt gamma radiation by setting the analysis window as indicated in Figure 3-5. In practice an 11.7 ns wide window is set at each gamma peak.

As a check to insure that the peaks in the time spectrum peaks are properly identified, a series of time spectra were accumulated at different flight path lengths. The velocity of the neutrons was calculated from the slope of peak position versus flight path length. The result of that test was an experimental velocity of 2.1 ± 0.2 cm/ns versus 2.2 cm/ns calculated for 2.5 MeV neutrons emitted at 90° from a thick TiD target. It was also observed that the gamma peak largely disappeared when no scattering sample was present while the neutron peak remained virtually unchanged.

3-6 Calibration

Calibration of the energy analysis PHA is required in order to determine gamma line energies and relative efficiencies for use in gamma emission cross section measurements. Energy and relative efficiency calibrations were both performed using a set of Amersham calibrated gamma reference sources at the following energies

Source	Energy (MeV)
^{137}Cs	0.662
^{54}Mn	0.835
^{88}Y	0.898
^{60}Co	1.172
^{22}Na	1.277
^{60}Co	1.333
^{88}Y	1.836

A plot of the calibration points and the linear fit for a typical energy calibration run is shown in Figure 3-6. The error in determining the peak channel is estimated at ± 0.25 channels. The confidence level of the fit shown in Figure 3-6 is 24% indicating that the fit is reasonable. Using the slope and intercept for this fitted line, the calculated energies of the sources are compared to the known energies. The average error found in this comparison is ± 0.0020 MeV and the standard deviation about the mean is 0.0027 MeV. This indicates that gamma line energies can be determined to within ± 0.003 MeV, which is comparable to the resolution obtainable with the Ge(Li) detector used in this experiment.

The relative efficiency calibration is run with the Ge(Li) TOF gating on because the use of discriminators in the fast timing system reduces efficiency considerably at energies below 0.8 MeV as shown in Figure 3-7. Relative efficiencies at energies between 0.835 MeV and 1.836 MeV are

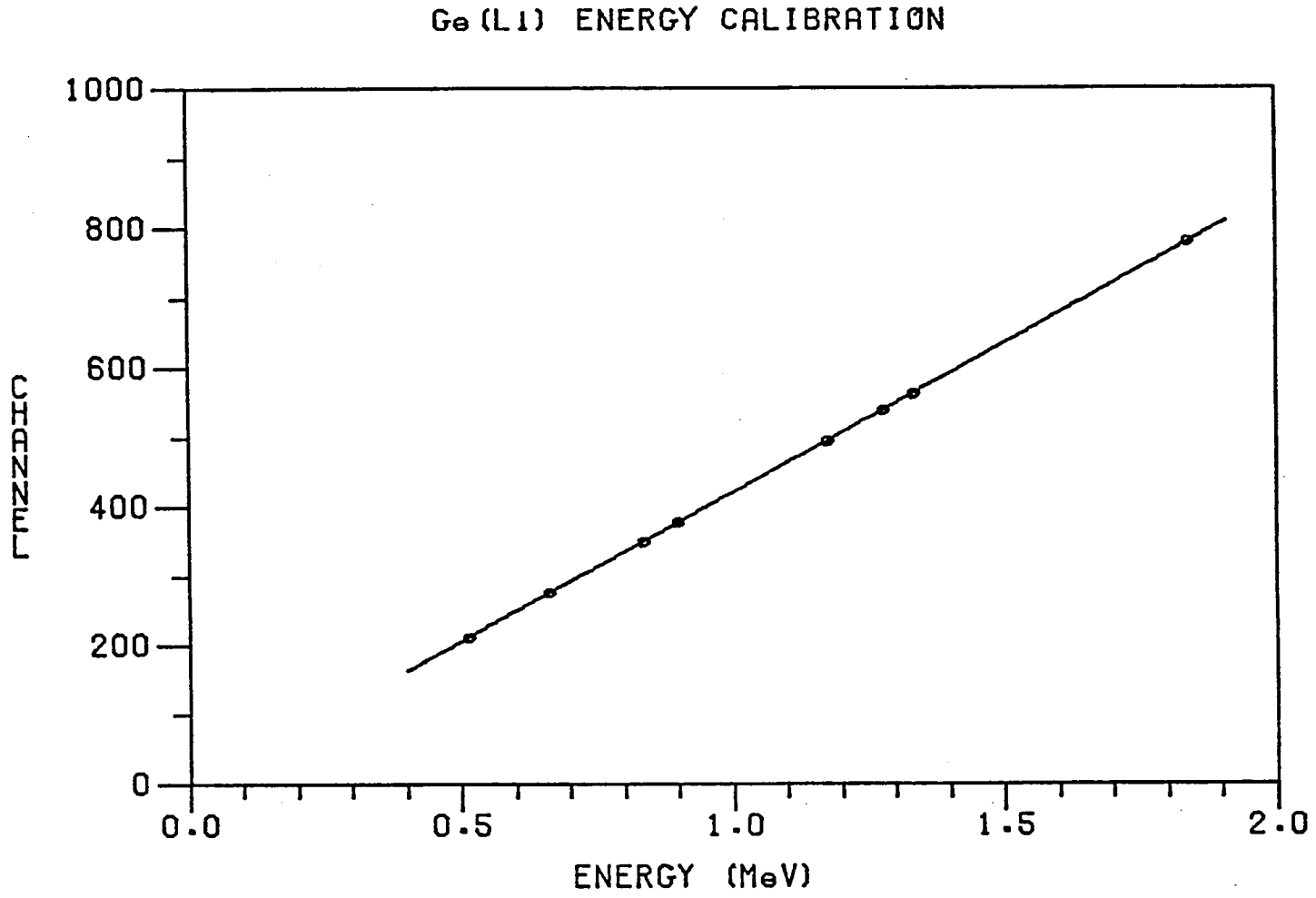
Ge(Li) ENERGY CALIBRATION
1000
800
600
400
200
0
CHANNEL
0.0
0.5
1.0
1.5
2.0
ENERGY (MeV)

FIGURE 3-6

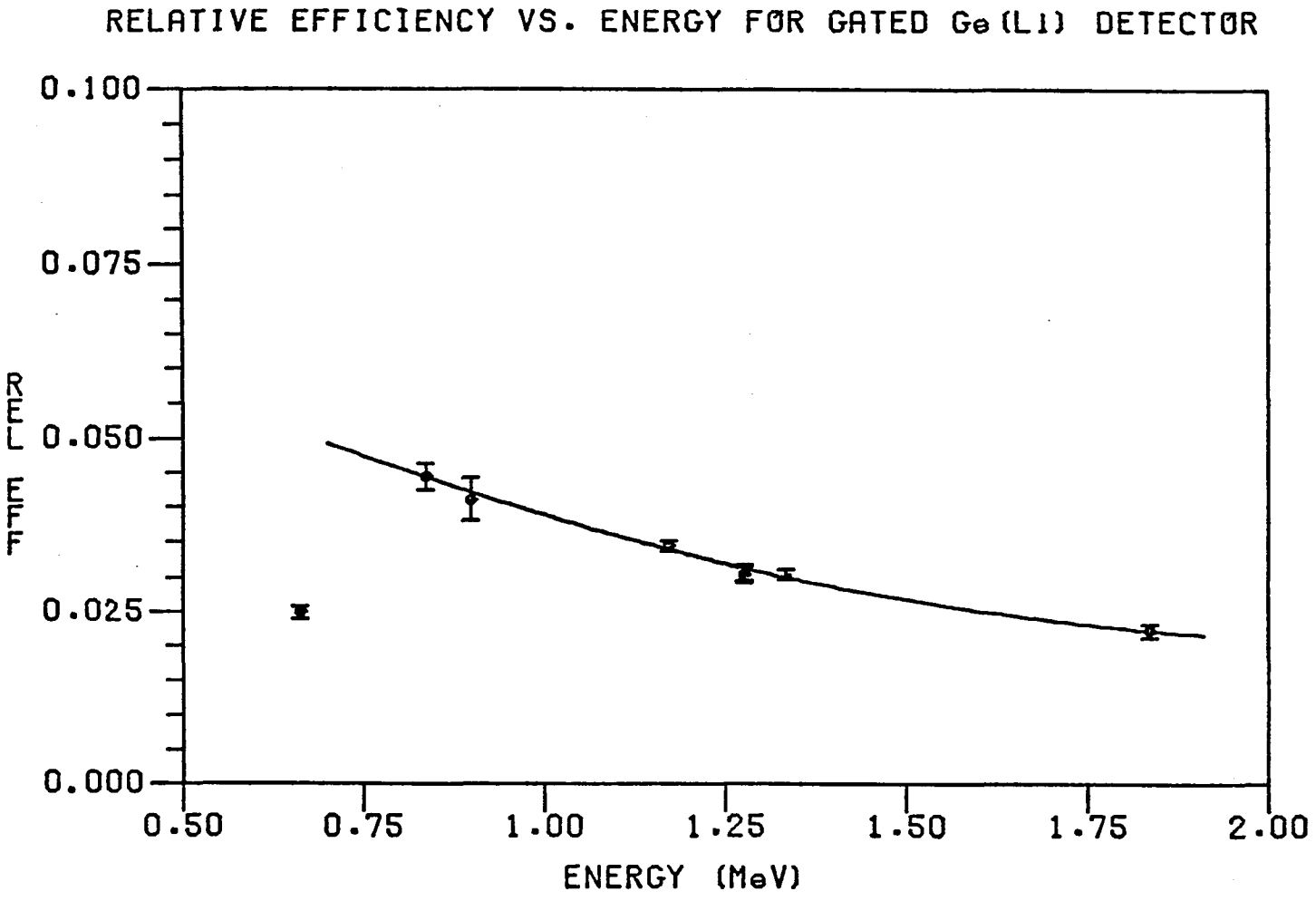
RELATIVE EFFICIENCY VS. ENERGY FOR GATED Ge(Li) DETECTOR
0.100
0.075
0.050
0.025
0.000
REL EFF
0.50
0.75
1.00
1.25
1.50
1.75
2.00
ENERGY (MeV)

FIGURE 3-7

obtained by first or second order polynomial fits to the calibration points between 0.835 MeV and 1.836 MeV. With this calibration information it is possible to use the strong 0.847 MeV line in ^{56}Fe as a standard to determine gamma emission cross section at different energies in various samples.

A time calibration of the Ge(Li) time-of-flight time-to-amplitude converter is also performed in order to measure time intervals as shown in Figure 3-5. This calibration is done by simply delaying a stop pulse to the Ge(Li) TOF TAC using known lengths of delay cable. An Ortec Model 425 nanosecond delay unit is used with a quoted error of ± 100 ps for each switched in delay cable. A plot of the calibration points obtained in this manner and a linear fit to the points is presented in Figure 3-8.

3-7 Data Acquisition

Data sets are obtained in runs normalized to the neutrons counted under the neutron monitor TOF spectrum. For iron samples these runs lasted approximately two hours while for antimony runs lasted from three hours to as much as eight hours at each angle. In general data was taken at seven angles from 90° to 0° spaced 15° apart. Runs were also made at all angles with the sample replaced by an empty plastic vial to insure that there was no contribution from background near gamma transitions of interest. In the case of ^{56}Fe this was believed important since some 0.847 MeV

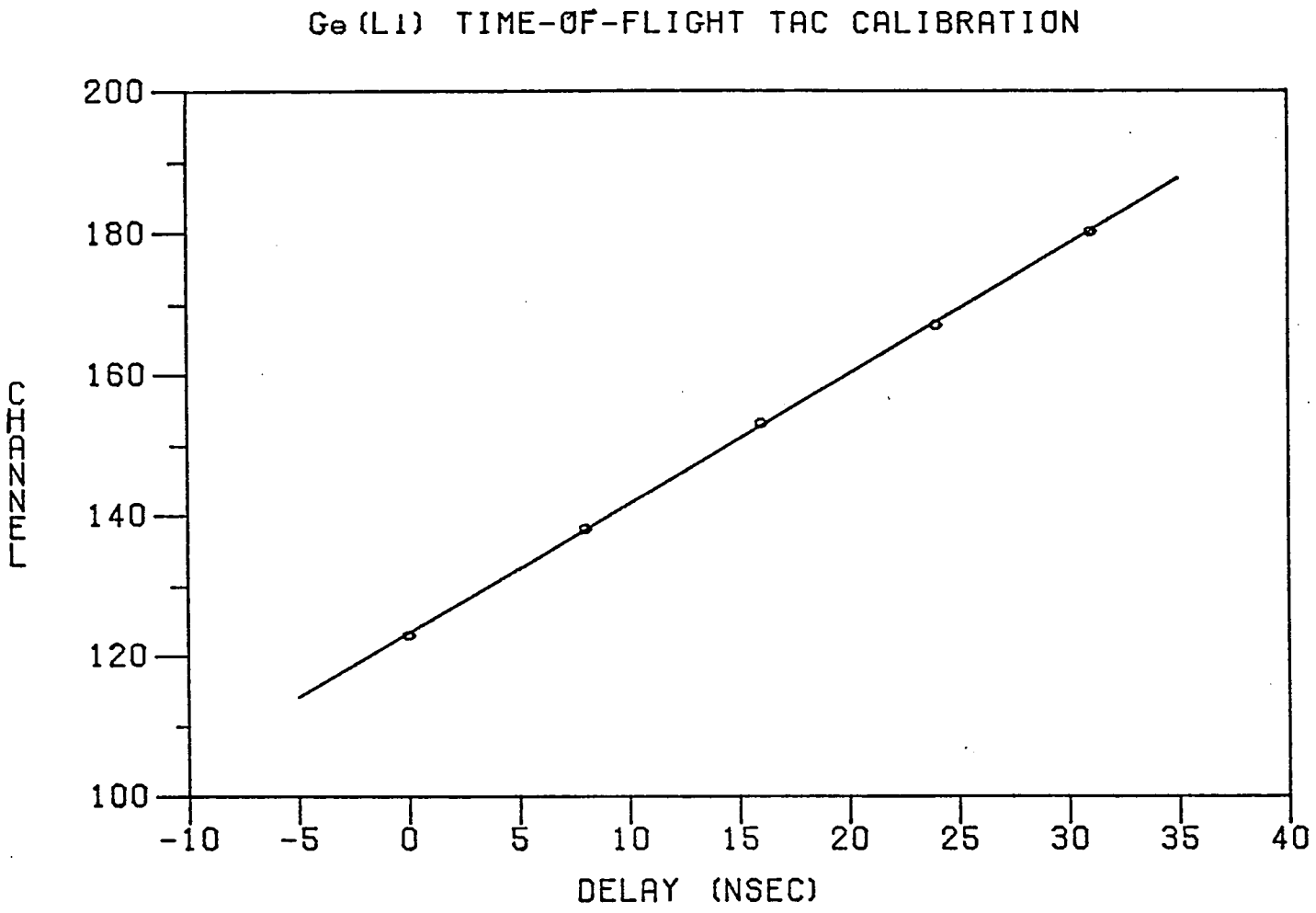
Ge(Li) TIME-OF-FLIGHT TAC CALIBRATION
CHANNEL
200
180
160
140
120
100
-10
-5
0
5
10
15
20
25
30
35
40
DELAY (NSEC)

FIGURE 3-8

radiation was seen in the background runs, presumably due to inelastic scattering from the large amounts of steel present in the Ge(Li) detector dewar and equipment rack supporting it. In practice, however, the 0.847 line due to the ^{56}Fe(n,n'gamma)^{56}Fe reaction in the sample was so strong that the background contribution was negligible.

The energy spectrum was accumulated using a 1000 channel analyzer offset 256 channels to give maximum coverage to the energy region of interest. Data from all of the analyzers is then transmitted to the University's DECsystem10 computer via high speed line for analysis.

IV. DATA ANALYSIS AND RESULTS

4-1 Introduction

The ultimate goal of this research is to determine level spins and gamma emission cross sections for excited states of ^{121}Sb and ^{123}Sb produced by the (n,n'gamma) reaction. This chapter will present the analysis of data obtained with iron and antimony samples in an effort to achieve that goal. In order to confirm the validity of the techniques employed, we first apply those techniques to ^{56}Fe and compare the results with those obtained by other experimenters. Then we discuss the results obtained with antimony.

The first section of this chapter will discuss the method of data analysis. In essence, the theoretical angular distributions calculated in Chapter II are compared to the experimental data obtained as discussed in Chapter III. Then Sections 4-3 and 4-4 present the results obtained with ^{56}Fe and the two stable antimony isotopes respectively.

4-2 Data Analysis Techniques

First we consider the analysis of angular distributions in order to determine level spins and mixing ratios. Then we discuss the extraction of gamma emission cross sections measured relative to the 0.847 MeV level of ^{56}Fe.

The basic approach in the analysis is to generate theoretical angular distributions for various hypothetical excited state spins. These distributions are then distorted in order to include such experimental factors as geometry, finite sample and source size etc. The altered distributions are then compared to raw experimental data, while varying the mixing ratio if it is non-zero, to determine a best fit. This allows us to quote values of spins and mixing ratios within certain confidence limits. This is the approach developed by a research group at the Nuclear Research Centre, Alberta, Canada. The analysis program, EVA, utilized by that group was made available to this laboratory and rewritten to suit the experimental conditions at hand (Davidson, 1976). The entire program and all subroutines were also thoroughly checked out to insure reliability.

Because of the close geometry employed in this experiment, geometrical factors become quite important. EVA is essentially a numerical integration program that determines the result expected in the laboratory from information about the angular distribution under idealized

conditions, ie., a point sample in a parallel neutron beam. The following factors are considered by EVA (see Appendix E)

- energy loss of the 300 keV deuteron in the TiD target affecting neutron energy through kinematics of the $d(d,n)^3He$ reaction
- neutron source angular distribution anisotropy including energy and yield anisotropies
- finite size of Ge(Li) detector
- finite area of the neutron source spot
- finite volume of the sample including the $1/r^2$ dependency of neutron flux
- error in the flight path length and angle to the Ge(Li) detector caused by reference of these quantities to the end face of the TiD target
- gamma and neutron attenuation in the sample

Theoretical angular distributions are entered into EVA in the form of the B_ν coefficients. The general form of the angular distribution is

$$W(\theta_i) = \sum_\nu a_\nu P_\nu(\cos \theta_i)$$

where the a_ν, calculated by MANDYF, depend on properties of the nuclear level being studied as well as the incident neutron energy E_n. The a_ν can also be expressed as

$$a_\nu = B_\nu \, c_\nu(J_i, J_f, \delta)$$

where the mixing ratio dependence is contained in c_ν, which

depends only on J_i and J_f (Green et al., 1972). Thus, with the B_γ supplied by MANDYF, EVA can vary δ and compare the resulting distorted theoretical distributions to experimental data for a best fit. Other information required by EVA includes neutron and gamma attenuation coefficients, beam spot and sample sizes, the angular attenuation factors Q_γ, as well as the experimental gamma yields at various angles.

Briefly, EVA begins the integrations by dividing the energy thickness of the TiD target into energy increments, the beam spot area in the TiD target into area increments and the sample volume into volume increments. Then for each increment the following routine is carried out. First the neutron energy is determined from $d(d,n)^3He$ reaction kinematics. Then the neutron path angle and length from the current beam spot area increment to the current volume increment are calculated. The neutron path angle allows a correction to be made for the angular distribution of neutrons from the $d(d,n)^3He$ and the length allows a $1/r^2$ correction to the neutron flux at the current volume increment to be made. Also the neutron path length inside the sample allows us to include neutron attenuation in the sample. Then the gamma path from the current volume increment to the Ge(Li) is calculated. Corrections are made for gamma attenuation in the sample, path length and angle errors, and the finite size of the Ge(Li) detector. The angle between the incident neutron and emitted gamma is then

computed and the theoretical yield calculated using the appropriate B_γ. This series of calculations is carried out over all combinations of energy, area, and volume increments with each contribution summed to obtain a theoretical yield at one experimental angle. This is repeated at all angles for which experimental yields were obtained. EVA concludes its analysis by performing a least squares fit to the experimental yields, varying the magnitude of the theoretical yield and the mixing ratio if desired. Finally the reduced χ^2 and confidence level of the best fit for each δ is output. From output files created by EVA, plots are produced using a general plotting routine, DIST, written in this laboratory (Patnode, 1978). Two types of plots are produced. First the distorted angular distributions are plotted along with the raw experimental data. This allows direct comparisons to be made between distributions calculated for hypothetical spins and experimental yields. The second type of graphic output is a plot of the reduced χ^2 versus arctan(δ) for each hypothetical spin. Confidence levels for the appropriate degrees of freedom are graphed also to indicate the reliability of the fit. From this type of graphic output we can make a statement about the probable values of the excited state spins and mixing ratio involved in a nuclear gamma transition.

The analysis program EVA is also useful in extracting differential gamma emission cross sections from experimental yields at 90°. By running EVA on a data point

at 90^0 we obtain an attenuation coefficient that corrects for geometry and attenuation of gammas and neutrons in the sample. The differential cross section is then given by

$$d\sigma/d\Omega = C\ Y\ A\ /\ (\epsilon_\gamma\ g\ n\ M\ f)$$

where

C = a constant

Y = gamma yield at gamma energy of interest, E_γ

A = atomic weight of sample

ϵ_γ = relative gamma detection efficiency at E_γ

g = geometric correction factor from EVA

n = Avogadro's number

M = sample mass

f = isotopic abundance

To determine the constant C, the differential gamma emission cross section of ^{56}Fe is used as a standard and the above equation for $d\sigma/d\Omega$ is solved for C. From a recent compilation of the differential gamma emission cross sections at 90^0 for ^{56}Fe in the 3 MeV region, an average value of 73.1 ± 5.9 mb/sr was obtained (McEllistrem, 1977). The value of $\epsilon(E_\gamma)$ is determined as described in Chapter III and g is calculated for the particular ^{56}Fe sample used. Then the yield obtained for ^{56}Fe is used to solve for C (see Section 4-3). With this value of C, we can determine any differential gamma emission cross section relative to the 0.847 MeV ^{56}Fe level.

4-3 ^{56}Fe Analysis

The primary purpose of this section is to confirm that the experimental technique is valid. ^{56}Fe is a good choice for this purpose because of its high cross section for the (n,n'gamma) reaction, its availability, and its 91.66% isotropic abundance. The spin of the 0.847 MeV level is known from other experiments to be +2, which is a result that we hope to duplicate here. Also, the differential gamma emission cross sections for the 1.24 MeV and 1.81 MeV transitions are known from other experiments and are compared with the results obtained here (see Figure 2-4 for an energy level diagram of ^{56}Fe).

First we present a typical time-of-flight gated Ge(Li) energy spectrum in Figure 4-1. This spectrum was taken at an angle of 90° with a flight path length of 30 cm during a 1.5 hour run. The three principle gamma transitions observed from ^{56}Fe are shown in the figure. Figure 4-2 is a background run taken under identical conditions but with the powdered iron sample replaced by an empty plastic sample holder. The runs in both figures are normalized to the same number of incident neutrons, as described in Chapter III. Note the absence of peaks in the 1.24 and 1.81 MeV regions of the background spectrum and the relatively small peak near 0.847 MeV in the background spectrum. This allows us to obtain reliable yield data at those energies without necessitating background spectrum subtraction.

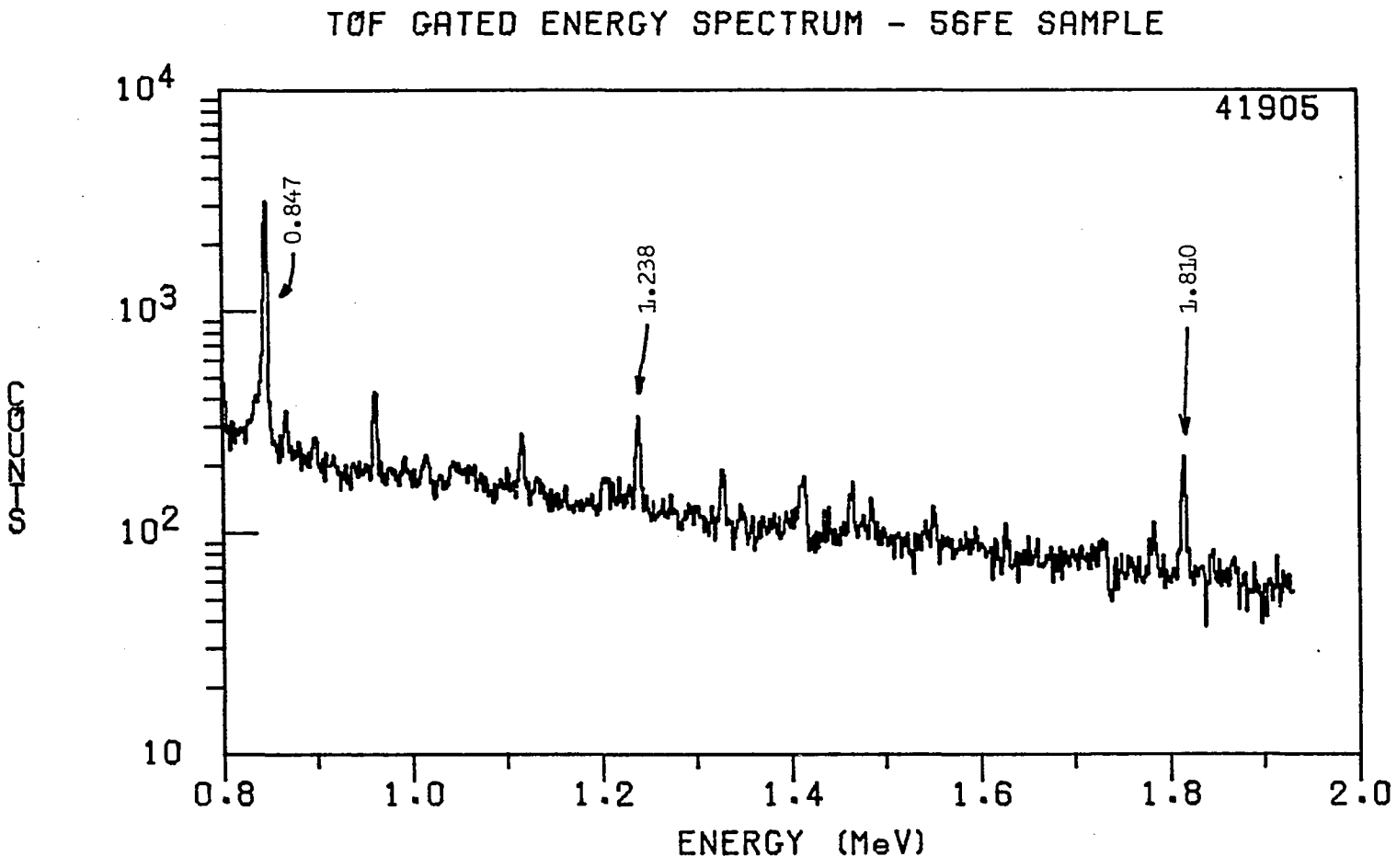
TOF GATED ENERGY SPECTRUM - 56FE SAMPLE
41905
0.847
1.238
1.810
10^4
10^3
10^2
10
0.8
1.0
1.2
1.4
1.6
1.8
2.0
ENERGY (MeV)
COUNTS

FIGURE 4-1

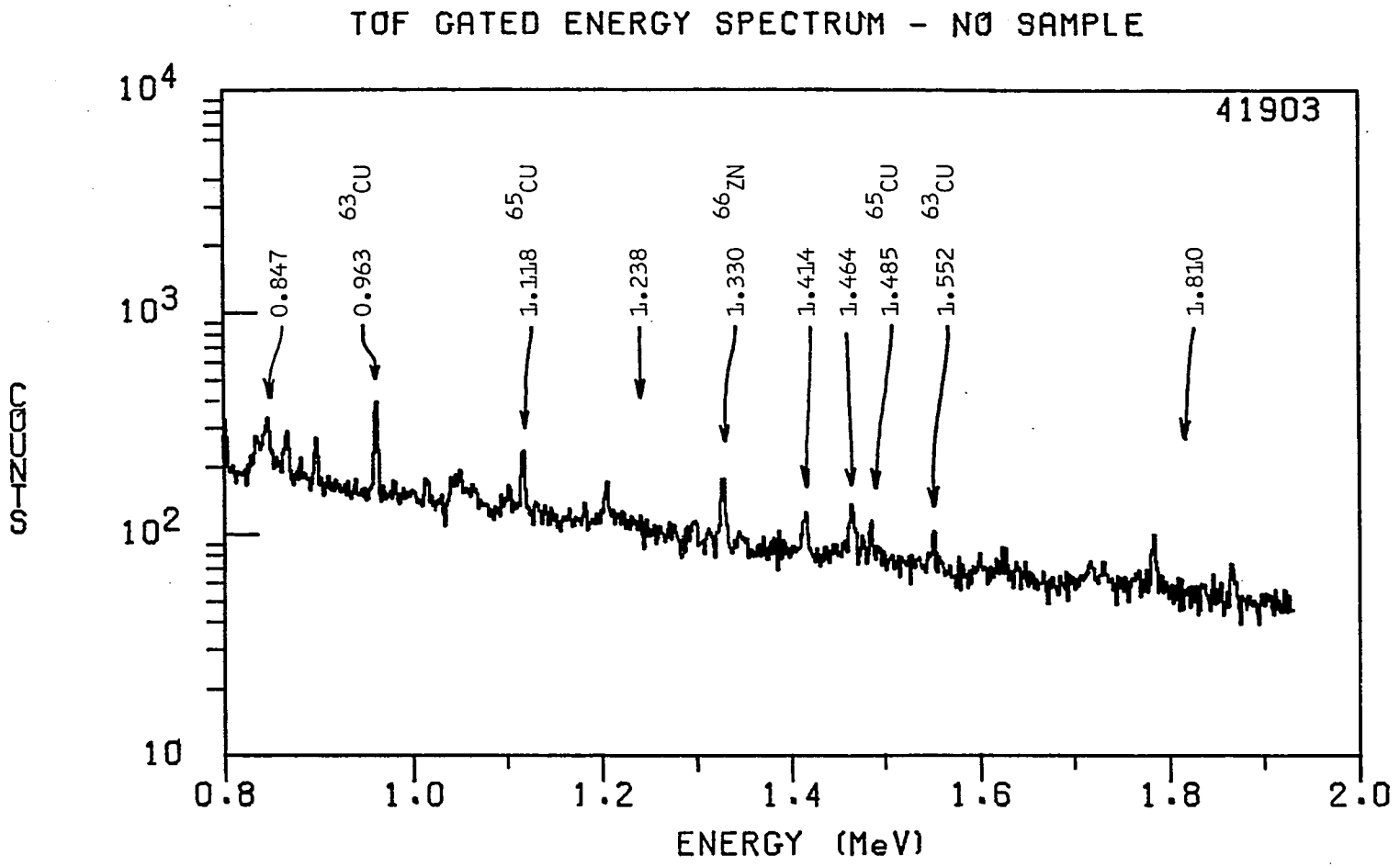
TOF GATED ENERGY SPECTRUM - N0 SAMPLE
41903
10^4
10^3
10^2
10
0.847
0.963
1.118
1.238
1.330
1.414
1.464
1.485
1.552
1.810
^{63}CU
^{65}CU
^{66}ZN
^{65}CU
^{63}CU
0.8
1.0
1.2
1.4
1.6
1.8
2.0
ENERGY (MeV)

FIGURE 4-2

Some background peaks which appeared consistantly in the data are identified in Figure 4-2. Most of the background lines observed apparently result from the (n,n'gamma) reaction in Cu and possibly in Zn and Fe. The Cu lines probably originate from Cu in the target backing. Cu and Zn lines could be produced by the (n,n'gamma) reaction in the brass feed through that allows current from the TiD target to be collected. And of course the ^{56}Fe(n,n'gamma) reaction in the Ge(Li) environment, ie., the steel dewar and equipment rack supporting it, can explain the presence of a relatively small peak at 0.847 MeV in the background spectrum. Also identified in Figure 4-2 is a strong 1.46 MeV background line present in room background at all times and possible resulting from decay of natural ^{40}K.

The first transition of interest in ^{56}Fe is the 0.847 MeV gamma from decay of the 0.847 MeV +2 level. Yields at seven angles from 0° to 90° in 15° steps were obtained from spectra similar to Figure 4-1 by a simple summing of the counts under the peak minus an average background contribution determined on the basis of counts at the left and right sides of the peak. Errors in yields included statistical contributions from background and signal areas summed in quadrature (See Appendix F).

The sample used in obtaining this distribution data was 123 g of natural iron in a cylindrical plastic holder with interior dimensions 3.18 cm in length by 3.80 cm in

diameter. Using the B_ν corresponding to the three hypothetical angular distributions generated by MANDYF for $J_2 = 1, 2, 3$ in Chapter II, we utilize EVA to distort the theoretical distribution and compare it to the experimental yields. The result of this procedure is presented in Figure 4-3. As this figure indicates, the $J_2 = 2$ spin assignment (solid line) gives the best fit to the experimental yield. Therefore, it would appear that the $J_2 = 2$ spin assignment of the 0.847 MeV level is correct. The results of the 0.847 level distribution fits are summarized in Figure 4-4. Because the ground state of ^{56}Fe is a 0 spin state, the mixing ratios of the transitions are all 0, ie., they are transitions of pure multipolarity. Thus the plots of reduced χ^2 versus arctan(δ) are represented by single values drawn as circles. This figure indicates that the $J_2 = 2$ assumption is correct with a fit at a confidence level of 54% whereas the $J_2 = 1$ and 3 assumptions have confidence levels well below 0.1%.

The ^{56}Fe data can also be used to illustrate the effect of making the cascade correction discussed in Chapter II. Figure 4-5 shows the $J_2 = 1, 2, 3$ distributions fit to the data with (solid lines) and without (dashed lines) cascade corrections for the 2.085 MeV and 2.657 MeV levels included. As expected the inclusion of cascade effects is not of major importance, however, the fits are improved somewhat as summarized in Table 4-1.

Next we discuss the measurement of differential

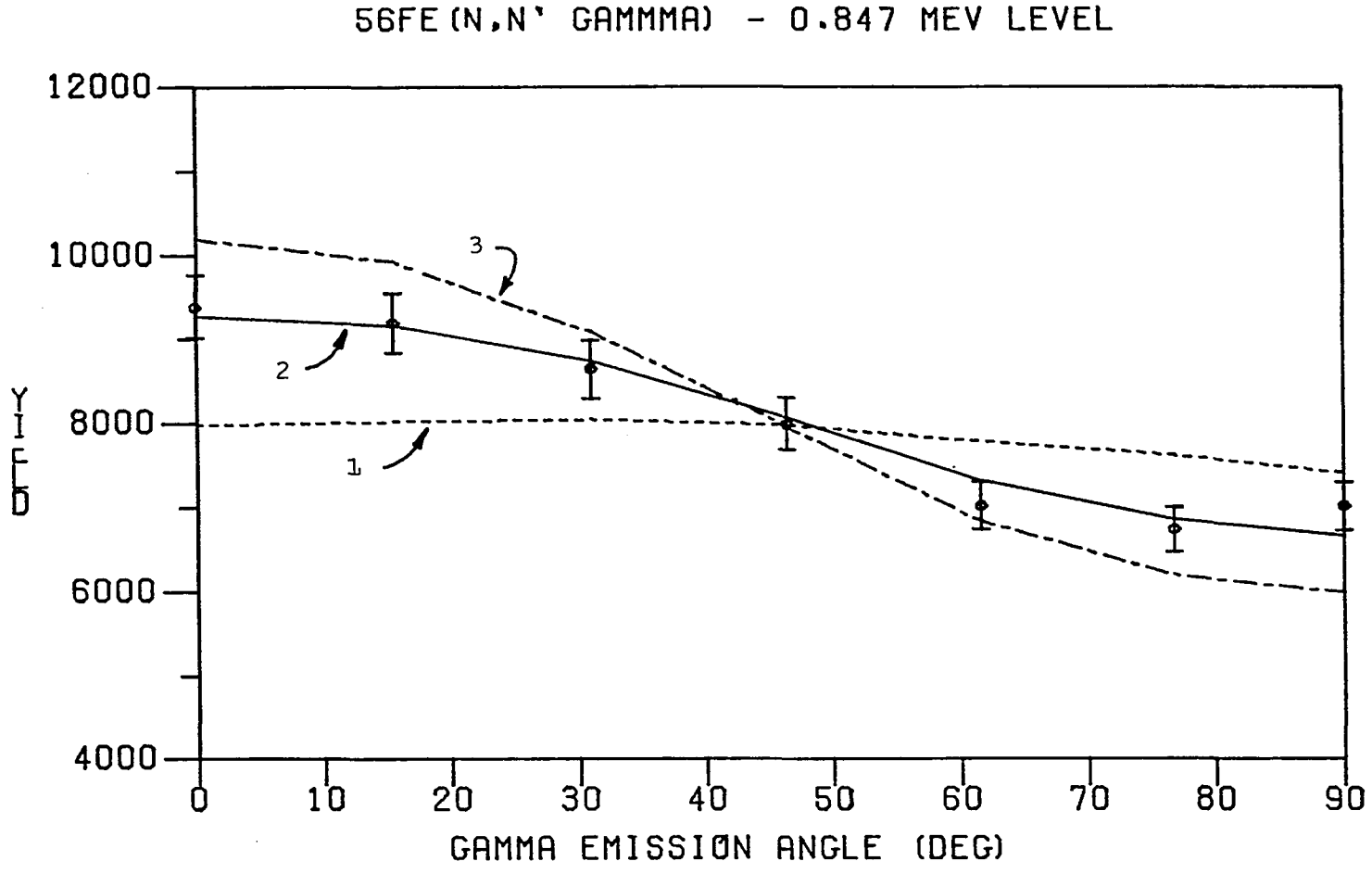
56FE(N,N' GAMMMA) - 0.847 MEV LEVEL
12000
10000
8000
6000
4000
YIELD
0
10
20
30
40
50
60
70
80
90
GAMMA EMISSION ANGLE (DEG)
1
2
3

FIGURE 4-3

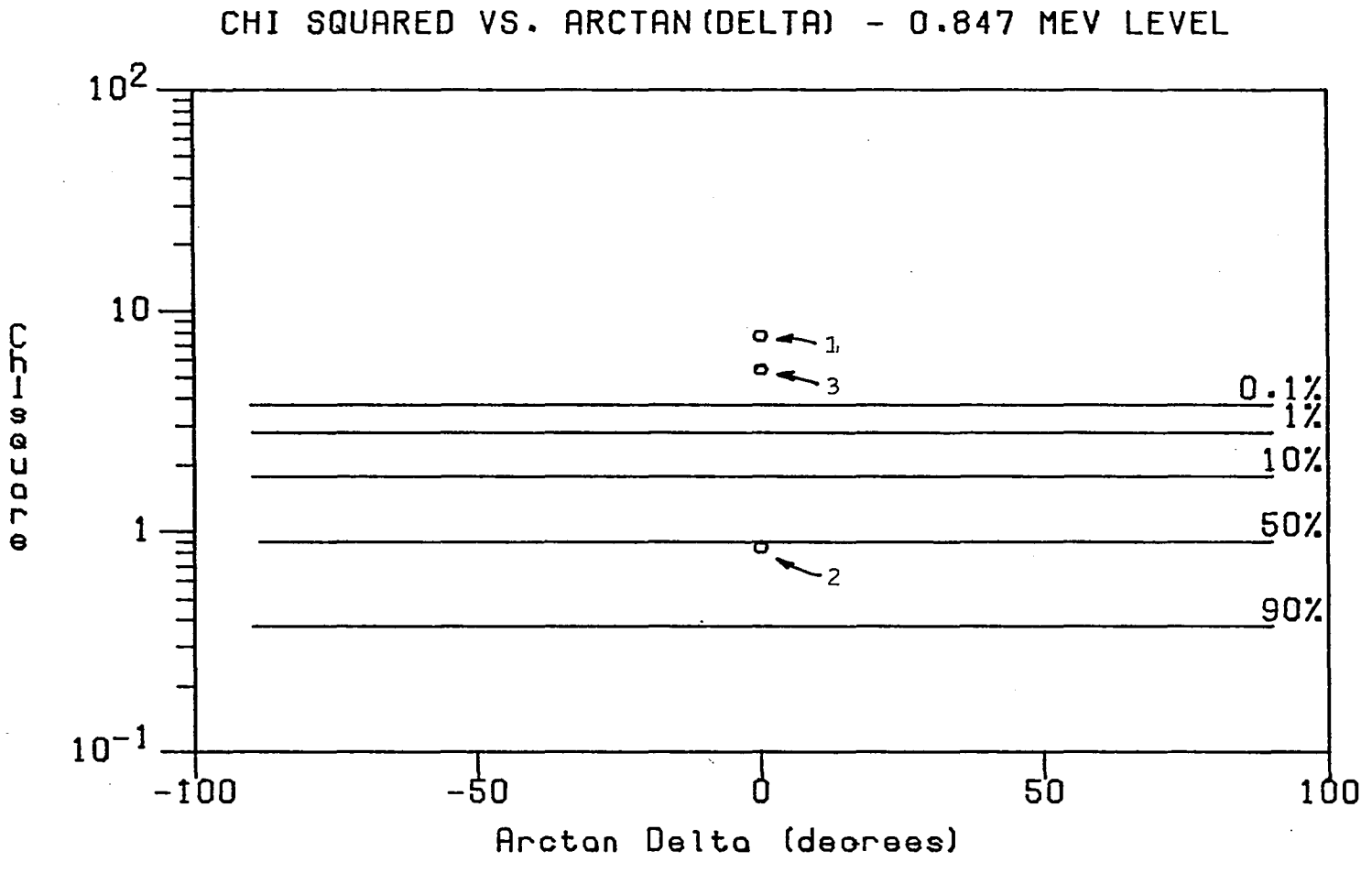
CHI SQUARED VS. ARCTAN(DELTA) - 0.847 MEV LEVEL
10^2
10
1
10^{-1}
CHI SQUARED
1
3
2
0.1%
1%
10%
50%
90%
-100
-50
0
50
100
Arctan Delta (degrees)

FIGURE 4-4

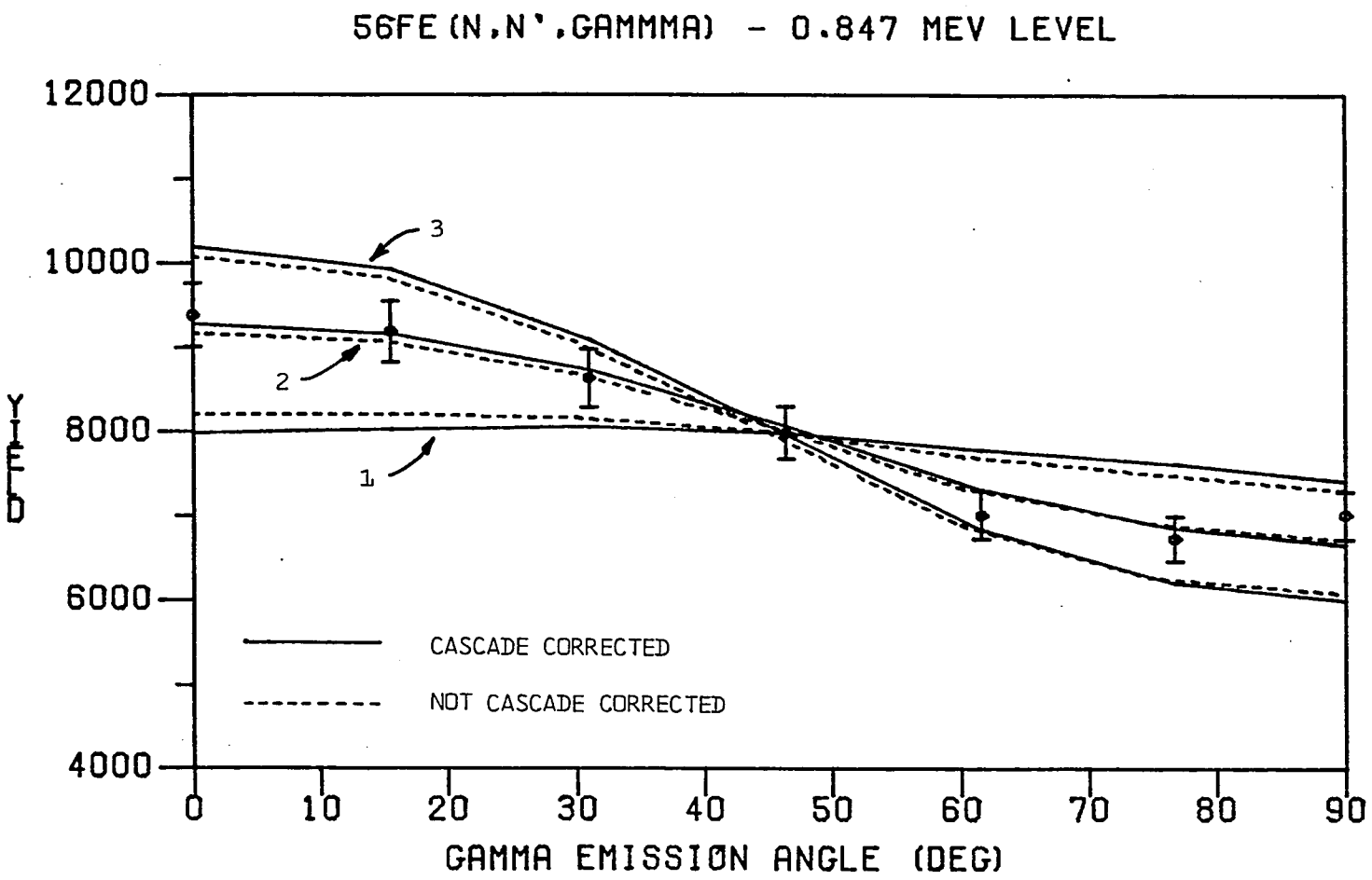
56FE(N,N',GAMMMA) - 0.847 MEV LEVEL
12000
10000
8000
6000
4000
YIELD
3
2
1
CASCADE CORRECTED
NOT CASCADE CORRECTED
0
10
20
30
40
50
60
70
80
90
GAMMA EMISSION ANGLE (DEG)

FIGURE 4-5

Table 4-1

Angular Distribution Fits to ^{56}Fe Data

	No Cascade		Cascade	
J_2	χ^2	%	χ^2	%
3	4.34	0.02	5.37	0.00
2	1.27	27.74	0.84	54.24
1	5.42	0.00	7.67	0.00

J_2 = hypothesized spin for 0.847 MeV level of ^{56}Fe

χ^2 = reduced χ^2

% = percent confidence

gamma emission cross sections, $d\sigma/d\Omega$, and total gamma emission cross sections, σ. All $d\sigma/d\Omega$ are given at 90° in mb/sr and σ are given in mb. In order to calculate $d\sigma/d\Omega$ we must first determine C, as discussed previously, using the yield of the 0.847 MeV transition at 90°. Solving for C and carrying out the computation, we find

$$C = (2.0 \pm 0.2) \times 10^{21} \text{ mb/sr}$$

Then $d\sigma/d\Omega$ can be determined for any other transition with the substitution of the appropriate factors into the equation for $d\sigma/d\Omega$. To calculate σ from $d\sigma/d\Omega$ we use the measured value of $d\sigma/d\Omega$ to renormalize the angular distribution calculated by MANDYF and determine the coefficient a_0. Then σ is given by

$$\sigma = \int (d\sigma/d\Omega)\, d\Omega = \int a_\nu P_\nu(\cos\theta_1)\, d\Omega = 4\pi a_0$$

This corrects for the anisotropy in the angular distribution and provides a more realistic result than simply estimating σ by $\sigma = 4\pi d\sigma/d\Omega$. The values of $d\sigma/d\Omega$ and σ obtained for 3 MeV neutrons incident on ^{56}Fe and producing 1.24 and 1.81 MeV gamma radiation are given in Table 4-2. From Table 4-2 it is evident that agreement between the present results and previous measurements is good, which indicates that this method of obtaining $d\sigma/d\Omega$ and σ works. In the next section these techniques will be applied to antimony.

Table 4-2

Gamma Emission Cross Sections for $^{56}Fe(n,n'gamma)$ at 90° for E_n = 3.0 MeV

E_γ (MeV)	Type	Present	Benjamin (1966)	Habbani (1976)	BNL (1966)
1.24	$d\sigma/d\Omega$	8.2±1.1	9.7±1.9	8.2±0.9	
	σ	132±18	173±35		~100
1.81	$d\sigma/d\Omega$	10.2±1.5	12.3±1.9	7.6±1.0	
	σ	135±20	186±37		~140

$d\sigma/d\Omega$ = differential gamma emission cross section in mb/sr

σ = total gamma emission cross section in mb

4-4 ^{121}Sb and ^{123}Sb Angular Distribution Analysis

Natural Sb is composed of two isotopes; ^{121}Sb makes up 42.7% of natural Sb and ^{123}Sb makes up 57.3%. Since both isotopes are present in such large proportion, gamma lines were expected, and observed, from the (n,n'gamma) reaction in both isotopes.

Figure 4-6 shows the decay scheme of ^{121}Sb with all known, or probable, in parentheses, spins and parities entered. This data reflects the most current information available, as of July 7, 1978, from the Evaluated Nuclear Structure Data File (ENSDF) at Oak Ridge National Laboratory, Oak Ridge, Tennessee. The most recent ENSDF data on the levels of ^{123}Sb is presented in Figure 4-7. All of the transitions shown in Figures 4-6 and 4-7 were observed in time-of-flight gated energy spectra and are identified in the spectrum shown in Figure 4-8 (See Appendix F). This spectrum was taken in a 4 hour run at 90° with a flight path length of 30 cm. The sample was 132 g of powdered natural antimony in a plastic vial of interior dimensions 3.20 cm in length by 3.80 cm in diameter. The background spectrum corresponding to this Sb spectrum is given in Figure 4-9. Again note that the Sb lines of interest are well resolved from any background lines. Some of the low lying Sb levels in the 0.5 MeV region were also observed, however, the spins of these levels are well known so efforts here were concentrated on the three strongest and most distinct transitions at 0.910 MeV and 0.999 MeV in

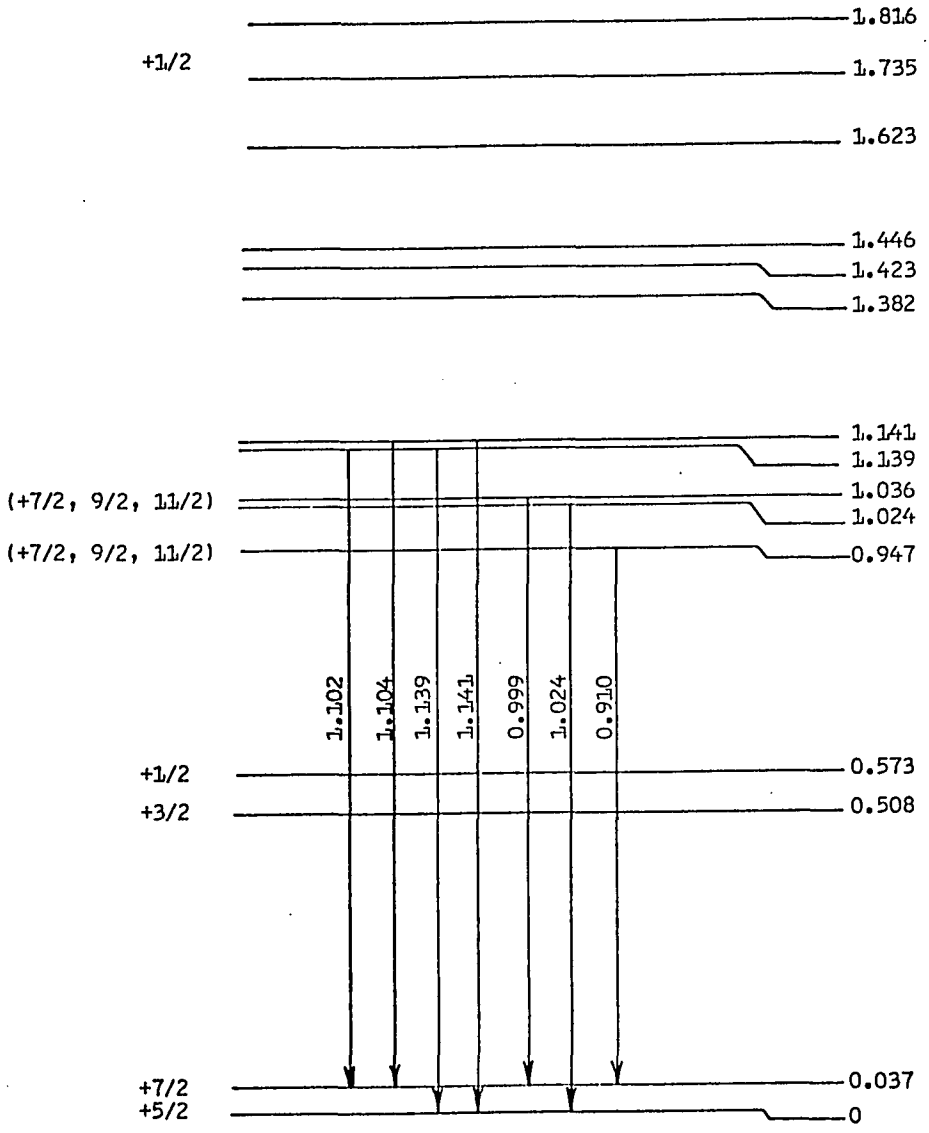

$^{121}_{51}Sb$

FIGURE 4-6

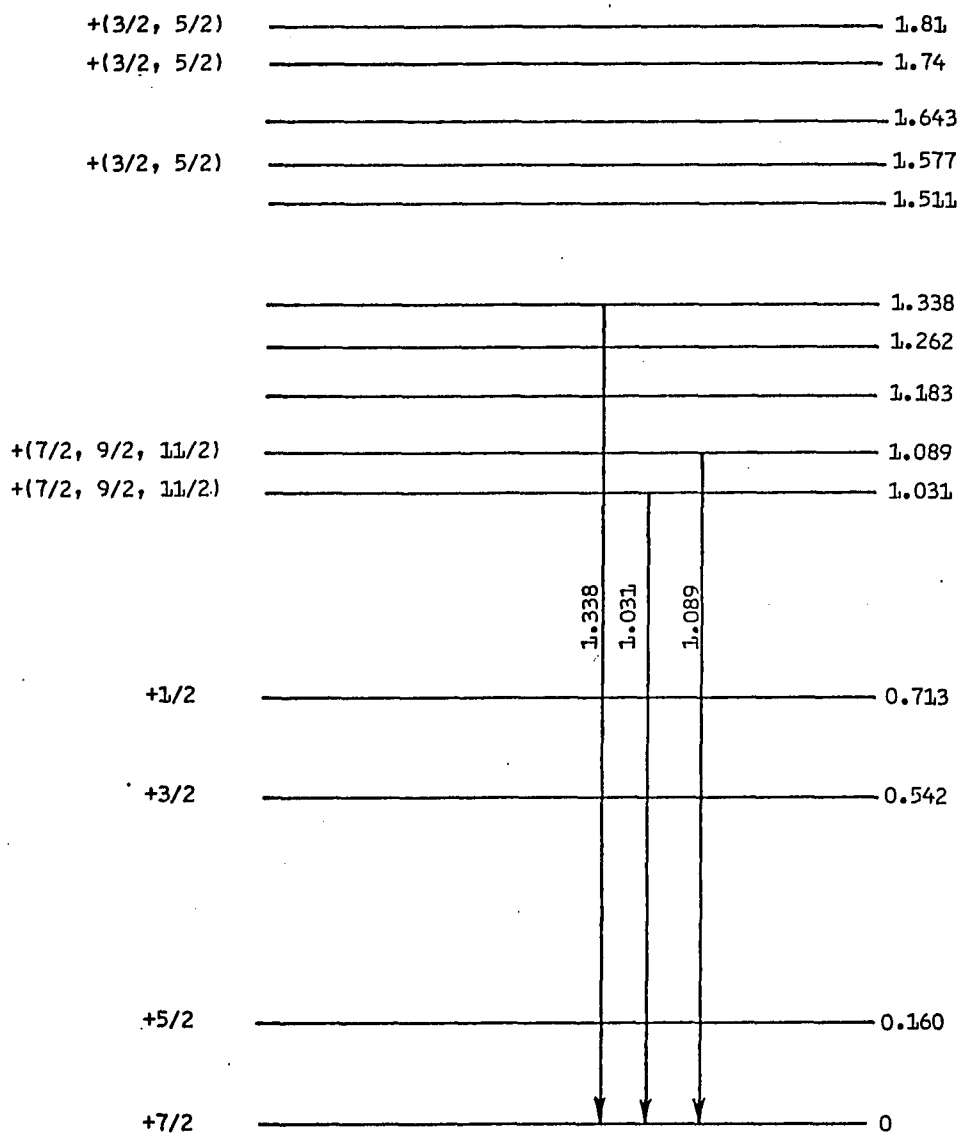

$^{123}_{51}Sb$

FIGURE 4-7

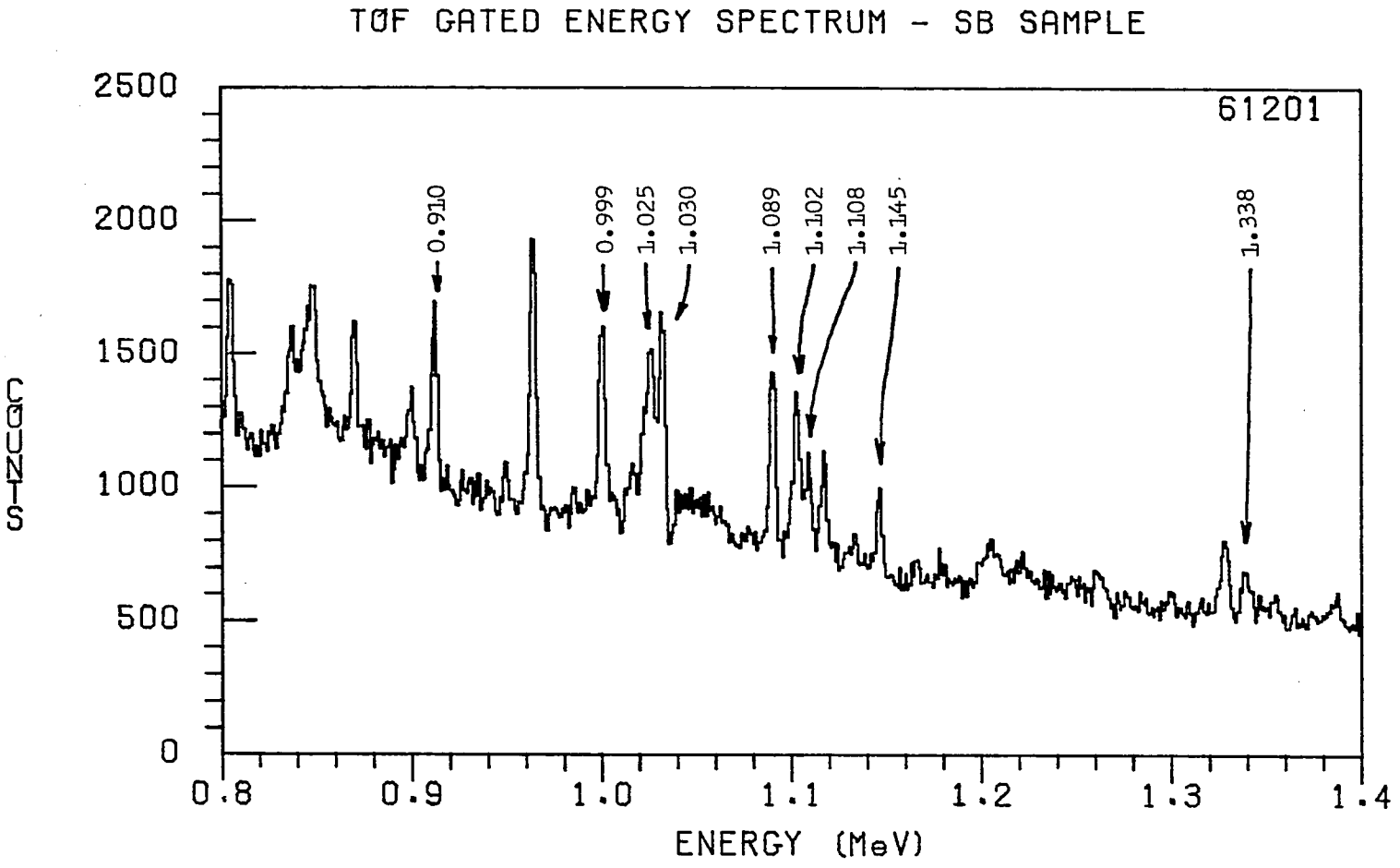
TØF GATED ENERGY SPECTRUM - SB SAMPLE
61201
2500
2000
1500
1000
500
0
0.8
0.9
1.0
1.1
1.2
1.3
1.4
ENERGY (MeV)
0.910
0.999
1.025
1.030
1.089
1.102
1.108
1.145
1.338

FIGURE 4-8

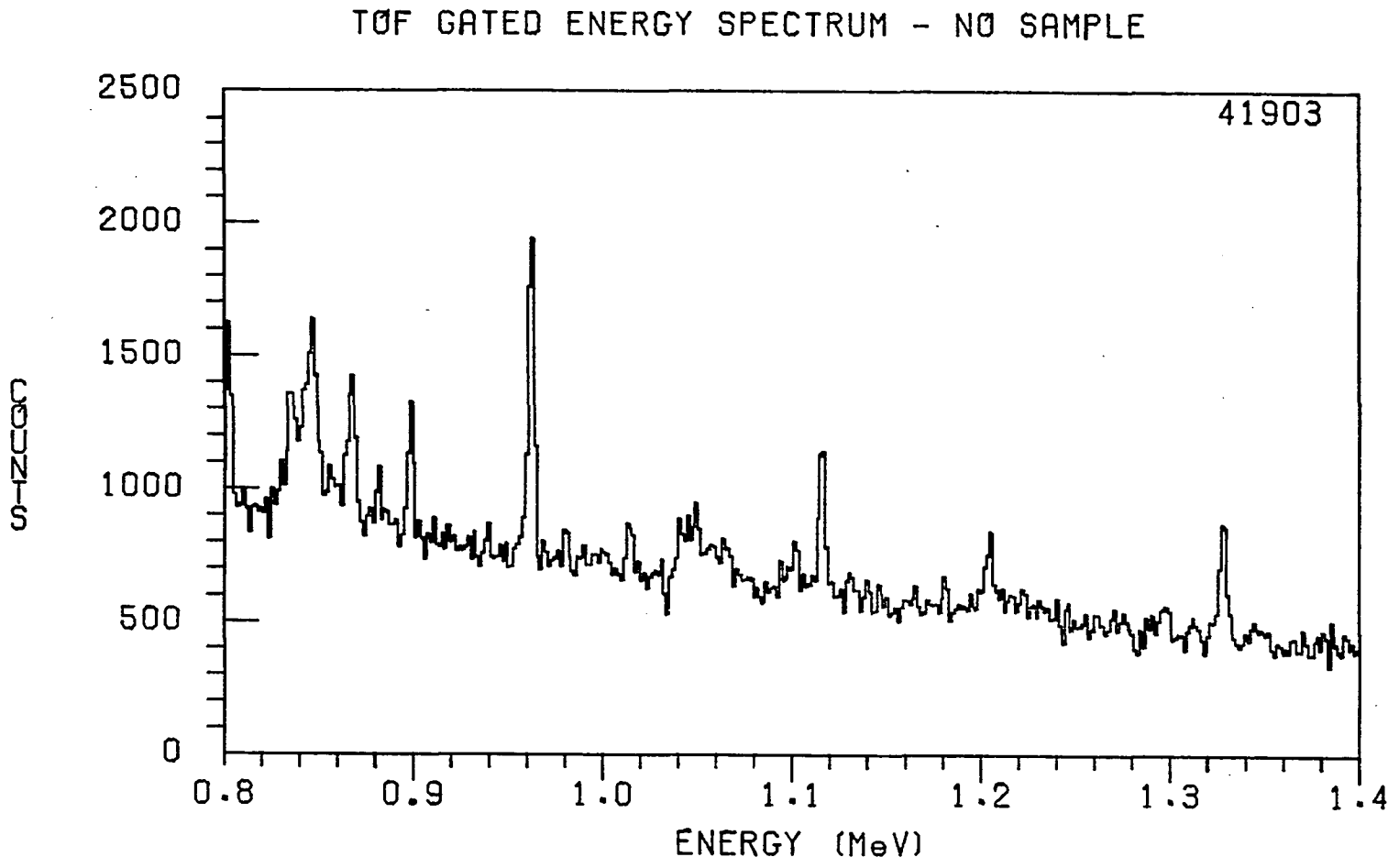
TØF GATED ENERGY SPECTRUM - NØ SAMPLE
41903
2500
2000
1500
1000
500
0
CØUNTS
0.8
0.9
1.0
1.1
1.2
1.3
1.4
ENERGY (MeV)

FIGURE 4-9

^{121}Sb and 1.089 MeV in ^{123}Sb. Cross section results are also reported for some other less well resolved gamma transitions in Sb. As Figure 4-8 indicates, some of the transitions observed were strong but were very close to each other and so could not be resolved sufficiently for meaningful angular distribution analysis.

To carry out the analysis of angular distributions of Sb we must first evaluate the theoretical angular distribution for hypothesized spins. This requires calculation of the T_{jl} using program SCAT and the Wilmore-Hodgson optical model parameters. Using these T_{jl}, MANDYF produces the B_ν coefficients required by the data analysis program EVA. Input to MANDYF was analogous to that used for ^{56}Fe distributions. The values of l_{1max} and l_{2max} were set at 5 and E_n was allowed to vary between 2.5 MeV and 3.25 MeV. In ^{121}Sb evaluations four extra exit channels were included while in ^{123}Sb evaluations eight extra channels were included. Cascading was not corrected for because significant transitions from higher levels were not observed. Theoretical angular distributions were generated for a wide range of hypothetical spins of the levels involved. These included a wider range of possible combinations than the 7/2 - 11/2 range suggested by other experiments (ENSDF, 1978). Figures 4-10 through 4-12 show the theoretical distributions calculated by MANDYF for the three transitions of interest with 7/2 - 11/2 spins. The $\delta = 0$ distributions are shown in solid lines. The dashed

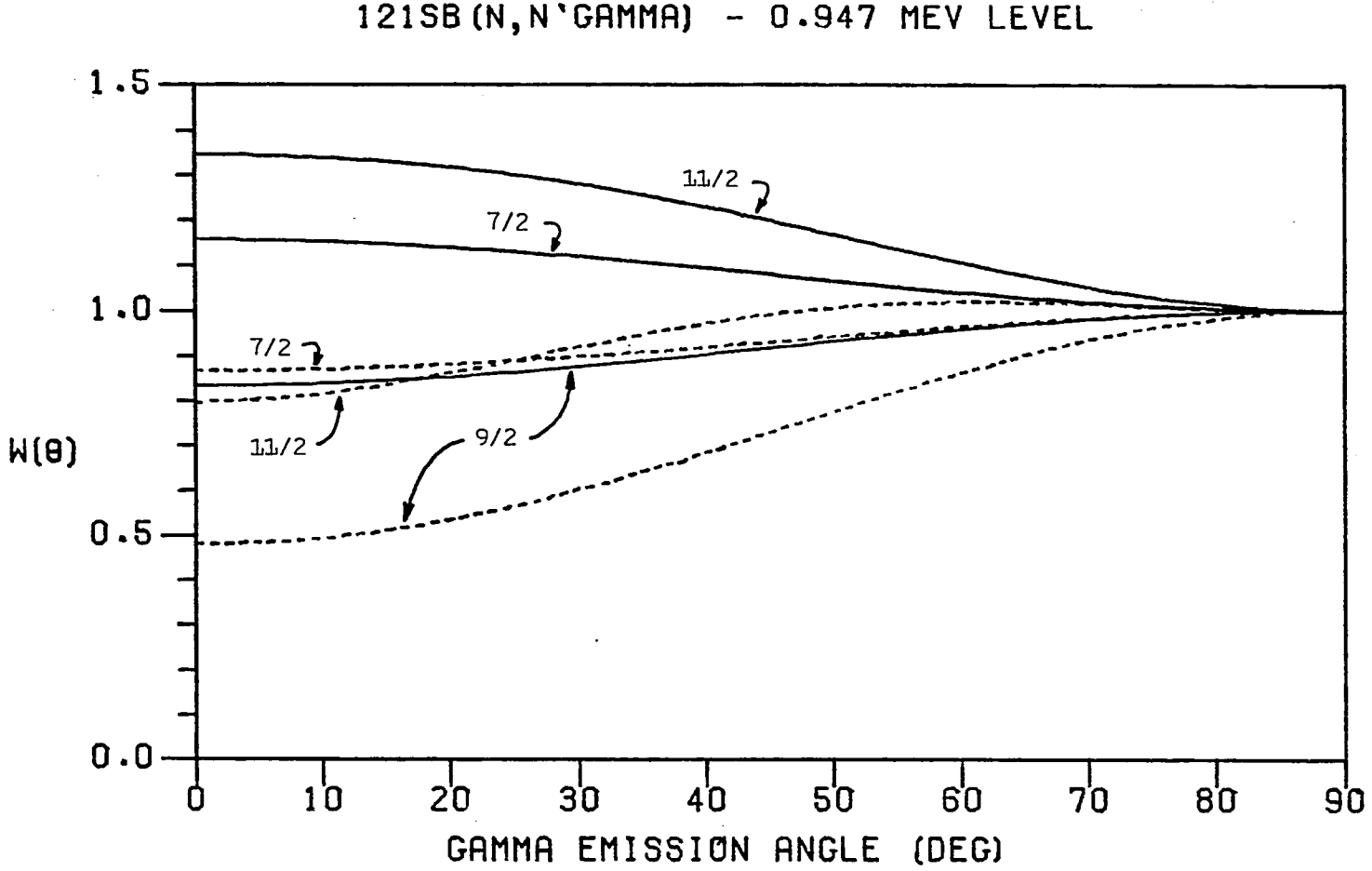
121SB(N,N'GAMMA) - 0.947 MEV LEVEL
1.5
1.0
0.5
0.0
W(θ)
11/2
7/2
7/2
11/2
9/2
0
10
20
30
40
50
60
70
80
90
GAMMA EMISSION ANGLE (DEG)

FIGURE 4-10

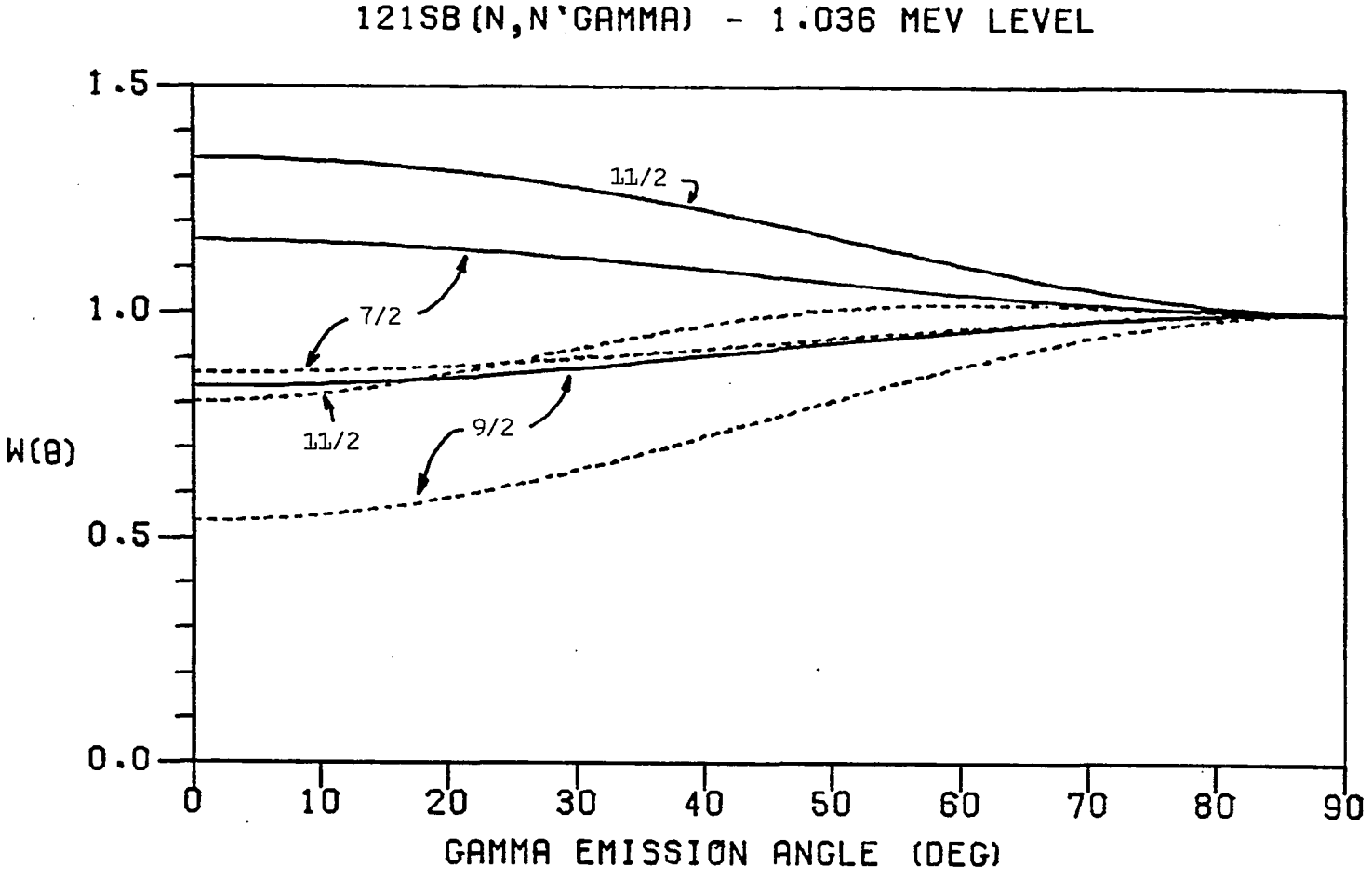
121SB(N,N'GAMMA) - 1.036 MEV LEVEL
1.5
1.0
0.5
0.0
W(θ)
11/2
7/2
11/2
9/2
0
10
20
30
40
50
60
70
80
90
GAMMA EMISSION ANGLE (DEG)

FIGURE 4-11

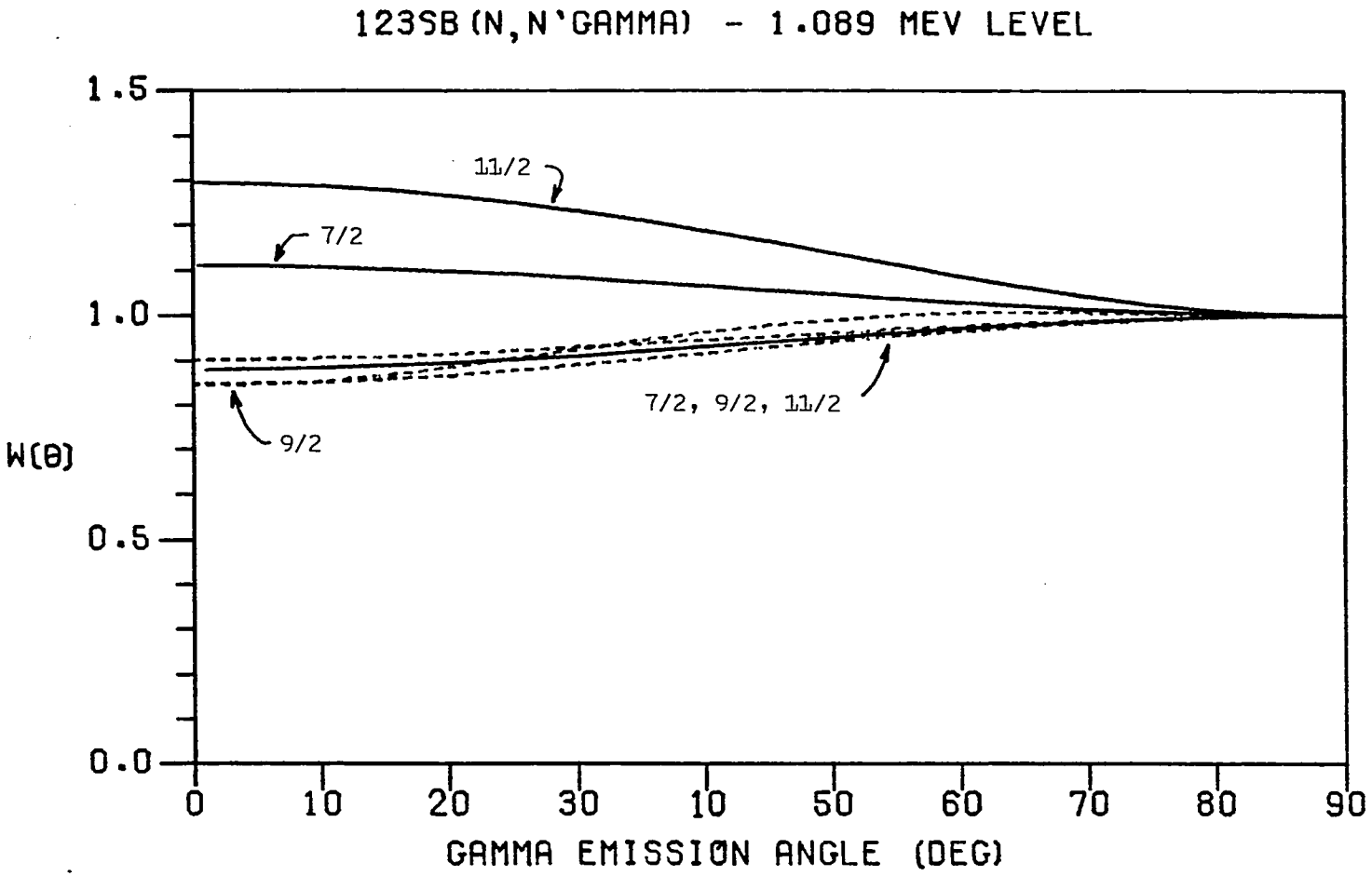
123SB(N,N'GAMMA) - 1.089 MEV LEVEL
1.5
1.0
0.5
0.0
W(θ)
11/2
7/2
7/2, 9/2, 11/2
9/2
0
10
20
30
10
50
60
70
80
90
GAMMA EMISSION ANGLE (DEG)

FIGURE 4-12

lines are the distributions for the best fit values of δ to be discussed in connection with each level later. Note that the angular distribution is strongly influenced by the mixing ratio.

Results of fits produced by EVA over a limited range of spins for the three transitions of interest in Sb are shown in Figures 4-13 through 4-18. Full numerical results are given in Tables 4-3, 4-4 and 4-5. It should be emphasized that the χ^2 quoted in Tables 4-3 through 4-5 are just values from the best fit. The range of acceptable δ is wide and is shown more clearly in the plot of χ^2 versus arctan(δ).

4-4.1 ^{121}Sb 0.947 MeV Level Distributions

Figures 4-13 and 4-14 show results for three hypothesized transitions from the 0.947 MeV level of ^{121}Sb producing 0.910 MeV gamma radiation

$$0.947 \text{ MeV } (+7/2, +9/2, +11/2) \longrightarrow 0.037 \text{ MeV } (+7/2)$$

From Figure 4-13 it is evident that the 9/2 assignment (solid lines) for the 0.947 MeV level provides the best fit to the experimental yields, however, the results are not conclusive. Figure 4-14 shows the variation of χ^2 as a function of arctan(δ). Because these transitions are not of pure multipolarity, the graph of χ^2 versus arctan(δ) shows considerable variation with arctan(δ). Figure 4-14 also supports the 9/2 assignment (solid line) but the 7/2 and

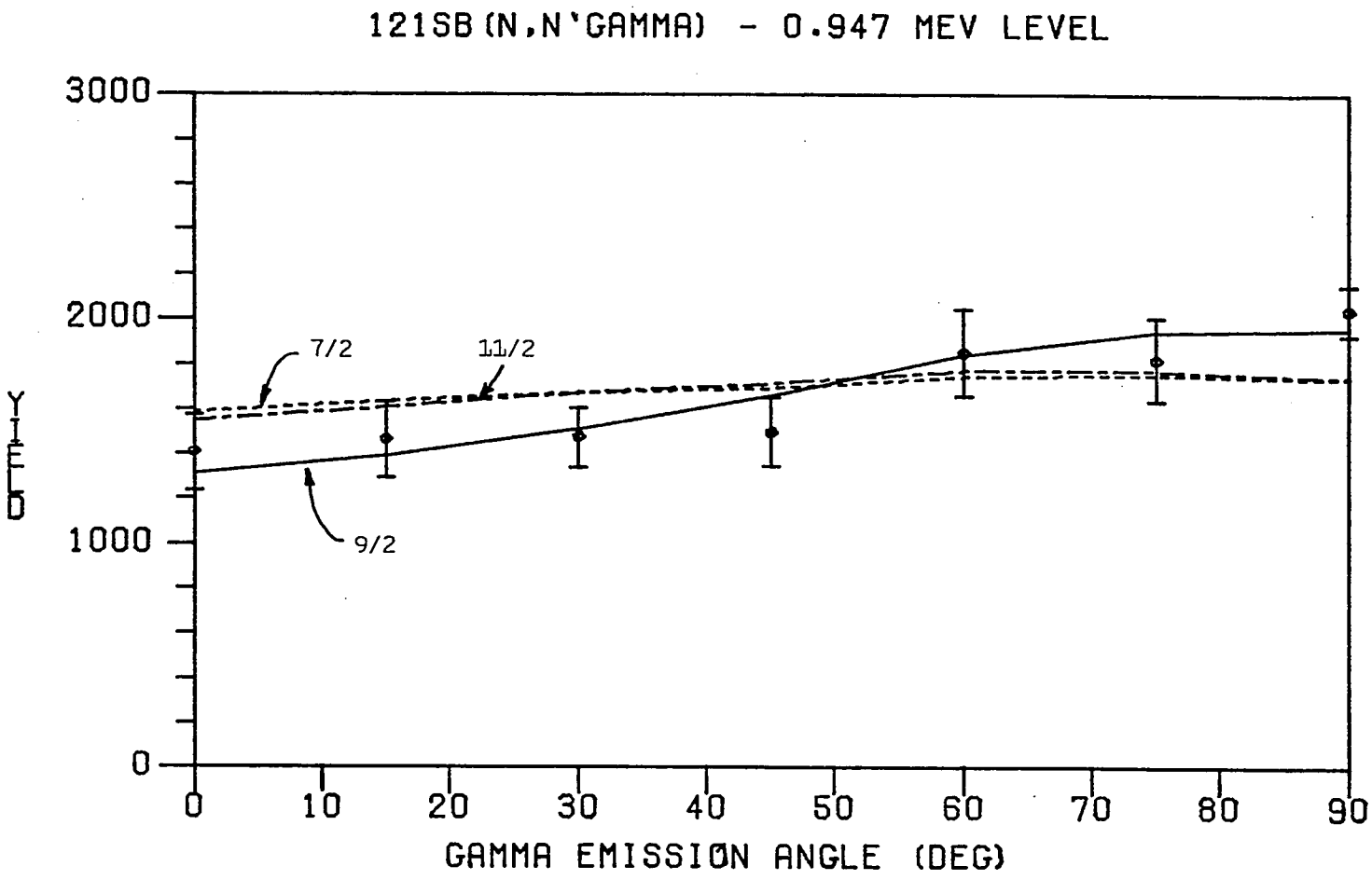
121SB(N,N'GAMMA) - 0.947 MEV LEVEL
3000
2000
1000
0
YIELD
7/2
11/2
9/2
0
10
20
30
40
50
60
70
80
90
GAMMA EMISSION ANGLE (DEG)

FIGURE 4-13

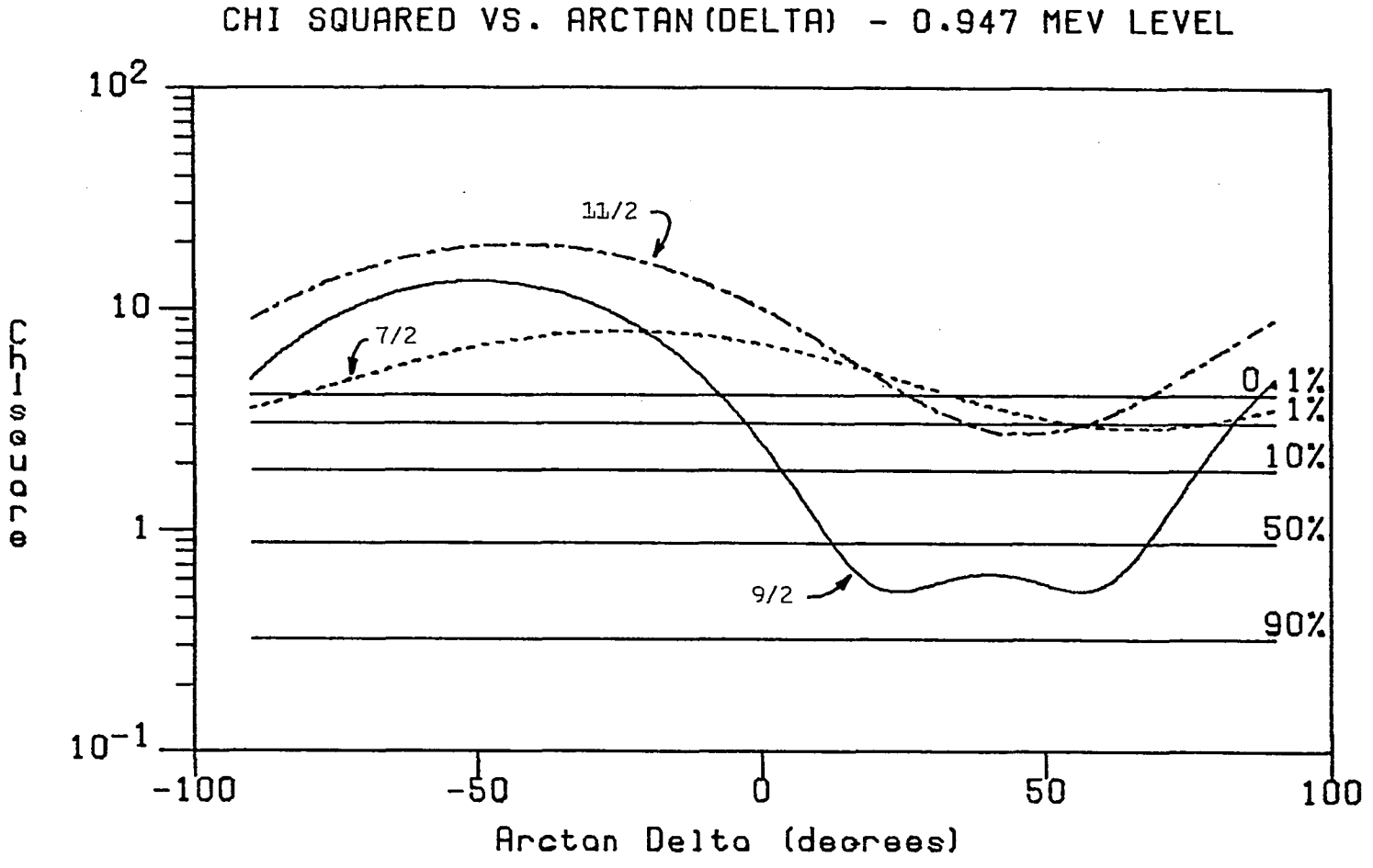
CHI SQUARED VS. ARCTAN(DELTA) - 0.947 MEV LEVEL
10^2
10
1
10^{-1}
CHI-SQUARE
11/2
7/2
9/2
0
1%
1%
10%
50%
90%
-100
-50
0
50
100
Arctan Delta (degrees)

FIGURE 4-14

Table 4-3

^{121}Sb Angular Distribution Fits - 0.947 MeV Level

0.910 MeV Gamma Transition

J_1	χ^2	%	δ
1/2	4.64	0.03	0.00
3/2	4.15	0.09	-1.88
5/2	2.57	2.45	-1.15
7/2	2.87	1.34	2.25
9/2	0.53	75.44	0.45
11/2	2.73	1.78	1.07
13/2	8.34	0.00	1.19

J_1 = hypothesized spin for 0.947 MeV level of ^{121}Sb

χ^2 = reduced χ^2

% = percent confidence

δ = mixing ratio for best fit

11/2 assignments are still possible at a confidence level of ~ 1%. If the 9/2 assignment is assumed correct, then acceptable values of arctan(δ) run from ~ 0° to ~ 85°. A transition from a 9/2 → 7/2 level allows values of L in the range

$$1 \leq L \leq 8$$

Of course only the L = 1 and 2 are likely with δ giving the ratio of L = 2 to L = 1. If arctan(δ) = 0°, then δ = 0 and the transition is pure L = 1. At the other extreme, if arctan(δ) = 85°, then $\delta \sim 11$ and the transition is almost pure L = 2. Assuming a + parity assignment for this level makes the 0.910 MeV gamma from decay of the 0.947 MeV level an admixture of M1 and E2.

There is other evidence to support a 9/2 assignment to the 0.947 MeV level. Theoretical calculations by Vanden Berghe et al., (1971) suggest the existence of two or three +9/2 levels in the 1 MeV region of ^{121}Sb. More recently, in a study of beta decay from ^{121}Te to ^{121}Sb, Meyer et al., (1975) report a +9/2 assignment for the ^{121}Sb 0.947 MeV level.

4-4.2 ^{121}Sb 1.036 MeV Level Distributions

Figures 4-15 and 4-16 give the results for the following transitions in ^{121}Sb producing 0.999 MeV gamma radiation of mixed multipolariy

1.036 MeV (+7/2, +9/2, +11/2) → 0.037 MeV (+7/2)

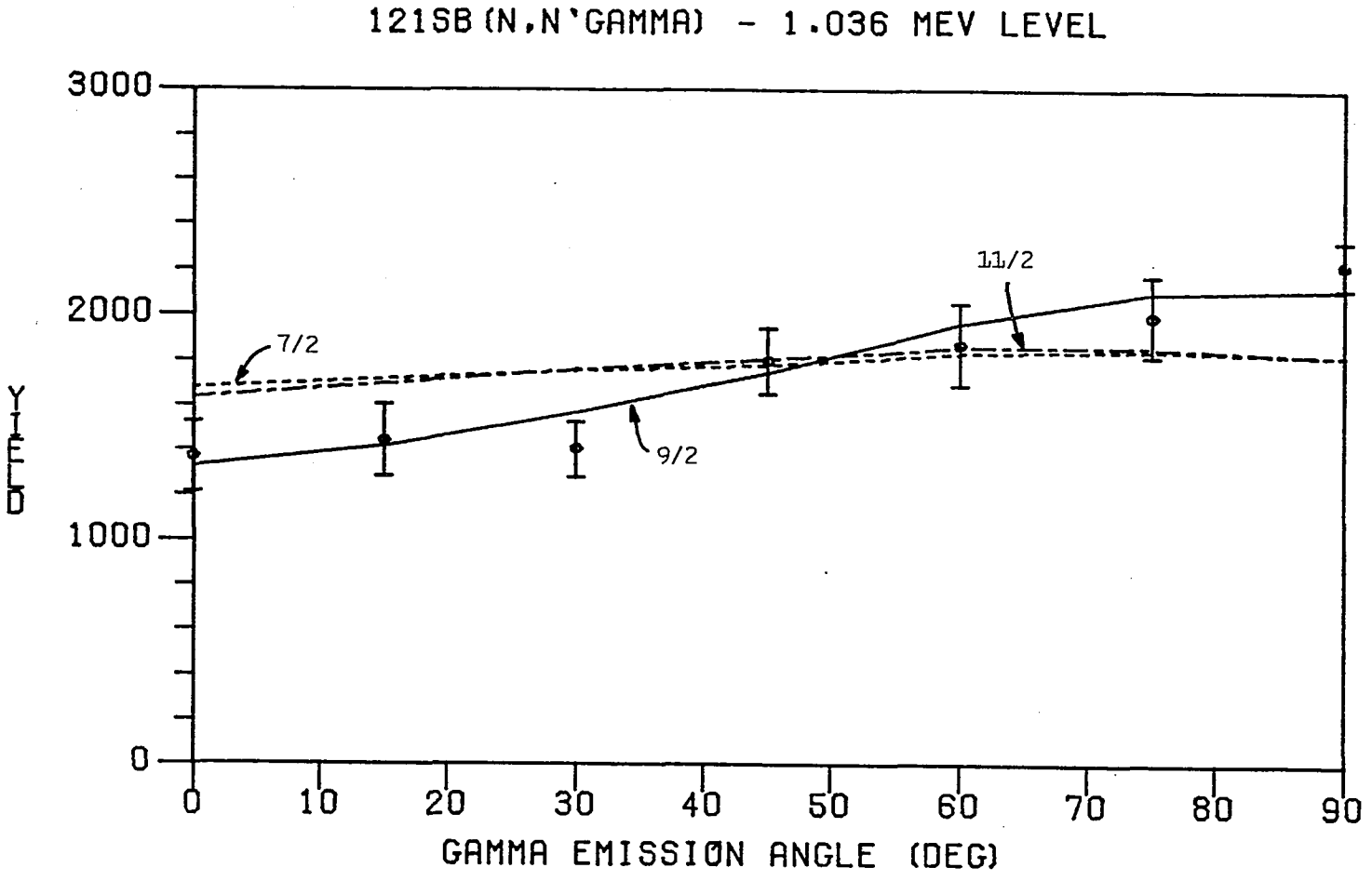
121SB(N,N'GAMMA) - 1.036 MEV LEVEL
3000
2000
1000
0
YIELD
7/2
9/2
11/2
0
10
20
30
40
50
60
70
80
90
GAMMA EMISSION ANGLE (DEG)

FIGURE 4-15

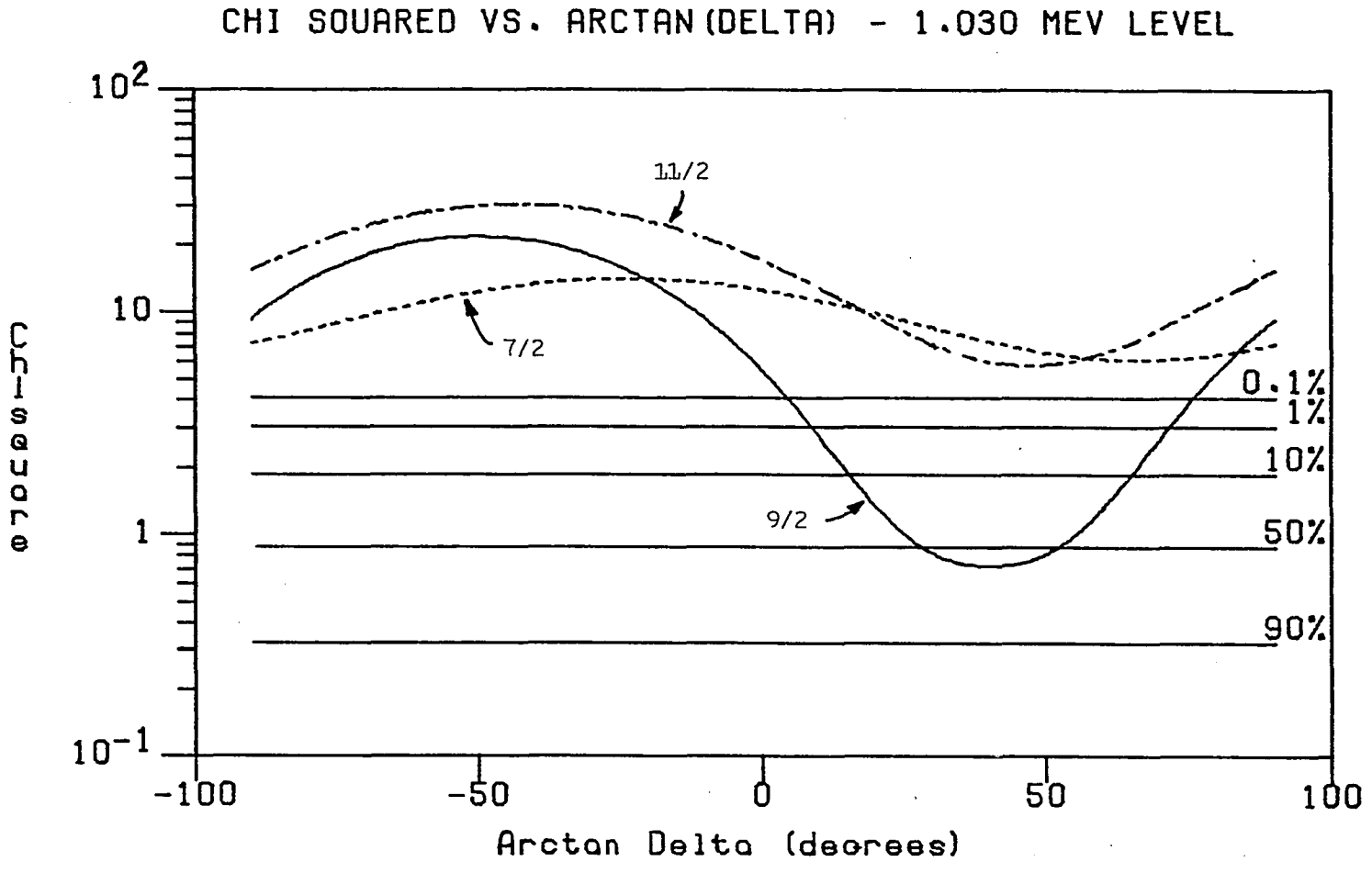
CHI SQUARED VS. ARCTAN(DELTA) - 1.030 MEV LEVEL
10^2
10
1
10^{-1}
Chi-square
11/2
7/2
9/2
0.1%
1%
10%
50%
90%
-100
-50
0
50
100
Arctan Delta (degrees)

FIGURE 4-16

Table 4-4

^{121}Sb Angular Distribution Fits - 1.036 MeV Level

0.999 MeV Gamma Transition

J_2	χ^2	%	δ
1/2	8.96	0.00	0.00
3/2	8.23	0.00	-1.88
5/2	5.66	0.00	-1.15
7/2	6.07	0.00	2.25
9/2	0.72	61.14	0.84
11/2	5.73	0.00	1.07
13/2	14.44	0.00	1.19

J_2 = hypothesized spin for 1.036 MeV level of ^{121}Sb

χ^2 = reduced χ^2

% = percent confidence

δ = mixing ratio for best fit

Figure 4-15 presents somewhat more conclusive results for the 1.036 MeV level than those obtained for the 0.947 MeV level. Here the 9/2 assignment (solid line) appears to fit the experimental yields considerably better than the 7/2 and 11/2 assignments. Figure 4-16 indicates that the only acceptable assignment for the 1.036 MeV level is 9/2. The confidence levels of fits to 7/2 and 11/2 are far below 0.1%. In this case the range of acceptable arctan(δ) is from ~ 10° to ~ 75°. The best fit value of $\delta = 0.84$ and a + parity assumption leads to the conclusion that the 0.999 MeV gamma from this transition is an admixture of ~ 60% M1 and ~40% E2.

Again the theoretical results of Vanden Berghe and the experimental work of Meyer support a +9/2 assignment to the 0.999 MeV level of ^{121}Sb. Combined with the results of this experiment, a +9/2 assignment for this level appears reasonable.

4-4.3 ^{123}Sb 1.089 MeV Level Distributions

The results of fits to the gamma angular distribution from the 1.089 MeV level of ^{123}Sb are given in Figures 4-17 and 4-18. The following transition sequences are considered

1.089 MeV (+7/2, +9/2, +11/2) $\longrightarrow$ G.S. (+7/2)

Numerical results over a wider range of spins appear in Table 4-5. As shown in Figure 4-17, the 7/2, 9/2, and 11/2

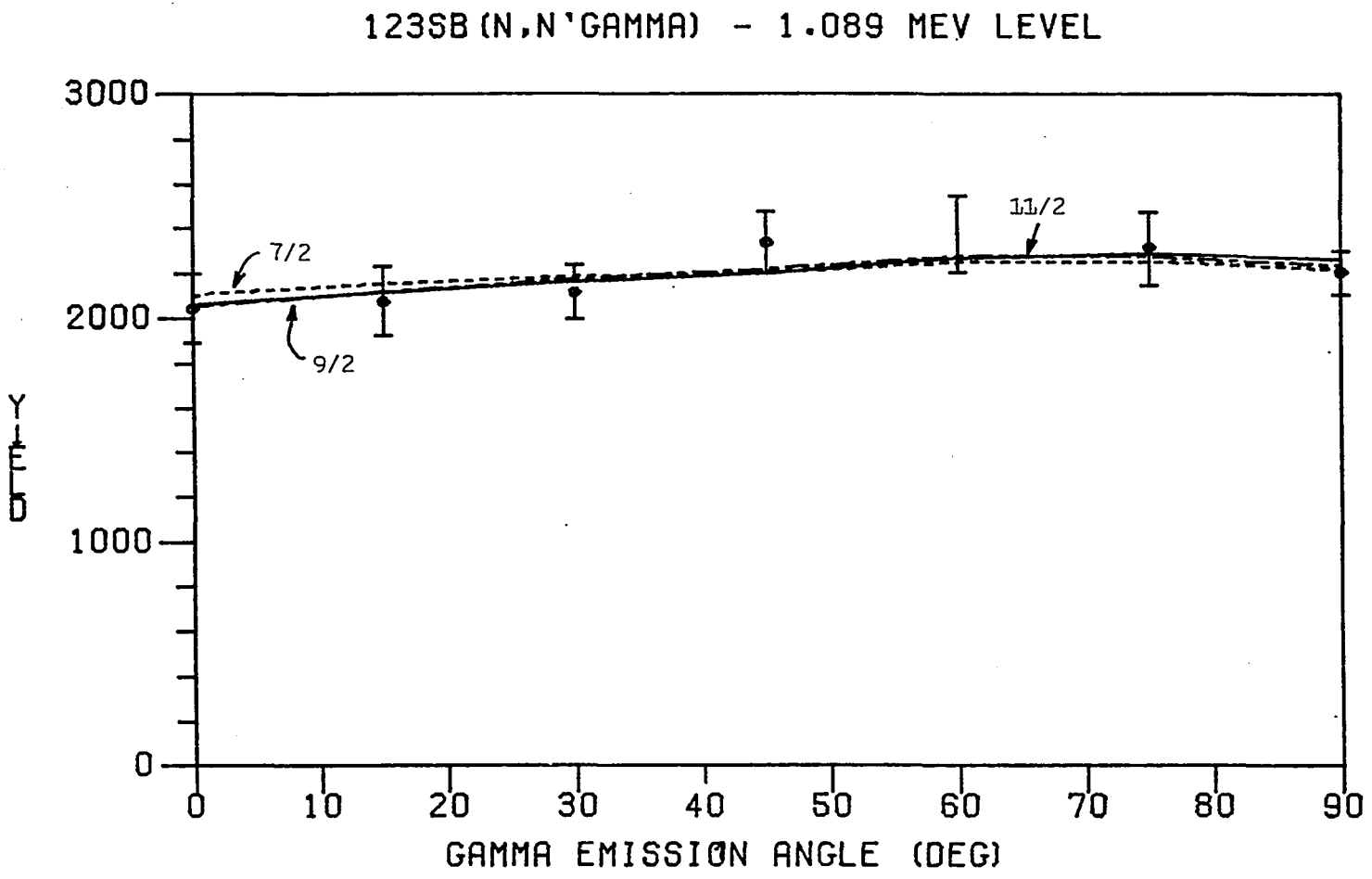
123SB(N,N'GAMMA) - 1.089 MEV LEVEL
3000
2000
1000
0
YIELD
7/2
9/2
11/2
0
10
20
30
40
50
60
70
80
90
GAMMA EMISSION ANGLE (DEG)

FIGURE 4-17

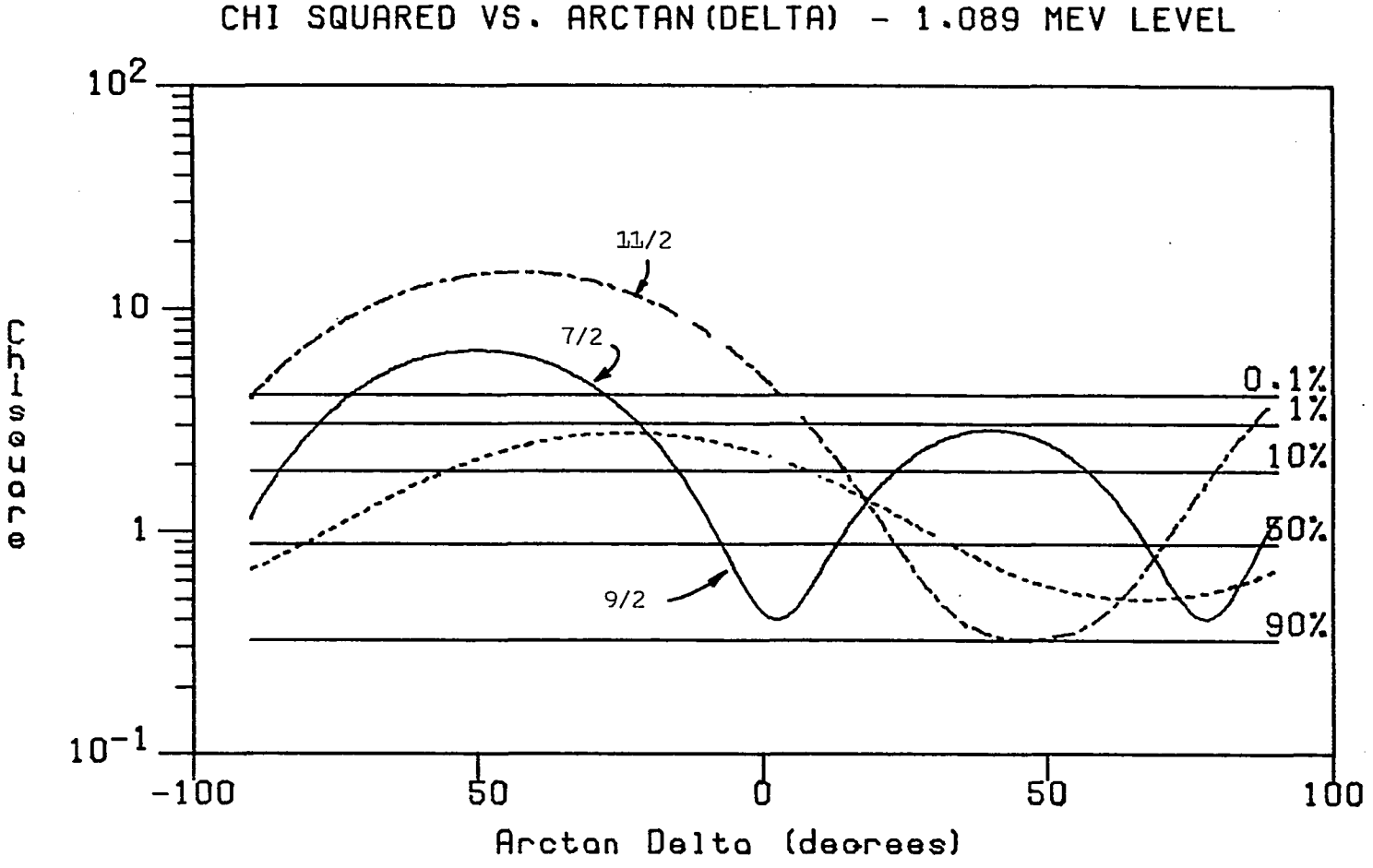
CHI SQUARED VS. ARCTAN(DELTA) - 1.089 MEV LEVEL
10^2
10
1
10^{-1}
Chi-square
11/2
7/2
9/2
0.1%
1%
10%
50%
90%
-100
50
0
50
100
Arctan Delta (degrees)

FIGURE 4-18

Table 4-5

^{123}Sb Angular Distribution Fits - 1.089 MeV Level

1.089 MeV Gamma Transition

J_2	χ^2	%	δ
1/2	1.07	37.51	0.00
3/2	1.01	41.17	0.53
5/2	0.86	50.27	-1.15
7/2	0.49	78.00	2.25
9/2	0.39	85.03	4.70
11/2	0.32	89.89	1.04
13/2	3.40	0.45	1.19

J_2 = hypothesized spin for 1.089 MeV level of ^{123}Sb

χ^2 = reduced χ^2

% = percent confidence

δ = mixing ratio for best fit

assignments for the 1.089 MeV level all provide reasonable fits to the experimental yields. This is supported by the acceptable χ^2 shown for all three assignments in Figure 4-18. Thus no probable spin assignment can be made to this level.

4-5 ^{121}Sb and ^{123}Sb Cross Section Analysis

Differential and total gamma emission cross sections for Sb are determined as for ^{56}Fe. Results are given in Table 4-6 for the three previously discussed gamma transitions in ^{121}Sb and ^{123}Sb. Also included are differential gamma emission cross sections for the 1.338 MeV transition in ^{123}Sb and the region of 1.145 MeV which can include transitions from two closely spaced lines in ^{121}Sb at 1.141 and 1.139 MeV. These cross sections have all been corrected for isotopic abundance. Table 4-6 also contains approximate values for differential gamma emission cross sections of the two sets of closely spaced lines in the 1.025 and 1.102 MeV regions. Because each of these regions can correspond to transitions in ^{121}Sb as well as ^{123}Sb, the cross sections given are for natural Sb and are uncorrected for isotopic abundance.

Very little work on gamma emission cross sections for the Sb (n,n'gamma) reaction has been done by other experimenters. The only value of $d\sigma/d\Omega$ available for comparison is given for E_n= 3.29 MeV and is quoted as 18.2 ± 1.9 mb/sr at 90° (Habbani and Jiggins, 1976). This

Table 4-6

Gamma Emission Cross Sections for Sb

at 90° for E_n = 3.0 MeV

E_γ	$d\sigma/d\Omega$	σ	Comments
0.910	13.0 ± 2.0	137 ± 21	I,R,A
0.999	12.9 ± 1.9	133 ± 20	I,R,A
1.025	19.1 ± 1.9	240 ± 36	NI,NR,NA
1.089	21.1 ± 3.0	265 ± 40	I,R,A
1.102	12.2 ± 2.4	153 ± 23	NI,NR,NA
1.145	5.0 ± 1.5	62 ± 9	I,NR,NA
1.338	4.0 ± 1.5	50 ± 8	I,R,NA

$d\sigma/d\Omega$ = differential gamma emission cross section in mb/sr

σ = total gamma emission cross section in mb

I = corrected for isotopic abundance

R = gamma line is well resolved from other lines

A = total cross section is corrected for anisotropy

Note: The prefix N in Comments denotes that the negation of the comment is true. For instance, NI,NR,NA denotes that no correction for isotopic abundance was made, that the line was poorly resolved, and that the total cross section was approximated by $\sigma = 4\pi d\sigma/d\Omega$.

figure is given for a gamma energy of 1.010 MeV, however, it is difficult to determine which Sb transitions are included because the gamma detector used was a NaI(Tl) crystal without sufficient resolution to separate the closely spaced lines in that region.

V. CONCLUSION

In reviewing this research it would seem that most of the goals set out in Chapter I have been reached. Using the known +2 spin assignment for the 0.847 MeV level of ^{56}Fe, we have shown that the statistical compound nucleus theory can be then applied to the evaluation of gamma angular distributions and by comparison with experiment, result in a correct spin assignment. This confirms the validity of the statistical compound nucleus theory as well as the technique for data acquisition and analysis. As a fringe benefit, we have also shown how gamma emission cross sections, so essential to applications of neutron physics, can be obtained relative to the well established result for the 0.847 MeV ^{56}Fe level.

Having demonstrated the success of this technique with ^{56}Fe, it was applied to ^{121}Sb and ^{123}Sb where 9/2 spin assignments were made for the 0.947 and 1.036 MeV ^{121}Sb levels. This result is especially satisfying as it agrees with the assignment deduced from a completely different type

of experiment (Meyer et al., 1975). Also gamma emission cross sections for the (n,n'gamma) reaction corresponding to several ^{121}Sb and ^{123}Sb transitions were reported which have not been reported in the literature previously.

At this point there are several suggestions which can be made to future experimenters. The first and most obvious suggestion is that all steps be taken to maximize neutron flux in the sample area. The accelerator capabilities must be improved in every way possible in order to achieve optimum deuteron beam current. In the present research it was found that immediately after accelerator maintainance, ie., source bottle cleaning with HF solution, quite high deuteron beam currents could be produced. Unfortunately, after as short an operating period as 24 hours, the monoatomic yield had dropped to approximately 25% of the initial yield. Another problem associated with reduced neutron yield is the carbon buildup observed on the TiD target. The solution to this problem would probably be to construct a liquid nitrogen cold trap directly upsteam of the target to condense pump oil vapor and prevent its depostion on the TiD target. Both of these problems tend to reduce neutron output. More in the nature of an improvement upon the experimental setup, a new TiD target holder with a still smaller water cooling cavity is suggested. The present target holder has more than sufficient flow capacity and of course placing the sample closer to the neutron source should increase neutron flux considerably.

Another area where this experiment could be improved is in gamma detection efficiency. The Ge(Li) detector utilized in the present experiment is a 40 cm^3 lithium-drifted germanium crystal with a detection efficiency ~ 8% of that for a 3" x 3" NaI(Tl) detector. In recent years much larger hyperpure Ge detectors have become commercially available with volumes of 160 cm^3 and efficiencies about four times higher than the present detector. The use of such a detector in this (n,n'gamma) experiment would increase data collection capabilities by a factor of four over the present experiment. The new hyperpure detectors also have the advantage of not requiring liquid nitrogen cooling when not in use.

Concerning continued research on the Sb(n,n'gamma) reaction, the author suggests the acquisition of isotopically enriched ^{121}Sb and ^{123}Sb samples. Both of these isotopes are available in enriched form to ~ 99% purity. Although the cost of purchasing ~ 50 g of such isotopes is prohibitive, it was found recently that these materials are available on loan from Oak Ridge National Laboratory for a modest fee. Unfortunately this was discovered to late to be of use in the present research. The use of enriched isotopes would allow separation of gamma transitions in ^{121}Sb and ^{123}Sb and produce a much cleaner energy spectrum as well as concentrate the sample material closer to the neutron source and thus increase the neutron flux through the sample.

Coupled with the use of enriched isotopes, the use of an energy variable neutron source would be most interesting. The energy level schemes of the Sb isotopes are not yet fully understood. By observing the gamma transitions in the separate isotopes at various excitation energies, perhaps some of the existing discrepancies could be cleared up. The use of such a neutron source would also be advantageous with natural Sb samples as any cascading could be eliminated by excitation with neutron energies just above the reaction threshold for the level of interest. Producing these neutrons, however, requires the use of higher energy charged particles and a reaction such as the $^{7}Li(p,n)^{7}Be$ or $^{3}H(p,n)^{3}He$ reactions. These reactions have Q values of -1.6 MeV and -0.76 MeV respectively and thus are not available on the UNH 400 keV accelerator.

Bibliography

Auble, R.L. and W.H. Kelly, A Study of ^{123}Sb Levels Populated in the Beta Decay of the High Spin Isomer of ^{123}Sn, Nucl. Phys. 81, 442 (1966).

Auble, R.L., W.H. Kelly and H.H. Bolotin, The Decay of ^{121}Te and ^{121m}Te, Nucl. Phys. 58, 337 (1964).

Barnard, E., N. Coetzee, J.A.M. De Villiers, D. Reitmann, and P. Van Der Merwe, The Energy Levels of ^{121}Sb and ^{123}Sb Isotopes from the (n,n'γ) Reaction, Nucl. Phys. A172, 215 (1971).

Barnes, P.D., C. Ellegaard, B. Herskind and M.C. Joshi, Properties of Levels in ^{121}Sb and ^{123}Sb Excited with the Reactions (^{3}He,d), (d,d') and (^{160},$^{160'}\gamma$), Phys. Lett. 23, 266 (1966).

Becchetti, F.D. and G.W. Greenlees, Nucleon-Nucleus Optical Model Parameters, A>40, E<50 MeV, Phys. Rev. 182, 1190 (1969).

Benjamin, R.W., P.S. Buchanan and I.L. Morgan, Gamma Rays Produced in the ^{56}Fe(n,n'γ)^{56}Fe Reaction, Nucl. Phys. 79, 241 (1966).

Biedenharn, L.C., J.M. Blatt and M.E. Rose, Some Properties of the Racah and Associated Coefficients, Rev. Mod. Phys. 24, 249 (1952).

Biedenharn, L.C. and M.E. Rose, Theory of Angular Correlation of Nuclear Radiations, Rev. Mod. Phys. 25, 729 (1953).

Blatt, John M. and L. C. Biedenharn, The Angular Distribution of Scattering and Reaction Cross Section, Rev. Mod. Phys. 24, 258 (1952).

Blatt, J.M. and V.F. Weisskopf, Theoretical Nuclear Physics, Wiley, New York (1952).

BNL (Brookhaven Nat. Lab.) Report 325, 26-56-7 (1966).

Booth, E.C., R.G. Arnold and W.J. Alston, Resonance Fluorescence Studies. II. ^{121}Sb and ^{123}Sb, Phys. Rev. C 7, 1500 (1973).

Boring, J.W. and M.T. McEllistrem, Differential Cross Sections for (n,n'γ) Reactions in Several Nuclei, Phys. Rev. 124, 1531 (1961).

Coope, D.F., S.N. Tripathi, M.C. Schell, Strong Collective Excitations in Low Energy Neutron Scattering From Transitional Nuclei, Phys. Rev. C 16, 2223 (1977).

Cranberg, Lawrence, Thomas A. Oliphant, Jules Levin, and C.D. Zafriatas, Fast-Neutron Scattering from Nuclides in the Lead Region, Phys. Rev. 159, 969 (1967).

Daniels, J.M. and J. Felsteiner, (n,n'γ) Reactions with 2.8-MeV Neutrons on Cobalt and Copper, Using a Lithium-Drifted Germanium Detector, Bull. Am. Phys. Soc. 10, 1116 (1965).

Davidson, J.M., H.R. Hooper, D.M. Sheppard, and G.C. Neilson, A Small-Sample Method for Studying Gamma-Ray Angular Distributions From the (n,n'gamma) Reaction, Nucl. Instr. and Meth. 134, 291 (1976).

Davidson, J.M., EVA: A Computer Code for the Analysis of γ-Ray Angular Distributions from the (n,n'γ) Reaction, Internal Report No. 79, Nuclear Research Centre, University of Alberta (1976).

Davidson, J.M., P.W. Green, H.R. Hooper, D.M. Sheppard and G.C. Neilson, Intermediate Coupling in ^{203,205}Tl, Phys. Rev. C 15, 635 (1977).

Day, R.B. and M. Walt, Gamma Rays from Neutron Inelastic Scattering in B^{10}, F^{19}, and Fe^{56}, Phys. Rev. 117, 1330 (1960).

Elbakr, S.A., I.J. Van Heerden, W.K. Dawson, W.J. McDonald and G.C. Neilson, A Small Sample Method for Investigation of the (n,n'γ) Reaction, Nucl. Instr. and Meth. 97, 283 (1971).

Elbakr, S.A., I.J. van Heerdan, D.R. Gill, N. Ahmed, W.J. McDonald, G.C. Neilson and W.K. Dawson, Level Structure of ^{160}Gd from the (n,n'γ) Reaction, Phys. Rev. C 10, 1864 (1974).

ENSDF (Evaluated Nuclear Structure Data File), Oak Ridge Nat. Lab., Oak Ridge, Tennesee (1978).

Evans, R.D., The Atomic Nucleus, McGraw-Hill Book Co., New York (1955).

Feshbach, H., C.E. Porter and V.F. Weisskopf, Model for Nuclear Reactions with Neutrons, Phys. Rev. 96, 448 (1954).

Frauenfelder, H. and R.M. Steffen, Angular Correlations, in Alpha-, Beta- and Gamma-Ray Spectroscopy, K. Siegbahn, ed., North-Holland Pub. Co., Amsterdam, Holland, 997 (1966).

Gilboy, W.B. and J.H. Towle, A Neutron Scattering Study of Fe^{56}, Nucl. Phys. 64, 130 (1964).

Green, P.W., B.C. Robertson, and D.M. Sheppard, A Compact Graphical Representation For Gamma-Ray Direction Correlation Coefficients For Aligned Nuclei, Nucl. Instr. and Meth. 98, 45 (1972).

Habbani, Farouk, I., and Alan H. Jiggins, Gamma Emission Cross Sections for 23 Elements Using 3.29 MeV Neutron Inelastic Scattering, Nucl. Instr. and Meth. 134, 542 (1976).

Hauser, Walter and Herman Feshbach, The Inelastic Scattering of Neutrons, Phys. Rev. 87, 366 (1952).

Holmqvist, B. and T. Wielding, Optical Model Analysis of Experimental Fast Neutron Elastic Scattering Data, Atomic Energy Co., Studsvik, Sweden, Report AE-430 (1971).

Hooper, H.R., J.M. Davidson, P.W. Green, D.M. Sheppard and G.C. Neilson, Gamma-Ray Angular Distribution Measurements from the $^{162,164}Dy(n,n'\gamma)$ Reactions, Phys. Rev. C 15, 1665 (1977).

Hosoe, M and S. Suzuki, Gamma Rays from Neutron Inelastic Scattering of Magnesium, Aluminium, Iron, and Bismuth, Jour. Phys. Soc. Jap. 14, 699 (1959).

Kellie, J.D., M.N. Islam, G.I. Crawford, Inelastic Neutron Scattering by ^{56}Fe and ^{31}P in the Energy Range 0.8 to 9.0 MeV, Nucl. Phys. A208, 525 (1973).

Krane, K.S., Solid-Angle Correction Factors for Coaxial Ge(Li) Detectors, Nucl. Instr. and Meth. 98, 205 (1972).

Lachkar, J., J. Sigaud, Y. Patin, and G. Haouat, Gamma-RayProduction Cross Sections for the ^{56}Fe (n,n'gamma) Reaction from 2.5-14.1 MeV Neutron Energies, Nucl. Sci. and Eng. 55, 168 (1974).

Lachkar, J., J. Sigaud, Y. Patin and G. Haouat, Gamma-Ray Production Cross Sections for the $^{56}Fe(n,n'\gamma)$ Reaction from 2.5 to 14.1 MeV Neutron Energies, Acta Phys. Slov. 26, 38 (1976).

Marden, P.J., Reaction Kinematics Program REAKIN, Univ. of N.H., unpublished (1978).

Marmier, P. and E. Sheldon, Physics of Nuclei and Particles, Academic Press, New York, (1971) vol. 1 and 2.

McEllistrem, M.T., Fast Neutron Scattering from some Medium Mass Nuclei, in Proceedings of the International Conference on the Interactions of Neutrons with Nuclei, Univ. of Lowell, Lowell, Mass. July, 1976, Eric Sheldon, ed., (ERDA, Oak Ridge, 1976), CONF-760715-40, 171 (1977).

McEllistrem, M.T., J.D. Brandenberger, K. Sinram, G.P. Glasgow, K.C. Chung, Discovery and assignment of excited 0+ levels in even-A Mo isotopes, Phys. Rev. C 9, 670 (1974).

Meyer, R.A., R.G. Lanier, J.T. Larsen, Two-particle, one-hole states in antimony nuclei and the decay of ^{121}Te, Phys. Rev.C 12, 2010 (1975).

Mohindra, R.K. and D.M.Van Patter, Study of the Level Structure of ^{60}Ni from (p,p'gamma) Angular Distributions, Phys. Rev. B 139, 274 (1965).

Moldauer, P.A., Theory of Average Neutron Reaction Cross Sections in the Resonace Region, Phys. Rev. 123, 968 (1961).

Moldauer, P.A. Average Compound-Nucleus Cross Sections, Rev. Mod. Phys. 42, 1079 (1964).

Nellis, Donald O. and Ira L. Morgan, Neutron-Induced Gamma-Ray production in ^{208}Pb, Phys. Rev.C 9, 1972 (1974).

Newton, T.W., J.M. Davidson, H.R. Hooper, P.W. Green, D.M. Sheppard and G.C. Neilson, 3$^-$ Octupole States in the Even Cd Nuclei, Phys. Rev. C 15, 630 (1977).

Nishimura, K., Gamma Rays from Inelastic Scattering of Neutrons by Fe, Cu, Zn, Ge, and Se, Jour. Phys. Soc. Jap. 16, 355 (1961).

Nishimura, K., K. Okano and S. Kikuchi, Studies of Excitation Cross Sections of (n,n'γ) Reactions, Nucl. Phys. 70, 421 (1965).

Patnode, T.A., General Graphics Program DIST, Univ. of N.H., unpublished, (1978).

Perey, C.M. and F.G. Perey, Compilation of Phenomenological Optical-Model Parameters, Atomic Data and Nuclear Data Tables 17, 1 (1976).

Raman, S., R.L. Auble and F.F. Dyer, Weak Gamma Transitions in 129-Day ^{123}Sn Decay, Phys. Rev. C 9, 426 (1974).

Ristinen, R.A., C. Chasman, and K.W. Jones, Charged Particle and γ-Ray Spectra from Fast Neutron Bombardment of a Lithium-Drifted Germanium γ-Ray Detector, Bull. Am. Phys. Soc. 10, 36 (1965).

Rose, H.J. and D.M. Brink, Angular Distributions of Gamma Rays in Terms of Phase-Defined Reduced Matrix Elements, Rev. Mod. Phys. 39, 306 (1967).

Satchler, G.R., The Angular Correlation of Three Nuclear Radiations, Phys. Rev. 94, 1304 (1954).

Satchler, G.R., Angular Distribution of Nuclear Reaction Products, Phys. Rev. 164, 1198 (1956).

Seagrave, J.D., D(d,n)^{3}He and T(d,n)^{4}He Neutron Source Handbook, Los Alamos Scientific Laboratory, Los Alamos, N.M., LAMS-2162 (1957).

Sen Gupta, A.K. and D.M. Van Patter, Studies of the Low-Lying Energy Levels of Zn^{64} and Zn^{66} From Measurements of (p,p'gamma) Radiations, Nucl. Phys. 50, 17 (1964).

Sheldon, Eric, Angular Correlation in Inelastic Nucleon Scattering, Rev. Mod. Phys. 35, 795 (1963).

Sheldon, E., Angular Correlation Functions for Compound Inelastic Nucleon Scattering, Phys. Rev. 133, B732 (1964).

Sheldon, Eric and Douglas M. Van Patter, Compound Inelastic Nucleon and Gamma-Ray Angular Distributions for Even- and Odd- Mass Nuclei, Rev. Mod. Phys. 38, 143 (1966).

Sheldon, E. and P. Gantenbein, Computation of Total, Differential and Double-Differential Cross Sections for Compound Nuclear Reactions of the Type (a,bγ) and (a,bγ-γ), ZAMP 18, 397 (1967).

Sheldon, Eric and Richard Michael Strang, Computation of Total, Differential and Double-Differential Cross Sections for Compound Nuclear Reactions of the type (a,b), (a,bγ) and (a,bγ-γ) (II) Generalized Programs "Mandy" and "Barbara" for Arbitrary Angular Momenta in Hauser-Feshbach-Moldaur Formalism, Comp. Phys. Comm. 1, 35 (1969).

Sheldon, Eric, S. Mathur, D.Donati, Computation of Total, Differential and Double-Differential Cross Sections for Compound Nuclear Reactions of the Type (a,b), (a,bγ), and (a,bγ-γ). (III) Fortran Translations of the Algol programs 'Mandy' and 'Barbara', Comp. Phys. Comm. 2, 272 (1971).

Sheldon, E. and V.C. Rogers, Computation of Total and Differential Cross Sections for Compound Nuclear Reactions of the Type (a,a), (a,a'), (a,b), (a,γ), (a,γ-γ), (a,bγ) and (a,bγ-γ). (IV) Fortran program 'CINDY', Comp. Phys. Comm. 6, 99 (1973).

Smith, William R., Nuclear Penetrability and Phase Shift Subroutine, Comp. Phys. Comm. 1, 106 (1969).

Tessler,G., and S.S. Glickstein, Search for the 2.37-MeV Gamma Ray From the ^{94}Zr(n,n'gamma) Reaction, Phys. Rev. C 6, 1430 (1972).

Van Loef, J.J. and D.A. Lind, Measurements of Inelastic Scattering Cross Sections for Fast Neutrons, Phys. Rev. 101, 103 (1956).

Vanden Berghe, G. and E. Degrieck, The Two Particle One Hole States in the Odd-A Antimony Isotopes, Z. Physik 262, 25 (1973).

Vanden Berghe, G., and K. Heyde, Structure and Electromagnetic Properties of the Odd-A Antimony Isotopes in a Unified-Model Calculation, Nucl. Phys. A163, 478 (1971).

Wilmore, D. and P.E. Hodgson, The Calculation of Neutron Cross Sections from Optical Potentials, Nucl. Phys. 55, 673 (1964).

Wolfenstein, L., Conservation of Angular Momentum in the Statistical Theory of Nuclear Reactions, Phys. Rev. 82, 690 (1951).

Zijp, E., Polarization Measurements and Optical Model Analysis of Neutron Scattering at 3.2 MeV, University of Amsterdam, Netherlands (1972).

APPENDIX A

(n,n'gamma) Reaction Kinematics

The kinematics of the (n,n'gamma) reaction will be discussed with reference to Figure A-1 which indicates the notation adopted here. Of particular interest is the relation between the lab gamma emission angle, θ_2, and the center-of-mass (CM) gamma emission angle, θ'_2.

The (n,n'gamma) reaction can be viewed as a two step process for kinematic purposes. A neutron scatters off of the target nucleus, exciting it, and causing it to recoil with energy E_4. Then approximately 10^{-12} seconds later the recoil nucleus decays and emits a gamma ray which again causes recoil of the residual nucleus with energy E_r. First we calculate the recoil energy E_4 and various other kinematic parameters of interest as a function of θ_1, the lab scattered nucleon angle. Then we examine the effect of recoil energy E_r on the gamma emission angle θ_2. Finally the relation between θ_2 and θ'_2 is discussed.

In order to implement calculation of the kinematic parameters relevant to the first step of this reaction, a Fortran program, REAKIN, was written (Marden, 1978). The kinematic formulae used were those of Marmier and Sheldon, (Marmier and Sheldon p 613, 1970). REAKIN will calculate the nonrelativistic kinematic parameters of interest for any

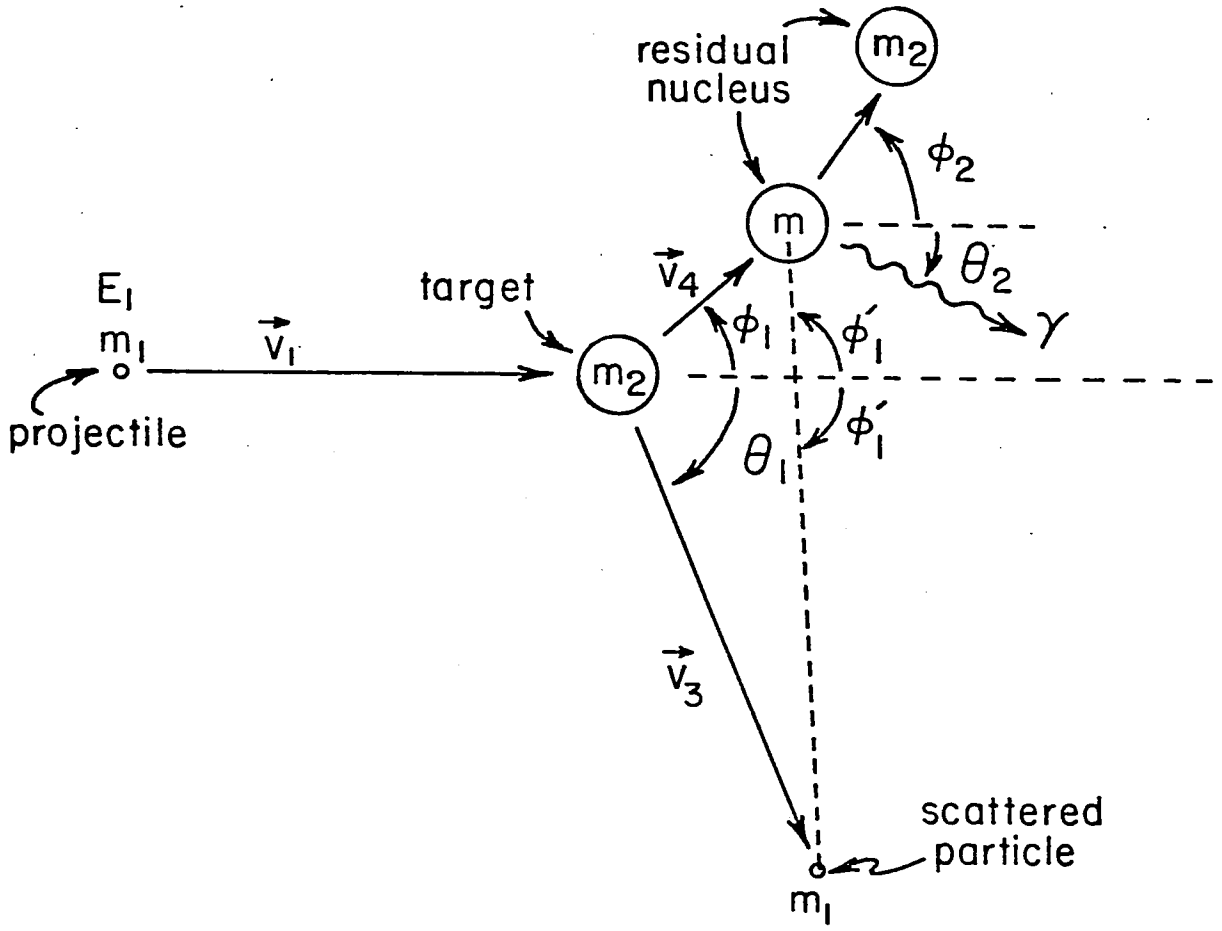
residual
nucleus
m_2
ϕ_2
m
θ_2
γ
E_1
m_1
$\vec{v}_1$
projectile
target
m_2
$\vec{v}_4$
ϕ_1
ϕ_1'
θ_1
ϕ_1'
$\vec{v}_3$
scattered
particle
m_1

FIGURE A-1

single step reaction of the form

$$m_1 + m_2 \rightarrow m_3 + m_4 + Q$$

which includes elastic and inelastic scattering. For inelastic scattering $m_1 = m_3$, $m_2 = m_4$, and $Q = -E^*$ where E^* is the excitation energy of the residual nucleus. This program has been run for the (n,n'gamma) reaction with ^{56}Fe, ^{121}Sb, and ^{123}Sb targets. REAKIN prints all input masses and energies, followed by the center-of-mass system angles and energies. The maximum values of the lab angles θ_1 and ϕ_1 are also given. Finally, a table of various parameters as functions of θ_1 is printed. Output from these runs appears in Tables A-1 through A-3. Note that the lab scattering angle θ_1 is approximately equal to the center-of-mass scattering angle θ_1'.

The next phase of the (n,n'gamma) reaction is the de-excitation of the recoiling nucleus. The gamma is emitted at a lab angle θ_2 and the nucleus recoils again at a lab angle of ϕ_2. Because the residual nucleus is so massive, very little momentum is given to it by the decay and the recoil energy, E_r is small. Most of the de-excitation energy is carried off by the gamma ray. Specifically, the recoil energy is given approximately by

$$E_r \sim (E^*)^2 / (2 m_2 c^2)$$

where E^* is the excitation energy of the nucleus and m_2 is the mass of the nucleus. For ^{56}Fe decaying by gamma

emission the recoil energy is $E_r \sim 8$ eV. Therefore, the nuclear recoil is negligible and the recoil angle $\phi_2 \sim 0$. This means that the assumption made in Chapter II, that $\theta_1 \sim \theta_1'$, is valid.

Table A-1

Reaction Kinematic Output for ^{56}Fe

(MASS IN AMU, ENERGY IN MEV, AND VELOCITY IN CM/SEC)

PROJECTILE MASS = 1.00 EMITTED PARTICLE MASS = 1.00
TARGET MASS = 56.00 RESIDUAL NUCLEUS MASS = 56.00

PROJECTILE KINETIC ENERGY = 3.00
PROJECTILE INCIDENT VELOCITY = 2.41E+09

Q-VALUE = -0.8470

LAB VELOCITY OF THE CENTER OF MASS = 4.22E+07

MAXIMUM THETA = 180.00
MAXIMUM PHI = 57.58

CM KINETIC ENERGY OF EMITTED PARTICLE = 2.0635
CM KINETIC ENERGY OF RESIDUAL NUCLEUS = 0.0368

CM VELOCITY OF EMITTED PARTICLE = 2.00E+09
CM VELOCITY OF RESIDUAL NUCLEUS = 3.56E+07

θ_1	E_3	ϕ_1	E_4	θ_1'	ϕ_1'	V_3	V_4
0	2.15	0.00	0.001	0.00	180.00	2.04E+09	6.58E+06
10	2.15	41.49	0.003	10.21	169.79	2.04E+09	9.54E+06
20	2.15	54.65	0.007	20.41	159.59	2.04E+09	1.52E+07
30	2.14	57.54	0.013	30.61	149.39	2.03E+09	2.15E+07
40	2.13	56.80	0.022	40.78	139.22	2.03E+09	2.78E+07
50	2.12	54.47	0.034	50.93	129.07	2.02E+09	3.40E+07
60	2.11	51.32	0.046	61.05	118.95	2.02E+09	4.00E+07
70	2.09	47.69	0.060	71.14	108.86	2.01E+09	4.56E+07
80	2.08	43.77	0.075	81.19	98.81	2.00E+09	5.09E+07
90	2.06	39.66	0.090	91.21	88.79	2.00E+09	5.58E+07
100	2.05	35.43	0.106	101.19	78.81	1.99E+09	6.03E+07
110	2.03	31.12	0.120	111.14	68.86	1.98E+09	6.43E+07
120	2.02	26.74	0.134	121.05	58.95	1.97E+09	6.79E+07
130	2.01	22.33	0.146	130.93	49.07	1.97E+09	7.09E+07
140	2.00	17.89	0.156	140.78	39.22	1.96E+09	7.34E+07
150	1.99	13.43	0.165	150.61	29.39	1.96E+09	7.53E+07
160	1.98	8.96	0.171	160.41	19.59	1.96E+09	7.67E+07
170	1.98	4.48	0.175	170.21	9.79	1.95E+09	7.76E+07
180	1.98	0.00	0.176	180.00	0.00	1.95E+09	7.79E+07

Table A-2

Reaction Kinematic Output for ^{121}Sb

(MASS IN AMU, ENERGY IN MEV, AND VELOCITY IN CM/SEC)

PROJECTILE MASS = 1.00 EMITTED PARTICLE MASS = 1.00
TARGET MASS = 121.00 RESIDUAL NUCLEUS MASS =121.00

PROJECTILE KINETIC ENERGY = 3.00
PROJECTILE INCIDENT VELOCITY = 2.41E+09

Q-VALUE = -1.0360

LAB VELOCITY OF THE CENTER OF MASS = 1.97E+07

MAXIMUM THETA = 180.00
MAXIMUM PHI = 53.84

CM KINETIC ENERGY OF EMITTED PARTICLE = 1.9235
CM KINETIC ENERGY OF RESIDUAL NUCLEUS = 0.0159

CM VELOCITY OF EMITTED PARTICLE = 1.93E+09
CM VELOCITY OF RESIDUAL NUCLEUS = 1.59E+07

θ_1	E_3	ϕ_1	E_4	θ_1'	ϕ_1'	V_3	V_4
0	1.96	0.00	0.001	0.00	180.00	1.95E+09	3.80E+06
10	1.96	34.61	0.002	10.10	169.90	1.95E+09	4.92E+06
20	1.96	49.00	0.003	20.20	159.80	1.95E+09	7.29E+06
30	1.96	53.36	0.006	30.29	149.71	1.94E+09	1.00E+07
40	1.95	53.65	0.010	40.38	139.62	1.94E+09	1.28E+07
50	1.95	52.03	0.015	50.45	129.55	1.94E+09	1.56E+07
60	1.94	49.39	0.021	60.51	119.49	1.94E+09	1.83E+07
70	1.94	46.16	0.027	70.55	109.45	1.93E+09	2.08E+07
80	1.93	42.54	0.034	80.58	99.42	1.93E+09	2.32E+07
90	1.92	38.68	0.041	90.59	89.41	1.93E+09	2.55E+07
100	1.92	34.65	0.048	100.58	79.42	1.92E+09	2.75E+07
110	1.91	30.50	0.054	110.55	69.45	1.92E+09	2.94E+07
120	1.90	26.26	0.060	120.51	59.49	1.92E+09	3.10E+07
130	1.90	21.96	0.066	130.45	49.55	1.91E+09	3.24E+07
140	1.89	17.61	0.071	140.38	39.62	1.91E+09	3.36E+07
150	1.89	13.23	0.074	150.29	29.71	1.91E+09	3.45E+07
160	1.89	8.83	0.077	160.20	19.80	1.91E+09	3.51E+07
170	1.88	4.42	0.079	170.10	9.90	1.91E+09	3.55E+07
180	1.88	0.00	0.080	180.00	0.00	1.91E+09	3.57E+07

Table A-3

Reaction Kinematic Output for ^{123}Sb

(MASS IN AMU, ENERGY IN MEV, AND VELOCITY IN CM/SEC)

PROJECTILE MASS = 1.00 EMITTED PARTICLE MASS = 1.00
TARGET MASS = 123.00 RESIDUAL NUCLEUS MASS =123.00

PROJECTILE KINETIC ENERGY = 3.00
PROJECTILE INCIDENT VELOCITY = 2.41E+09

Q-VALUE = -1.0890

LAB VELOCITY OF THE CENTER OF MASS = 1.94E+07

MAXIMUM THETA = 180.00
MAXIMUM PHI = 52.78

CM KINETIC ENERGY OF EMITTED PARTICLE = 1.8716
CM KINETIC ENERGY OF RESIDUAL NUCLEUS = 0.0152

CM VELOCITY OF EMITTED PARTICLE = 1.90E+09
CM VELOCITY OF RESIDUAL NUCLEUS = 1.55E+07

θ_1	E_3	ϕ_1	E_4	θ_1'	ϕ_1'	V_3	V_4
0	1.91	0.00	0.001	0.00	180.00	1.92E+09	3.95E+06
10	1.91	32.88	0.002	10.10	169.90	1.92E+09	4.99E+06
20	1.91	47.41	0.003	20.20	159.80	1.92E+09	7.25E+06
30	1.90	52.12	0.006	30.29	149.71	1.92E+09	9.88E+06
40	1.90	52.67	0.010	40.38	139.62	1.92E+09	1.26E+07
50	1.90	51.24	0.015	50.45	129.55	1.91E+09	1.53E+07
60	1.89	48.74	0.020	60.51	119.49	1.91E+09	1.79E+07
70	1.88	45.62	0.026	70.55	109.45	1.91E+09	2.04E+07
80	1.88	42.09	0.033	80.58	99.42	1.90E+09	2.27E+07
90	1.87	38.30	0.040	90.59	89.41	1.90E+09	2.49E+07
100	1.86	34.33	0.046	100.58	79.42	1.90E+09	2.69E+07
110	1.86	30.23	0.053	110.55	69.45	1.89E+09	2.87E+07
120	1.85	26.04	0.059	120.51	59.49	1.89E+09	3.03E+07
130	1.85	21.78	0.064	130.45	49.55	1.89E+09	3.17E+07
140	1.84	17.47	0.069	140.38	39.62	1.89E+09	3.28E+07
150	1.84	13.13	0.072	150.29	29.71	1.88E+09	3.37E+07
160	1.84	8.77	0.075	160.20	19.80	1.88E+09	3.44E+07
170	1.83	4.39	0.077	170.10	9.90	1.88E+09	3.47E+07
180	1.83	0.00	0.077	180.00	0.00	1.88E+09	3.49E+07

APPENDIX B

Transmission Coefficients

To illustrate the meaning of the transmission coefficients referred to in Chapter II, consider first the case of a particle penetrating a potential barrier. For simplicity we represent the potential as a rectangular barrier in one-dimension as shown in Figure B-1. Define three regions in Figure B-1 as follows

Region 1	$V = 0$	$-\infty < x < 0$
Region 2	$V = U$	$0 \leq x \leq b$
Region 3	$V = 0$	$b < x < \infty$

A classical particle of energy $E < U$ incident on the left side of the barrier cannot penetrate, however, quantum mechanically the particle can penetrate the barrier. This penetrating ability is described through the use of the transmission coefficients.

The solutions to Schrödinger's equation in Region 1 and Region 2 are linear combinations of incident and reflected wave functions. In Region 3 the solution is a transmitted wave traveling toward increasing z. The wave amplitude $A^{(+)}$ and $A^{(-)}$ represent the incident and reflected particles on the left side of the barrier (Region 1) while $B^{(+)}$ and $B^{(-)}$ are the wave amplitudes inside of the barrier

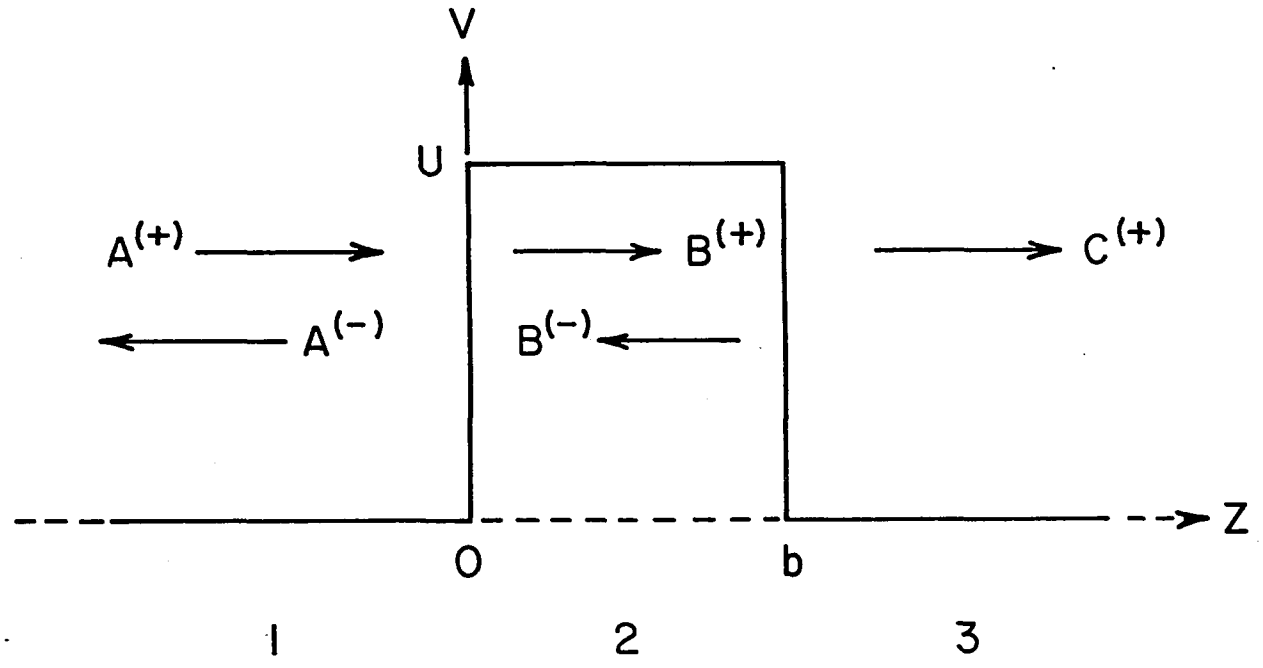

FIGURE B-1

(Region 2). To the right of the barrier (Region 3), $C^{(+)}$ represents the transmitted wave amplitude. We now define the transmission coefficients in terms of fluxes as follows. A flux is equal to the probability current times the wave number k where the wave number $k = (2mE/\hbar^2)^{1/2}$ is proportional to velocity. Then the transmission coefficient T is

$$T = \text{Emergent Flux/Incident Flux} = |C^{(+)}|^2 \, k_3 / |A^{(+)}|^2 \, k_1$$

In general, the coefficients A, B, and C are found by solving the Schrödinger equation in the three regions seperately and matching the solutions at the boundaries.

For a nuclear potential barrier, the potential is a three-dimensional spherically symmetric barrier. Radial symmetry permits us to separate variables and express solutions as functions of each variable

$$\Psi(r) = f(r)\,\Theta(0)\,\Phi(o)$$

where f, Θ, and Φ are the solutions to the radial and two angular equations respectively. The angular solutions are the spherical harmonics $Y_{lm}(\theta,\phi)$. It is the radial equation that is of interest in calculating the transmission coefficients since the nuclear potential is a function of the radial coordinate, r. The radial equation can be written in modified form

$$d^2u/dr^2 + (2m/\hbar^2)[E - V(r) - \{l(l+1)\hbar^2/2mr^2\}]u = 0$$

where $u(r) = r\,f(r)$ Since the solutions of this equation, the $u_\ell(r)$, are dependent on l, the resulting coefficient T_ℓ will be l dependent. The transmission coefficient can also be dependent on j when a spin-orbit term is added to the potential $V(r)$ resulting in the $T_{j\ell}$ used in calculating the differential cross section in Chapter II. In determining the $T_{j\ell}$, solution of the radial wave equation is generally carried out for each j and l with a potential $V(r)$ by applying numerical methods through the use of a program such as SCAT described in Appendix C.

APPENDIX C

Program SCAT

The Fortran program SCAT numerically integrates the radial Schrödinger equation and determines the transmission coefficients, T_{jl}, required by MANDYF (see Appendix D) to evaluate compound nucleus reactions (Smith, 1969). SCAT uses an optical model potential that includes a Coulomb term, a complex Woods-Saxon nuclear potential, and spin-orbit coupling.

Briefly, the technique employed by SCAT consists of stepping out a solution, starting with zero at the origin, to a point beyond the nuclear potential where the solution is matched at two radii, R_b and $R_b + \delta$, to a linear combination of regular and irregular asymptotic Coulomb wave functions. Of course when neutron scattering is being considered these wave functions reduce to regular and irregular spherical Bessel functions. The boundary matching coefficients β are determined and the T_{jl} derived from them as follows

$$T_{jl} = 1 - |1 - 2\beta_{jl}|^2$$

The interior radial wave equation is

$$d^2f(r)/dr^2 + \{k^2 + 2mV(r)/\hbar^2 - l(l + 1)/r^2\}f(r) = 0$$

where the potential consists of three terms. The Coulomb term V_c is simply that due to a homogenously charged sphere. The second term is the complex Woods-Saxon nuclear term V_N with the general form

$$Vf_{ws}(r,R,a) + iW[(1-t)f_{ws}(r,R',ca' + tf_s(r,R',a')]$$

where V, W, R, a, R', and a' are constants of the potential. The factor f_{ws} is a Woods-Saxon form

$$f_{ws}(r,R,a) = [1 + \exp\{(r-R)/a\}]^{-1}$$

and f_s is a surface peaked derivative term

$$f_s = -4a' \, df_{ws}(r,R',a')/dr$$

and t is the fraction of the surface peaked contribution and has values from 0 to 1. The last term in V(r) is the spin-orbit term V'_{so}

$$V'_{so} = \langle \vec{l} \cdot \vec{s} \rangle \, V_{so} \, (2/r) \, df_{ws}/dr$$

where V_{so} is a constant. Since $\vec{j} = \vec{l} + \vec{s}$, we can write

$$\langle \vec{l} \cdot \vec{s} \rangle = [j(j+1) - l(l+1) - s(s+1)]/2$$

The essential input parameters to SCAT are the values of R, a, R', a', V, W, V_{so} in the potential V(r). The parameters used in this experiment were those of Wilmore and Hodgson, (1964)

$$R = 1.322 - (7.6 \times 10^{-4})A + (4 \times 10^{-5})A^2 \text{ fm}$$

$$a = 0.66 \text{ fm}$$

$$R' = 1.266 - (3.7 \times 10^{-4})A + (4 \times 10^{-6})A^2 \text{ fm}$$

$$a' = 0.48 \text{ fm}$$

$$V = 47.01 - 0.267E_n - 0.0018E_n^2 \text{ MeV}$$

$$W = 9.52 - 0.053E_n \text{ MeV}$$

$$V = 7.0 \text{ MeV}$$

$$t = 1.0$$

Where E_n is the incoming neutron energy and A is the target mass number. These parameters were derived from fits of the potential V(r) to neutron elastic scattering data. Other input parameters are the projectile energy, masses of target and projectile, projectile spin, product of target and projectile charge, and maximum partial wave to be calculated.

APPENDIX D

Program MANDYF

The Fortran program MANDYF evaluates total cross sections, differential cross sections, and angular distribution for reactions of the type (a,b), (a,b gamma), and (a,b gamma-gamma) according to a statistical compound nucleus theory (Sheldon and Donati, 1971). Partial waves up to l_{max}= 8 can be included with up to 40 extra exit channels considered.

As an example, details of the calculation for the (n,n'gamma) reaction will be presented here. For more information on this and the other reactions, see the references by Sheldon. The differential cross section for the (n,n',gamma) reaction is given by

$$d\sigma/d\Omega = \frac{\lambda^2}{4}\sum g\, \eta_\nu(j_1 j_1 J_0 J_1)\; U_\nu(j_2 j_2 J_2 J_1) \times A_\nu(L_2 L_2' J_3 J_2)\; \tau\; P_\nu(\cos\theta_2)$$

where $0 \le \nu \le 2j_1, 2J_1, 2J_2, 2L_2'$. This can be rewritten as follows

$$d\sigma/d\Omega = \frac{\lambda^2}{8}\sum N'C'W'\, M(\delta)\, \tau\, P_\nu(\cos\theta_2)$$

where

$$N' = (-)^{J_0+J_3-j_2+1/2}(J_1)^4 (j_1)^2 (J_2)^2/(J_0)^2$$

$$C' = \langle \nu 0 | j_1 j_1 1/2 \; -1/2 \rangle$$

$$W' = W(J_1 J_1 j_1 j_1 ; \nu J_0) \; W(J_1 J_1 J_2 J_2 ; \nu j_2)$$

$$M(\delta) = (1+\delta^2)^{-1}[M(LL) + 2\delta M(LL') + \delta^2 M(L'L')]$$

and

$$M(LL') = LL' \langle \nu 0 | LL' 1 \; -1 \rangle \; W(J_2 J_1 LL' ; \nu J_3)$$

Thus we see that evaluation of the differential cross section requires calculation of Clebsch-Gordon and Racah coefficients for given J_0, j_1, J_1, j_2, J_2, L, L' and J_3. These coefficients are calculated and then summed if the angular momenta relations discussed below are satisfied and ν is within its restriction.

The sequence followed by MANDYF in evaluating a differential cross section is as follows. The program first chooses $l_1 = 0$ and $j_1 = l_1 - 1/2$. From conservation of angular momentum in a compound nucleus reaction we have

$$\vec{J}_0 + \vec{j}_1 = \vec{J}_1$$

which leads to a restriction on J_1 as follows

$$|J_0 - j_1| \leq J_1 \leq J_0 + j_1$$

Thus the lowest $J_1 = |J_0 - j_1|$ is chosen with $\pi_1 = (-)^{l_1} \pi_0$. Parity conservation requires that $l_1 + l_2$ be even (odd) if $\pi_0 = \pi_2$ ($\pi_0 \neq \pi_2$) so l_2 is first set at zero and the parity condition is tested. If it is not met l_2 is set to 1. Then we set $j_2 = l_2 - 1/2$ and test j_2 with the angular momentum conservation relation

$$\vec{J}_1 = \vec{J}_2 + \vec{j}_2$$

using

$$|J_2 - J_1| \leq j_1 \leq J_2 + J_1$$

If j_2 satisfies this relation the computation procedes by evaluating the Clebsch-Gordon and Racah coefficients for any ν satisfying $0 \leq \nu \leq 2j_1, 2J_1, 2J_2, 2L'$. Then the sums in τ are performed and the contribution added to the differential cross section. Next $j_2 = l_2 + 1/2$ is tested and the process repeated if the test is satisfied. Then l_2 is increased by two and $j_2 = l_2 - 1/2$ and so on until $l_2 \leq l_{2max}$ is not satisfied. Following that, J_1 is raised by 1 and tested to insure that $J_1 \leq J_0 + j_1$ and the process repeated again. Then j_1 is set to $j_1 = l_1 + 1/2$ and the calculation repeated once more. Finally, l_1 is increased by 1 with $l_1 \leq l_{1max}$ and the entire cycle repeated. The calculation terminates when all possible combinations satisfying $l_1 = l_{1max}$ have been completed.

To illustrate the procedure followed by MANDYF explicitly, consider the ^{56}Fe(n,n'gamma)^{56}Fe reaction. A printout of the angular momenta involved in the terms kept by MANDYF is presented in Table D-1. For this reaction note that $J_0 = 0$, $\pi_0 = +$, $J_2 = 2$, $\pi_2 = +$, $J_3 = 0$, $\pi_3 = +$, and $L = L' = 2$. The calculation begins with $l_1 = 0$ and $j_1 = l_1 + 1/2 = 1/2$ since $j_1 = l_1 - 1/2 < 0$. Then $J_1 = J_0 - j_1 = 1/2$ and $\pi_1 = +$ as a result of $\pi_1 = (-)^{l_1}\pi_0$. l_2 is first set at zero and is valid since $\pi_0 = \pi_2 = +$ and $l_1 + l_2 = 0$ is even. This means that $j_2 = l_2 + 1/2 = 1/2$,

again because $j_2 = l_2 - 1/2 < 0$. Finally MANDYF tests j_2 by

$$|J_1 - J_2| \leq j_2 \leq J_1 + J_2$$
$$3/2 \leq j_2 \leq 5/2$$

which is not fulfilled. Next l_2 is set to 2 so $j_2 = l_2 - 1/2 = 3/2$ and the condition

$$3/2 \leq j_2 \leq 5/2$$

is fulfilled. Only a $\nu = 0$ is tabulated for these parameters since $j_1 = 1/2$ and we require $0 \leq \nu \leq 2j_1, 2J_1, 2J_2, 2L'$. As shown in Table D-1, the tabulation continues until all terms with $l_1 = l_{1max}$ and $l_2 = l_{2max}$ have been computed at which point the calculation is complete. MANDYF outputs the total cross section, differential cross section, and normalizes the differential cross section to 1.0 at 90° to arrive at the angular distribution. MANDYF then cycles back for additional input data and repeats its calculations.

Table D-1

Angular Momentum Tabulation from Program MANDYF

l_1	j_1	J_1	l_2	j_2	ν	τ	N' C' W'	a_y
0.	0.5	0.5	2.	1.5	0	.2918E+00	-.2236E+01	.1000E+01
0.	0.5	0.5	2.	2.5	0	.2012E+00	-.2236E+01	.1000E+01
1.	0.5	-0.5	1.	1.5	0	.2374E+00	-.2236E+01	.1000E+01
1.	0.5	-0.5	3.	2.5	0	.2176E-01	-.2236E+01	.1000E+01
1.	1.5	-1.5	1.	0.5	0	.1469E+00	-.4472E+01	.2000E+01
1.	1.5	-1.5	1.	0.5	2	.1469E+00	.3742E+01	.1000E+01
1.	1.5	-1.5	1.	1.5	0	.1663E+00	-.4472E+01	.2000E+01
1.	1.5	-1.5	1.	1.5	2	.1663E+00	.0000E+00	.0000E+00
1.	1.5	-1.5	3.	2.5	0	.1525E-01	-.4472E+01	.2000E+01
1.	1.5	-1.5	3.	2.5	2	.1525E-01	-.2673E+01	-.7143E+00
1.	1.5	-1.5	3.	3.5	0	.3193E-01	-.4472E+01	.2000E+01
1.	1.5	-1.5	3.	3.5	2	.3193E-01	.1069E+01	.2857E+00
2.	1.5	1.5	0.	0.5	0	.1813E+00	-.4472E+01	.2000E+01
2.	1.5	1.5	0.	0.5	2	.1813E+00	.3742E+01	.1000E+01
2.	1.5	1.5	2.	1.5	0	.1590E+00	-.4472E+01	.2000E+01
2.	1.5	1.5	2.	1.5	2	.1590E+00	.0000E+00	.0000E+00
2.	1.5	1.5	2.	2.5	0	.1096E+00	-.4472E+01	.2000E+01
2.	1.5	1.5	2.	2.5	2	.1096E+00	-.2673E+01	-.7143E+00
2.	1.5	1.5	4.	3.5	0	.2085E-02	-.4472E+01	.2000E+01
2.	1.5	1.5	4.	3.5	2	.2085E-02	.1069E+01	.2857E+00
2.	2.5	2.5	0.	0.5	0	.1293E+00	-.6708E+01	.3000E+01
2.	2.5	2.5	0.	0.5	2	.1293E+00	.6414E+01	.1714E+01
2.	2.5	2.5	0.	0.5	4	.1293E+00	-.3586E+01	-.1714E+01
2.	2.5	2.5	2.	1.5	0	.1134E+00	-.6708E+01	.3000E+01
2.	2.5	2.5	2.	1.5	2	.1134E+00	.2291E+01	.6122E+00
2.	2.5	2.5	2.	1.5	4	.1134E+00	.4098E+01	.1959E+01
2.	2.5	2.5	2.	2.5	0	.7821E-01	-.6708E+01	.3000E+01
2.	2.5	2.5	2.	2.5	2	.7821E-01	-.2291E+01	-.6122E+00
2.	2.5	2.5	2.	2.5	4	.7821E-01	-.2305E+01	-.1102E+01
2.	2.5	2.5	4.	3.5	0	.1487E-02	-.6708E+01	.3000E+01
2.	2.5	2.5	4.	3.5	2	.1487E-02	-.3894E+01	-.1041E+01
2.	2.5	2.5	4.	3.5	4	.1487E-02	.6830E+00	.3265E+00
2.	2.5	2.5	4.	4.5	0	.1057E-02	-.6708E+01	.3000E+01
2.	2.5	2.5	4.	4.5	2	.1057E-02	.2291E+01	.6122E+00
2.	2.5	2.5	4.	4.5	4	.1057E-02	-.8537E-01	-.4082E-01
3.	2.5	-2.5	1.	0.5	0	.3373E-01	-.6708E+01	.3000E+01
3.	2.5	-2.5	1.	0.5	2	.3373E-01	.6414E+01	.1714E+01
3.	2.5	-2.5	1.	0.5	4	.3373E-01	-.3586E+01	-.1714E+01
3.	2.5	-2.5	1.	1.5	0	.3820E-01	-.6708E+01	.3000E+01
3.	2.5	-2.5	1.	1.5	2	.3820E-01	.2291E+01	.6122E+00

3.	2.5-2.5	1. 1.5	4	.3820E-01	.4098E+01	.1959E+01
3.	2.5-2.5	3. 2.5	0	.3502E-02	-.6708E+01	.3000E+01
3.	2.5-2.5	3. 2.5	2	.3502E-02	-.2291E+01	-.6122E+00
3.	2.5-2.5	3. 2.5	4	.3502E-02	-.2305E+01	-.1102E+01
3.	2.5-2.5	3. 3.5	0	.7334E-02	-.6708E+01	.3000E+01
3.	2.5-2.5	3. 3.5	2	.7334E-02	-.3894E+01	-.1041E+01
3.	2.5-2.5	3. 3.5	4	.7334E-02	.6830E+00	.3265E+00
3.	2.5-2.5	5. 4.5	0	.1035E-04	-.6708E+01	.3000E+01
3.	2.5-2.5	5. 4.5	2	.1035E-04	.2291E+01	.6122E+00
3.	2.5-2.5	5. 4.5	4	.1035E-04	-.8537E-01	-.4082E-01
3.	3.5-3.5	1. 1.5	0	.9300E-01	-.8944E+01	.4000E+01
3.	3.5-3.5	1. 1.5	2	.9300E-01	.7636E+01	.2041E+01
3.	3.5-3.5	1. 1.5	4	.9300E-01	-.3073E+01	-.1469E+01
3.	3.5-3.5	3. 2.5	0	.8527E-02	-.8944E+01	.4000E+01
3.	3.5-3.5	3. 2.5	2	.8527E-02	.1273E+01	.3401E+00
3.	3.5-3.5	3. 2.5	4	.8527E-02	.5464E+01	.2612E+01
3.	3.5-3.5	3. 3.5	0	.1786E-01	-.8944E+01	.4000E+01
3.	3.5-3.5	3. 3.5	2	.1786E-01	-.4073E+01	-.1088E+01
3.	3.5-3.5	3. 3.5	4	.1786E-01	-.4098E+01	-.1959E+01
3.	3.5-3.5	5. 4.5	0	.2520E-04	-.8944E+01	.4000E+01
3.	3.5-3.5	5. 4.5	2	.2520E-04	-.4836E+01	-.1293E+01
3.	3.5-3.5	5. 4.5	4	.2520E-04	.1490E+01	.7124E+00
3.	3.5-3.5	5. 5.5	0	.8113E-04	-.8944E+01	.4000E+01
3.	3.5-3.5	5. 5.5	2	.8113E-04	.3563E+01	.9524E+00
3.	3.5-3.5	5. 5.5	4	.8113E-04	-.2173E+00	-.1039E+00
4.	3.5 3.5	2. 1.5	0	.1063E-01	-.8944E+01	.4000E+01
4.	3.5 3.5	2. 1.5	2	.1063E-01	.7636E+01	.2041E+01
4.	3.5 3.5	2. 1.5	4	.1063E-01	-.3073E+01	-.1469E+01
4.	3.5 3.5	2. 2.5	0	.7329E-02	-.8944E+01	.4000E+01
4.	3.5 3.5	2. 2.5	2	.7329E-02	.1273E+01	.3401E+00
4.	3.5 3.5	2. 2.5	4	.7329E-02	.5464E+01	.2612E+01
4.	3.5 3.5	4. 3.5	0	.1394E-03	-.8944E+01	.4000E+01
4.	3.5 3.5	4. 3.5	2	.1394E-03	-.4073E+01	-.1088E+01
4.	3.5 3.5	4. 3.5	4	.1394E-03	-.4098E+01	-.1959E+01
4.	3.5 3.5	4. 4.5	0	.9901E-04	-.8944E+01	.4000E+01
4.	3.5 3.5	4. 4.5	2	.9901E-04	-.4836E+01	-.1293E+01
4.	3.5 3.5	4. 4.5	4	.9901E-04	.1490E+01	.7124E+00
4.	4.5 4.5	2. 2.5	0	.6602E-02	-.1118E+02	.5000E+01
4.	4.5 4.5	2. 2.5	2	.6602E-02	.8909E+01	.2381E+01
4.	4.5 4.5	2. 2.5	4	.6602E-02	-.2988E+01	-.1429E+01
4.	4.5 4.5	4. 3.5	0	.1256E-03	-.1118E+02	.5000E+01
4.	4.5 4.5	4. 3.5	2	.1256E-03	.4049E+00	.1082E+00
4.	4.5 4.5	4. 3.5	4	.1256E-03	.6519E+01	.3117E+01
4.	4.5 4.5	4. 4.5	0	.8920E-04	-.1118E+02	.5000E+01
4.	4.5 4.5	4. 4.5	2	.8920E-04	-.5669E+01	-.1515E+01
4.	4.5 4.5	4. 4.5	4	.8920E-04	-.5705E+01	-.2727E+01
5.	4.5-4.5	3. 2.5	0	.5643E-04	-.1118E+02	.5000E+01
5.	4.5-4.5	3. 2.5	2	.5643E-04	.8909E+01	.2381E+01
5.	4.5-4.5	3. 2.5	4	.5643E-04	-.2988E+01	-.1429E+01
5.	4.5-4.5	3. 3.5	0	.1182E-03	-.1118E+02	.5000E+01
5.	4.5-4.5	3. 3.5	2	.1182E-03	.4049E+00	.1082E+00

5.	4.5-4.5	3.	3.5	4	.1182E-03	.6519E+01	.3117E+01
5.	4.5-4.5	5.	4.5	0	.1668E-06	-.1118E+02	.5000E+01
5.	4.5-4.5	5.	4.5	2	.1668E-06	-.5669E+01	-.1515E+01
5.	4.5-4.5	5.	4.5	4	.1668E-06	-.5705E+01	-.2727E+01
5.	4.5-4.5	5.	5.5	0	.5369E-06	-.1118E+02	.5000E+01
5.	4.5-4.5	5.	5.5	2	.5369E-06	-.5669E+01	-.1515E+01
5.	4.5-4.5	5.	5.5	4	.5369E-06	.2340E+01	.1119E+01
5.	5.5-5.5	3.	3.5	0	.7096E-03	-.1342E+02	.6000E+01
5.	5.5-5.5	3.	3.5	2	.7096E-03	.1020E+02	.2727E+01
5.	5.5-5.5	3.	3.5	4	.7096E-03	-.3042E+01	-.1455E+01
5.	5.5-5.5	5.	4.5	0	.1002E-05	-.1342E+02	.6000E+01
5.	5.5-5.5	5.	4.5	2	.1002E-05	-.3925E+00	-.1049E+00
5.	5.5-5.5	5.	4.5	4	.1002E-05	.7489E+01	.3580E+01
5.	5.5-5.5	5.	5.5	0	.3224E-05	-.1342E+02	.6000E+01
5.	5.5-5.5	5.	5.5	2	.3224E-05	-.7177E+01	-.1918E+01
5.	5.5-5.5	5.	5.5	4	.3224E-05	-.7222E+01	-.3453E+01

APPENDIX E

Program EVA

The data analysis program, EVA, is a modified version of the program used by the Nuclear Research Centre's (n,n'gamma) research group in Alberta, Canada (Davidson, 1976). As discussed briefly in Chapter IV, EVA calculates the distortion of the theoretical gamma angular distribution caused by the following factors

- energy loss of the 300 keV deuteron in the TiD target affecting neutron energy through kinematics of the $d(d,n)^3He$ reaction
- neutron source angular distribution anisotropy including energy and yield anisotropies
- finite size of Ge(Li) detector
- finite area of the neutron source spot
- finite volume of the sample including the $1/r^2$ dependency of neutron flux
- error in the flight path length and angle to the Ge(Li) detector caused by reference of these quantities to the end face of the TiD target
- gamma and neutron attenuation in the sample

The geometry and notation used by EVA is shown in Figure E-1. A cylindrical coordinate system is used with

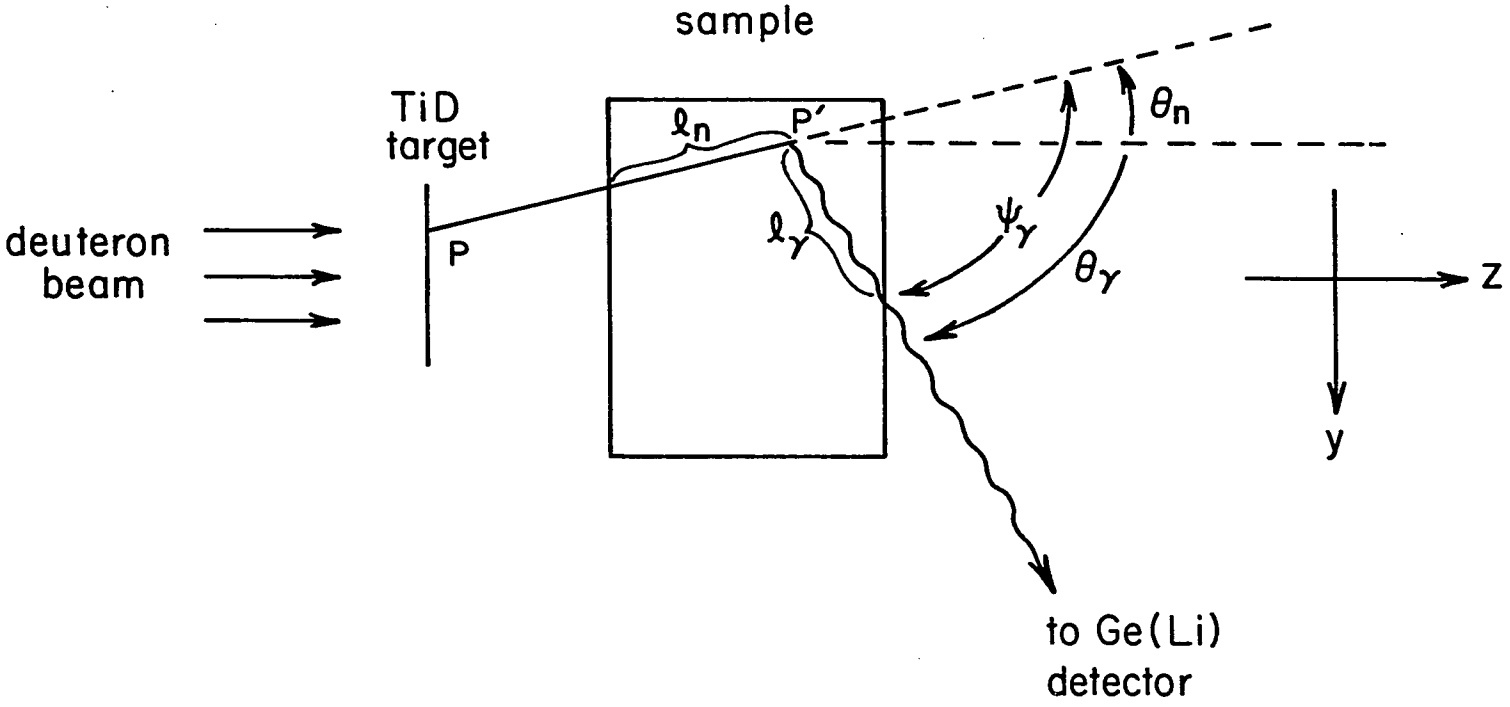
sample
TiD
target
ℓ_n
P'
θ_n
deuteron
beam
P
ℓ_γ
ψ_γ
θ_γ
z
y
to Ge(Li)
detector

FIGURE E-1

the $\hat{z}$ axis along the deuteron beam direction and the $\hat{x}$ axis in a vertical direction. A deuteron interacts with deuterium in the TiD target at a point P. This produces a neutron of energy E_n which exits the target, travels through the sample a distance l_n, and initiates an (n,n'gamma) reaction at a point P'. Thus the neutron path is established, making an angle θ_n with respect to the deuteron beam direction and an angle ϕ_n with respect to the vertical $\hat{x}$ axis. The length of this path is used to calculate a $1/r^2$ flux attenuation factor. The angle θ_n is used to determine neutron yield, discussed in more detail later, and energy, from reaction kinematics.

EVA then calculates the gamma flight path using the lab angles θ_γ and ϕ_γ of the Ge(Li) detector position relative to the beam axis. ϕ_γ is fixed, usually in the y-z plane at $\phi_\gamma = 90^0$ and θ_γ is chosen by the experimenter. The distance that the gamma travels through the sample, l_γ, is used to determine gamma attenuation and the flight path length is used to correct for variation in path length from different areas of the sample. Angular attenuation effects caused by finite Ge(Li) detector size are included in the form of the Q_ν coefficients calculated with a program developed by Krane, (1972).

Finally, EVA determines the angle Ψ_γ between the incident neutron path and the gamma. This is the gamma emission angle with respect to the alignment axis which is used to calculate the angular distribution using the series

$$W(\theta_\gamma) = 1 + B_2 c_2 P_2(\cos\theta_\gamma) + B_4 c_4 P_4(\cos\theta_\gamma)$$

where the B_ν are energy dependent terms containing all the information on the distribution except the mixing ratio dependence which is contained in the c_ν. The appropriate $B_\nu(E_n)$ is chosen by interpolating a table of $B_\nu(E_n)$ supplied by MANDYF (Sheldon and Donati, 1971). Since the c_ν are independent of experimental conditions, these terms are not included in the calculation until the numerical integration is complete.

When all energy, volume, and area increments have been included in the computation, EVA multiplies the distribution terms by the c_ν factors for a given δ and performs a least square fit of the distorted theoretical distribution to the experimental yields, varying the amplitude of the theoretical distribution. This fit is repeated over a range of δ and the best fit parameters printed. Output files are also created for later plotting.

The original version of EVA was written for use with the $^7Li(p,n)^7Be$ and $^3H(p,n)^3He$ neutron producing reactions and incorporated the neutron angular distributions of these reactions through the use of Legendre polynomial series expansion coefficients. The UNH version of EVA has been set up for use with the $d(d,n)^3He$ reaction and incorporates angular distribution information in the form of a table of yield values taken from Seagrave, (1957). A table lookup and interpolation procedure is written into EVA in the form of a subroutine ANGDIS.

The UNH version of EVA has also had flight path length and angle corrections included in it. This is because those quantities were referenced from the endface of the target holder. The use of an ~ 3 cm long sample and a 30 cm flight path without such a correction would introduce an appreciable systematic error. Also a subroutine to calculate confidence levels from the reduced χ^2 and degrees of freedom was added. In addition, EVA was originally written in Fortran II for an XDS 940 computer and required conversion to the UNH DECsystem10 computer. EVA must be run with access to a data file called ABD.DAT which contains the α, β and γ coefficients required to compute the c_ν in Green's formalism with the sign convention for δ of Rose and Brink (Green et al., 1972; Rose and Brink, 1967). Note that this sign convention is opposite to that used for δ in MANDYF.

Input data is entered into EVA from separate data files. All input data is in list directed (free field) format. A separate data file creation program, INEVA, is also available for data entry. The following is a list of some required data

- title of analysis run
- experimental angles, yields and errors
- mixing ratio limits and increment
- TiD target energy thickness and number of increments
- gamma and neutron linear attenuation coefficients

- sample dimensions and sample-target distance
- volume increment numbers
- reaction threshold energy
- deuteron energy
- beam spot radius and area increment numbers
- Q_y angular attenuation coefficients
- B_y coefficients for various energies
- initial and final level spins
- flight path length

For further details on file construction and operation of this program see the EVA documentation by Davidson.

APPENDIX F

Determination of Yield Statistics

It is the intent of this section to describe how the yield errors shown in the figures and used by EVA to calculate χ^2 are determined. Also we present some statistical data on the ^{56}Fe, ^{121}Sb and ^{123}Sb transitions discussed in Chapter IV.

The extraction of a yield, S, from the raw data requires determination of the background area, B, and the total peak area, N, where

$$S = N - B$$

Then the standard deviation in S is

$$\sigma_S = (\sigma_N^2 + \sigma_B^2)^{1/2}$$

The background is calculated from $B = l\,\bar{B}$ where l is the number of channels under the peak and $\bar{B}$ is the average background determined from contributions at both sides of the peak including a total of m channels and B' counts. Thus

$$\bar{B} = B'/m$$

Then

$$\sigma_{\bar{B}} = \sigma_{B'}/(m)^{1/2} = (B'/m)^{1/2} = (B)^{1/2}$$

Using the fact that $\sigma_N^2 = N$ and $\sigma_B^2 = 1\,\bar{B}$ we substitute into the equation for σ_S

$$\sigma_S = (N + 1\,\bar{B})^{1/2} = (S + 21\,\bar{B})^{1/2}$$

The above expression includes only a statistical contribution and does not take into account the human error involved in the peak extraction. It was found that for repeated data points the inclusion of statistical error only, resulted in yields which did not agree well with each other. Therefore, a 3% additional error was added in quadrature to σ_S. This provided good agreement on all repeated data points. The final error bars for the ^{56}Fe data were approximately 4% while the Sb data error bars were approximately 10%.

Also of interest are the signal-to-noise ratio, S/B, and the quantity $S/(B)^{1/2}$ for the peaks found in the spectra obtained with ^{56}Fe, ^{121}Sb and ^{123}Sb. These quantities are given for the three ^{56}Fe gamma lines in Table F-1 and for the seven Sb gamma lines in Table F-2.

Table F-1

^{56}Fe Gamma Line Statistics for 90° Spectrum

E_γ	S/B	$S/(B)^{1/2}$
0.847	2.98	143.4
1.24	0.68	19.6
1.81	1.02	23.4

Table F-2

Sb Gamma Line Statistics for 90° Spectrum

E_γ	S/B	$S/(B)^{1/2}$
0.910	0.34	17.2
0.999	0.37	17.8
1.025	0.52	35.2
1.089	0.44	19.8
1.102	0.29	18.8
1.145	0.19	7.5
1.338	0.17	5.0